9-26-2017

Resonant-Cavity Optoelectronic Devices for Optical Interconnects

Brian Pile
University of Connecticut - Storrs, brian.pile@gmail.com

Resonant-Cavity Optoelectronic Devices for Optical Interconnects

Brian Clarke Pile, PhD

University of Connecticut, 2017

Internet traffic is increasing exponentially with the continued growth of online streaming, cloud computing, and social media services. This increases demand on data centers that must handle the transmission, routing, and storage of the data. As bandwidth is scaled up, more power efficient systems are required to reduce cost and power consumption, while maintaining thermal requirements. Gigabit connections between the labyrinth of network servers are traditionally made of copper, but link distances are typically limited to ten meters, and the required electronic equalizations add to the power budget. To achieve high bitrates with low energy per bit, optical interconnects are displacing copper, at increasingly short distances. This trend will continue as optical transceiver costs fall and the devices within become more energy efficient.

A category of optoelectronic devices that apply resonant-cavities are uniquely suited to address optical interconnect improvements. The resonant-cavity enhances the device function, by increasing its sensitivity. In this dissertation two such devices are investigated for application in high speed, energy efficient, short reach optical interconnects for data centers.

The first is the microring resonator, which is a planar photonic circuit capable of multiple functions such as optical switching and intensity modulation. An optical switching fabric based on microrings is designed and optical data transmission is simulated. Operated as a modulator, the microring is analyzed theoretically to develop a novel small-signal model that agrees with experimental results, and accurately predicts dynamic power dissipation.

The second device is a novel GaAs-based thyristor photodetector. Operated with surface illumination, the epitaxial structure of the device is compatible with VCSEL integration. The for the fabricated device are presented with an analysis of internal current gain, inherent to the

thyristor operation. Experimental findings are applied to the development of an equivalent circuit model, in order to derive the rise time of the detector. The thyristor detector shows promising results in that high sensitivity is achieved along with a predicted rise time less than 25 ps.

Resonant-Cavity Optoelectronic Devices for Optical Interconnects

Brian Clarke Pile

B.S., University of Connecticut, 2006

M.S., University of Connecticut, 2009

A Dissertation

Submitted in Partial Fulfillment of the

Requirements for the Degree of

Doctor of Philosophy

at the

University of Connecticut

2017

APPROVAL PAGE

Doctor of Philosophy Dissertation

Resonant-Cavity Optoelectronic Devices for Optical Interconnects

Presented by

Brian Clarke Pile, B.S., M.S.

Major Advisor

_____

Geoff W. Taylor

Associate Advisor

_____

Rajeev Bansal

Associate Advisor

_____

John Ayers

University of Connecticut
2017

Table of Contents

List of Figures

1 Chapter 1: Introduction

1.1 Background

Optical interconnects transfer data in the form of light pulses that travel within optical waveguides. The primary advantage of optical versus copper-based electrical communication channels, is the extremely low attenuation of silica glass fibers. For example, the attenuation in single-mode fiber (SMF) is only 0.2-0.3 dB/km at an operating wavelength of λ=1550 nm, and 3 dB/km for multimode fiber (MMF) at λ=850 nm [1]. Furthermore, unlike electrical transmission lines, the attenuation in optical fibers is effectively independent of the signal bitrate. For a typical RG-58 coaxial cable, on the other hand, the attenuation at a frequency f=1 GHz is about 0.6 dB/m which is over two orders of magnitude larger than fiber [2]. Additional benefits of fiber are smaller form factor, lower weight, and natural immunity to electromagnetic interference. Generally speaking, the improvements offered by employing a fiber optic channel come with the disadvantage of increased cost. The need to align optical components with micron precision, and the use of compound semiconductor lasers are both cost contributors. Optical interconnects were therefore initially limited to long haul telecommunication applications, where very long link distances justified the price of investment.

Over the past decade, however, optical interconnects have become increasingly ubiquitous due to the exponential increase in internet traffic, which requires data centers to increase bandwidth between computer servers [3]. Increasing data rates into the gigabit range requires shorter lengths of copper cabling, and electronic equalization

to compensate for signal distortion in the lossy channel. Equalization increases power dissipation and the link lengths are still typically limited to less than 10 m. Therefore, the advantages offered in terms of power, bandwidth, and size have allowed short-reach optical interconnects to be adopted, with typical bitrates of 10 Gbps at link lengths up to 300 m [4]. The vertical cavity surface emitting laser (VCSEL) operating at 850 nm is the primary enabling technology for this change. VCSELs are inexpensive because they can be tested on-wafer by automated systems, without the need to cleave devices prior to test (as in the case of edge emitting lasers). Also, they emit a circular beam that is easily coupled into MMF which simplifies packaging. They are also high-speed and power efficient, with low threshold currents on the order of one milliamp. In 2017, more than 25 million VCSEL-based transceivers are projected to be shipped to customers [5].

Next generation data rates in networking equipment are moving to 40 Gbps, and will continue to 100 Gbps and beyond. In the past few years silicon photonics (SiP) has emerged as a competing technology for high bandwidth capacity interconnects, with the hopes that mature CMOS manufacturing will provide a low cost solution [6]. A variety of devices (besides the laser source) may be monolithically integrated in SiP such as MOS transistors, waveguides, grating couplers, multiplexers, and photodetectors. This enables photonic integrated circuits (PICs) that are capable of 100 Gbps total data rate. A typical transceiver operates with four channels near 1550 nm, each modulated at 25 Gbps, that are transmitted in parallel SMFs [7]. Although state-of-the-art VCSELs have been demonstrated at bitrates greater than 50 Gbps [8], these links will have reduced link lengths in order to manage distortion caused by MMF

multimode dispersion. Therefore, SiP based interconnects using SMF are a promising solution for medium-reach links with lengths between 300 and 2000 m. Commercial products are now available, but widespread adoption will ultimately depend on solving packaging difficulties that are in competition with overall transceiver cost [5].

Because of the growing demand for optical interconnects, much research is underway to improve the performance of the optoelectronic devices inside the transceivers. Resonant-cavity devices are of particular interest because they can be energy efficient and high-speed, simultaneously.

1.2 Dissertation Outline

This thesis examines two types of devices that offer potential improvements in optical interconnect figures of merit. The first device is the microring resonator. Microring resonators have extremely small footprints and provide versatile capabilities for densely integrated optical and electro-optic functions. The second device is a novel resonant-cavity thyristor-based photodetector. Acting as an optoelectronic switch, the thyristor photodetector provides logic-level output voltages with small optical input power, thereby eliminating the need for additional photoreceiver circuitry. The dissertation is organized as follows.

Chapter 2 introduces the analysis of microring resonators. Optical transfer functions for the basic device topology are derived and characterized. Two analysis methods are presented, and the advantages of each approach are discussed. The spectral properties of the optical transmission are derived and summarized, for use in the later chapters.

In Chapter 3, an optical switching fabric based on microring resonators is presented. The fabric is comprised of second-order resonators that function as wavelength selective switches. Design of the 2-by-2 switch element is presented with the off- and on-state optical characteristics. The basic switch element is then cascaded to form a non-blocking topology with four input and output ports. Verification of the design is shown by simulating simultaneous transmission of 40 Gbps optical data streams, through the fabric.

The operation of microring resonators as optical intensity modulators is discussed in Chapter 4. A novel approach for modeling the optically-limited speed is developed, based on small-signal analysis. Two types of modulation are considered involving resonance control and coupling control. Following the theoretical analysis, the model is compared with experimental data for a recently reported modulator. Finally, the analysis is extended to account for electrical consideration of device electrodes, which allows the power consumption of the modulator be accurately predicted.

In Chapter 5 the design and experimental characterization of a resonant-cavity thyristor photodetector is discussed. The epitaxial layer structure is described and simulated optical properties are compared to measurement. Experimental results for the electro-optic detector response are shown across the device resonance. A linear response is found in the off-state, with photo-generated current exceeding that of ideal resonant-enhanced quantum efficiency. The increase is attributed to internal bipolar current gain which is quantified theoretically.

Chapter 6 uses the experimental finding of Chapter 5 to develop an equivalent circuit model for the thyristor photodetector. The circuit allows for an analysis of the transient photoresponse as the detector switches between off- and on-states. Current gain in the detector as well as device parasitics are found to be important factors in maximizing the speed of the turn-on transient.

The thesis is concluded in Chapter 7. Chapters 1-7 focus on digital data transmission using optical links. Analog signal transmission is also of considerable interest for the field of microwave photonics. Additional work has been included in Appendix A, where a sub-type of analog optical link is analyzed. The link uses a pulsed optical source rather than a continuous wave source, and provides frequency conversion by subsampling the input RF signal. This architecture is analyzed theoretically in terms of gain, noise figure, spurious-free dynamic range, and application in photonic analog to digital converters.

The research pursued in this dissertation has resulted in the following publications:

B. C. Pile and G. W. Taylor, "Turn-ON Analysis for a Thyristor-Based Photoreceiver," *IEEE Journal of Quantum Electronics,* vol. 53, pp. 1-7, 2017.

B. C. Pile and G. W. Taylor, "Resonant Cavity Enhanced Thyristor-Based Photodetectors for Optical Receivers," *IEEE Journal of Quantum Electronics,* vol. 52, pp. 1-7, 2016.

B. Pile and G. Taylor, "Small-signal analysis of microring resonator modulators," *Optics Express,* vol. 22, pp. 14913-14928, 2014/06/16 2014.

Y. Zhang, **B. Pile**, and G. W. Taylor, "Design of micro resonator quantum well intensity modulator," *Optical and Quantum Electronics,* vol. 44, pp. 635-648, 2012.

B. Pile and G. W. Taylor, "Performance of Subsampled Analog Optical Links," *Journal of Lightwave Technology,* vol. 30, pp. 1299-1305, 2012/05/01 2012.

Y. Zhang, **B. Pile**, and G. W. Taylor, "Design of microresonator quantum well intensity modulators based on an absorption blue-shift," in *Proc. SPIE 8164, Nanophotonics and Macrophotonics for Space Environments V*, 2011, pp. 81640C-81640C-10.

B. C. Pile, Y. Zhang, J. Yao, and G. W. Taylor, "Resonant optoelectronic thyristor switches as elements for optical switching fabrics," in *Proc. SPIE 8164, Nanophotonics and Macrophotonics for Space Environments V*, 2011, pp. 81640D-81640D-8.

2 Chapter 2: Microring Resonator Analysis

2.1 Introduction

Microring resonators are being investigated for use in optoelectronic integrated circuits due to high quality Q factors and compact size. High Q resonators offer wavelength-selective manipulation of optical signals, while the small dimensions allow for dense integration. As a result, a wide variety of devices have been built using microring resonators such as filters [9, 10], wavelength division multiplexers [11], switches [12], biosensors [13], lasers [14], photodetectors [15], and modulators [16-18].

2.2 Transmission Characteristics

The passive microring resonator operates with constant device parameters that do not vary with time. More complex devices are constructed as extensions of the basic form, that may incorporate multiple rings and/or electro-optically active device regions. This section provides an analysis of the resonant properties of a typical microring resonator.

A basic microring resonator topology is shown in Fig. 2.1a. The microring of radius R is formed by a curved optical waveguide comprising a closed loop. Optical access to the ring is achieved with two sections of straight waveguide, that provide evanescent energy coupling in and out of the ring. The optical input s_i approaches the microring along the straight waveguide and enters the coupling region defined by a coupling coefficient κ_1 and transmission coefficient σ_1. Assuming a lossless coupling region, indicated by the dashed rectangles in Fig. 2.1a, the electric fields at the coupler

outputs (s_t and s_1) are related to the input fields (s_i and s_4) through the matrix relation [19]

$$\begin{bmatrix} s_t \\ s_1 \end{bmatrix} = \begin{bmatrix} \sigma_1 & -j\kappa_1 \\ -j\kappa_1 & \sigma_1 \end{bmatrix} \begin{bmatrix} s_i \\ s_4 \end{bmatrix} \tag{2.1}$$

with $|\kappa_1|^2 + |\sigma_1|^2 = 1$. A corresponding relation applies to the fields at the lower coupler. The optical field coupled into the ring forms a traveling wave that circulates clockwise. During a single roundtrip, this wave experiences a phase shift $\theta=\beta L$ where $L=2\pi R$ is the ring circumference and $\beta = 2\pi\nu n/c = 2\pi n/\lambda$ is the propagation constant in the ring waveguide, n is the effective index of the waveguide mode, c is the vacuum light speed, ν is the optical frequency, and λ is the wavelength of the input light. The circulating wave is also attenuated by a factor $\ell = \exp[-\alpha L/2]$ where α is the intensity attenuation coefficient in the ring. The cavity resonances occur for values of θ that are multiples of 2π such that $\theta_r = m2\pi$, where m is an integer called the mode number. The resonant frequencies are therefore $\nu_r = m(c/nL)$ and the resonant wavelengths are $\lambda_r = nL/m$.

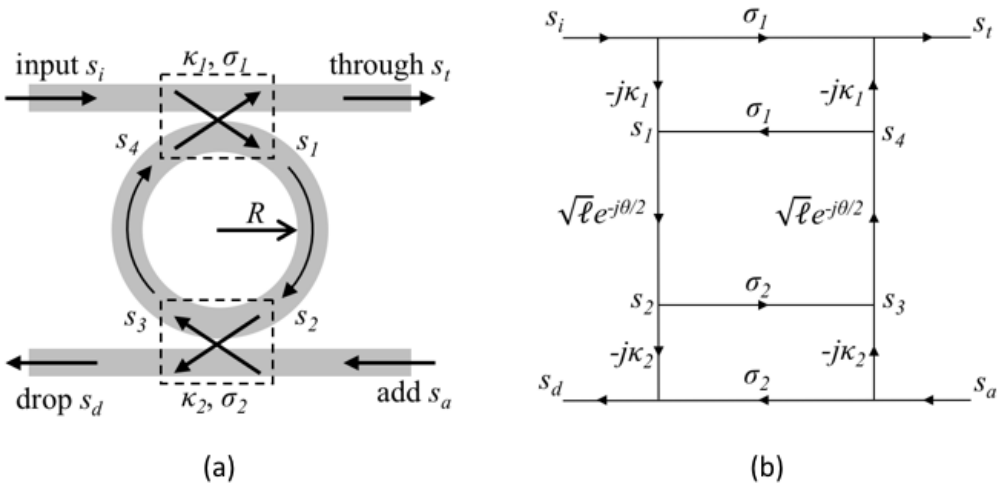

Fig. 2.1 Basic add-drop microring resonator
A first-order add-drop microring resonator (a) and corresponding signal flow diagram (b).

2.2.1 Coupling of Modes in Space Formulation

Transmission characteristics of microring resonators can be determined using the coupling of modes in space analysis [19]. This analysis tracks the wave propagation in the ring as a function of position relative to the coupling regions. The transfer functions of the ring are calculated by solving for the fields at the output ports (s_t and s_d), in terms of the input s_i. This may be done by finding expressions for each of the noted waves in Fig. 2.1a, and systematically eliminating terms containing the internal field components s_1 through s_4.

Alternatively, the resonator can be represented as a linear system by a signal flow diagram as shown in Fig. 2.1b. From this diagram, a technique known as Mason's rule [20, 21] may be applied to obtain the transfer functions directly. This method becomes especially advantageous when analyzing more complicated resonator structures containing multiple rings. Carrying out Mason's rule on the signal flow

diagram in Fig. 2.1b, the response from the input port to the through and drop ports become

$$H_t = \frac{s_t}{s_i} = \frac{\sigma_1 - \sigma_2 e^{-j\theta}}{1 - \sigma_1\sigma_2 e^{-j\theta}} \tag{2.2}$$

and

$$H_d = \frac{s_d}{s_i} = \frac{-\kappa_1\kappa_2\sqrt{\ } e^{-j\theta/2}}{1 - \sigma_1\sigma_2 e^{-j\theta}} \tag{2.3}$$

respectively. The transmission of optical intensity is then found by squaring the absolute value of (2.2) and (2.3) to give

$$T_t = \left|\frac{s_t}{s_i}\right|^2 = \frac{\sigma_1^2 + (\sigma_2)^2 - 2\sigma_1\sigma_2\cos\theta}{1 + (\sigma_1\sigma_2)^2 - 2\sigma_1\sigma_2\cos\theta} \tag{2.4}$$

and

$$T_d = \left|\frac{s_d}{s_i}\right|^2 = \frac{(\kappa_1\kappa_2)^2}{1 + (\sigma_1\sigma_2)^2 - 2\sigma_1\sigma_2\cos\theta}\ . \tag{2.5}$$

This result shows that the transmissions are periodic with round trip phase shift θ because of the cosine dependence. Also, when $\theta = m2\pi$ such that the phase shift is an integer multiple of 2π, the numerator of (2.4) may be factored to form $(\sigma_1 - \ell\sigma_2)^2$. This is an interesting result, showing that if the resonator is designed to have $\sigma_1 = \ell\sigma_2$, then ideally no optical power exits from the through port. Instead, the power is transferred to the drop port under a condition known as critical coupling. For this reason, the topology in Fig. 1a is known as the add-drop configuration, since input signals that resonate with the ring can be directed to the drop port, and replaced with a new signal injected at the add port.

Figure Fig. 2.2 shows example transmission spectrums given by (2.4) and (2.5) for a microring with radius R=5 μm, n=3.3, and α=10 cm^{-1}. The coupling parameters are taken to be σ_1=0.93, and σ_2=0.94. Here, the transmissions are plotted against the detuning phase $\delta = \beta L - \theta_r$, which is the deviation in roundtrip phase with respect to a particular resonance of interest. The m=67 resonance occurs in the telecom C-band at λ_r=1547.4 nm, and is chosen as the reference.

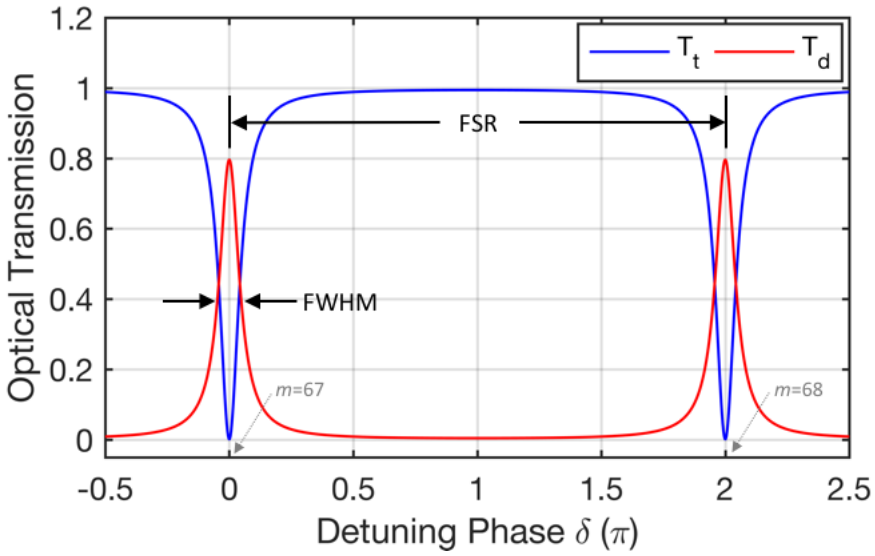

Fig. 2.2 Add-drop transmission spectra
Example optical transmission spectra for an add-drop microring resonator. The blue curve is the transmission T_t from the input port to the through port and the red curve is the transmission T_d from the input port to the drop port.

The interesting transmission features occur at the resonances, where T_t exhibits a notch response and T_d shows a bandpass response. Note that the maximum drop port transmission does not reach unity in this example because internal loss in the ring has been included. If the loss were negligible such that $\ell \approx 1$, total power transfer occurs under the lossless critical coupling condition σ_1=σ_2. Also note that the structure is only

reciprocal in the lossless and critically coupled case, where the transmission from add-to-drop port equals T_t and the transmission from add-to-through port equals T_d.

2.2.2 Coupling of Modes in Time Formulation

The basic microring resonator in Fig. 2.1 can also be analyzed in the time domain using the coupling of modes in time (CMT) formulation. This method represents the optical dynamics with a differential equation for the total energy stored in the ring. It is especially useful for modeling active ring devices, as will be shown in Chapter 4 for the case of microring modulators.

A ring resonator may be described heuristically as a lumped oscillator with energy amplitude $a(t)$, normalized such that $|a(t)|^2$ is the total energy, in Joules, stored in the ring [22, 23]. Assuming that the traveling wave circulating in the ring has constant amplitude $A(t)$ (neglecting propagation loss for the moment), then $|A(t)|^2$ is the power flowing through any ring cross section. The total energy stored is then related to the power flowing in the ring as $|a(t)|^2 = T|A(t)|^2$, where $T = n_g L/c$ is the round trip travel time. The oscillator has a resonant frequency ω_r and energy decay time constant τ. There are two sources of energy loss contributing to τ. Loss due to coupling to the upper and lower straight waveguides are represented by τ_e and τ_d respectively, and the intrinsic loss in the ring is accounted for with time constant τ_ℓ. The overall energy decay time constant τ is determined from these components by $\tau^{-1} = \tau_e^{-1} + \tau_d^{-1} + \tau_\ell^{-1}$. The time rate of change for $a(t)$ can then be written as

$$\frac{da}{dt} = \left(j\omega_r - \frac{1}{\tau} \right) a - j\mu_e s_i \tag{2.6}$$

and the output waves are given by

$$s_t = s_i - j\mu_e a \tag{2.7}$$

and

$$s_d = -j\mu_d a \tag{2.8}$$

where μ_e (μ_d) are the coupling strengths between $a(t)$ and the upper (lower) waveguides, and are related to the power coupling coefficients through

$$\mu_e^2 = \frac{2}{\tau_e} = \frac{\kappa_1^2}{T} \tag{2.9}$$

and

$$\mu_d^2 = \frac{2}{\tau_d} = \frac{\kappa_2^2}{T}. \tag{2.10}$$

The choice of the $-j$ factor in front of the coupling factors μ_e and μ_d in (2.7) and (2.8) is chosen arbitrarily by the reference plane [19, 22], to be consistent with the CMS approach where coupled fields are phase shifted by $-j$, as shown in (2.1). In the ring, the circulating wave power is attenuated by a factor of $\exp(-\alpha L)$ per round trip, and therefore the power loss per round trip is proportional to $[1 - \exp(-\alpha L)]$. When the ring loss is small, such that $\alpha L \ll 1$, then the intrinsic loss time constant is related to the attenuation coefficient as

$$\frac{2}{\tau} = \frac{c\alpha}{n_g} = \frac{\alpha L}{T}. \tag{2.11}$$

Optical transfer functions for the add-drop microring in Fig. 2.1 are obtained by applying a monochromatic wave to the input of the form $s_i = s_{i0}\exp(j\omega t)$. Since the input s_i is purely harmonic, the energy amplitude follows the same time dependence according to $a = a_0\exp(j\omega t)$. Inserting these expressions for the input field and energy amplitude into (2.6) yields

$$j\omega a = \left(j\omega_r - \frac{1}{\tau} \right) a - j\mu_e s_i \tag{2.12}$$

and solving for a gives

$$a = \frac{-j\mu_e}{j(\omega - \omega_r) + \frac{1}{\tau}} s_i \ . \tag{2.13}$$

Substituting this result into (2.7), the frequency-dependent response to the through port is found to be

$$H_t = \frac{s_t}{s_i} = \frac{j(\omega - \omega_r) + \frac{1}{\tau_d} + \frac{1}{\tau} - \frac{1}{\tau_e}}{j(\omega - \omega_r) + \frac{1}{\tau}} \tag{2.14}$$

and substitution of (2.13) into (2.8) gives the response to the drop port as

$$H_d = \frac{s_d}{s_i} = \frac{-\sqrt{\frac{2}{\tau_e}}\sqrt{\frac{2}{\tau_d}}}{j(\omega - \omega_r) + \frac{1}{\tau}} \ . \tag{2.15}$$

From (2.14) it is seen that, on resonance, the through port response reduces to zero when $\tau_e^{-1} = \tau_d^{-1} + \tau_\ell^{-1}$, which is the condition of critical coupling described in the CMS analysis above. These criteria can be shown to be equivalent when the coupling coefficients and intrinsic resonator loss is small. In this situation, the through coupling coefficients may be approximated as $\sigma_1 = \sqrt{1 - \kappa_1^2} \approx 1 - \kappa_1^2/2$ and $\sigma_2 = \sqrt{1 - \kappa_2^2} \approx 1 - \kappa_2^2/2$ while the round trip attenuation factor is approximately $\ell = \exp(-\alpha L/2) \approx 1 - \alpha L/2$. Inserting these approximations into the CMS critical coupling condition yields the following reduction

$$
\begin{aligned}
\sigma_1 &= \sigma_2 \\
1-\frac{\kappa_1^2}{2} &= \left(1-\frac{\alpha L}{2}\right)\left(1-\frac{\kappa_2^2}{2}\right) \\
1-\frac{\kappa_1^2}{2} &\approx 1-\frac{\kappa_2^2}{2}-\frac{\alpha L}{2} \\
\frac{\kappa_1^2}{T} &= \frac{\kappa_2^2}{T}+\frac{\alpha L}{T} \\
\tau_e^{-1} &= \tau_d^{-1}+\tau^{-1}
\end{aligned}
\tag{2.16}
$$

and shows the equivalence of the CMS and CMT critical coupling condition. The ring responses given in (2.4) and (2.5) can also be shown to be equivalent to (2.14) and (2.15) using the same approximations. Finally, the optical power transmissions are found by squaring the absolute values of the CMT responses to find

$$
T_t = \frac{\left(\omega-\omega_r\right)^2+\left(\frac{1}{\tau_d}+\frac{1}{\tau}-\frac{1}{\tau_e}\right)^2}{\left(\omega-\omega_r\right)^2+\left(\frac{1}{\tau}\right)^2} \tag{2.17}
$$

and

$$
T_d = \frac{\frac{2}{\tau}\frac{2}{\tau_e}}{\left(\omega-\omega_r\right)^2+\left(\frac{1}{\tau}\right)^2} \tag{2.18}
$$

for the through and drop ports, respectively. The transmissions are Lorentzian functions centered around a resonator resonance, and are not periodic in frequency as was seen in the CMS approach. This is a main difference of the two formulations, and in the following section add-drop ring transmissions are compared to illustrate differences between these results.

2.2.3 Comparison of CMS and CMT Optical Transmission

Example transmission spectra given by the CMS and CMT approach are shown in Fig. 2.3, using the same resonator parameters as in Fig. 2.2.

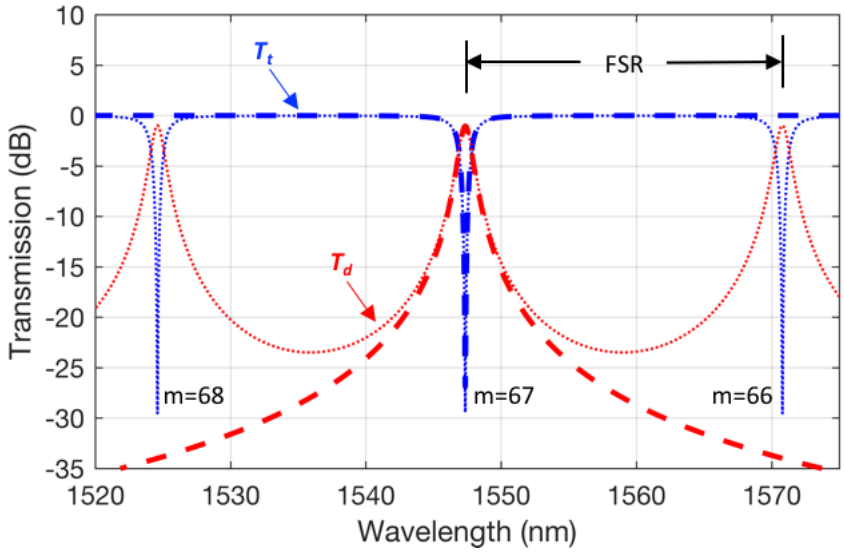

Fig. 2.3 Comparison of transmission using CMS and CMT analysis
Dotted curves show the CMS transmissions given by (2.4) and (2.5). Dashed curves show CMT transmissions given by (2.14) and (2.18).

The dashed curves show the CMT transmissions, exhibiting a single transmission notch and drop passband at the resonant wavelength of λ_r=1547.4 nm. Away from resonance the T_d rolls off monotonically while T_t goes to unity (0 dB). In contrast, the CMS transmissions, shown by dotted curves, capture the periodic nature of the resonator response according to the FSR. Near the resonance of interest, with m=67, the two formulations converge with good agreement. Therefore, if operating the resonator with input signals near a single resonance, the CMT approach provides a simplified analysis, with the benefit of time-domain representation that will be developed further in chapter 4. If operating across a large fraction of the FSR, then the CMS approach is most accurate.

2.3 Spectral Properties

Spectral properties of resonators are generally characterized in terms of the resonance linewidth and free spectral range. The resonance linewidth is a measure of spectral selectivity and is generally taken as the full width at half maximum (FWHM) of the resonance. The free spectral range (FSR) is the separation between resonances, in terms of optical frequency or wavelength. Other metrics are obtained from these two quantities such as quality factor Q, cavity finesse $\mathcal{F}$, and photon lifetime τ_p. The FSR and linewidth for the example add-drop ring resonator are indicated in Fig. 2.2. These values are determined by the device parameters and are derived for the add-drop topology next.

The cavity linewidth can be found by applying a series expansion to (2.5) about a given resonance θ_r, using $\cos(\theta-\theta_r) \approx 1-(\theta-\theta_r)^2/2$, which yields the Lorentzian function

$$T_d \approx \frac{\dfrac{\left(\kappa_1\kappa_2\right)^2}{\sigma_1\sigma_2}}{\left(\dfrac{1-\sigma_1\sigma_2}{\sqrt{\sigma_1\sigma_2}}\right)^2+\left(\theta-\theta_r\right)^2} \tag{2.19}$$

from which the FWHM can be readily identified from the denominator as

$$\Delta\theta\big|_{FWHM} = 2\frac{1-\sigma_1\sigma_2}{\sqrt{\sigma_1\sigma_2}}. \tag{2.20}$$

To express the linewidth in terms of optical frequency span, rather than round trip phase shift, the relation

$$\Delta\theta = \frac{2\pi L}{c}\left(n+\nu\frac{dn}{d\nu}\right)\Delta\nu = \frac{2\pi L n_g}{c}\Delta\nu \tag{2.21}$$

where n_g is the group index in the ring, is combined with (2.20) to give

$$\Delta\upsilon\big|_{FWHM} = \frac{c}{\pi n_g L}\frac{1-\sigma_1\sigma_2}{\sqrt{\sigma_1\sigma_2}}. \tag{2.22}$$

It is often more convenient to express the linewidth in terms of wavelength span, since optical test instruments often return measurements based on wavelength. Using the expression $\Delta\upsilon = (c/\lambda_r^2)\Delta\lambda$ with (2.22), the linewidth in terms wavelength is

$$\Delta\lambda\big|_{FWHM} = \frac{\lambda_r^2}{\pi n_g L}\frac{1-\sigma_1\sigma_2}{\sqrt{\sigma_1\sigma_2}}. \tag{2.23}$$

The FSR may be found by finding the change in frequency required to increment the round trip phase shift by 2π, according to $(d\theta/dv)\Delta\upsilon = 2\pi$, resulting in

$$\Delta\upsilon\big|_{FSR} = \frac{c}{n_g L} \tag{2.24}$$

or in terms of wavelength as

$$\Delta\lambda\big|_{FSR} = \frac{\lambda_r^2}{n_g L}. \tag{2.25}$$

The FSR depends inversely on the ring length, therefore to incorporate microrings in a wavelength-division multiplexed system small rings are desirable to maximize the number of channels that can be allocated across the free spectral range.

The remaining resonator parameters Q, $\mathcal{F}$, and τ_p, are expressed here in terms of the wavelength versions of FSR and FWHM [1]. Quality factor is given by

$$Q = \frac{\lambda_r}{\Delta\lambda\big|_{FWHM}} = \frac{\pi n_g L}{\lambda_r}\frac{\sqrt{\sigma_1\sigma_2}}{1-\sigma_1\sigma_2}\ , \tag{2.26}$$

the finesse is

$$\mathrm{F} = \frac{\Delta\lambda\big|_{FSR}}{\Delta\lambda\big|_{FWHM}} = \frac{\pi\sqrt{\sigma_1\sigma_2}}{1-\sigma_1\sigma_2}\ , \tag{2.27}$$

and the photon lifetime is

$$\tau_p = \frac{1}{2\pi\Delta\nu\big|_{FWHM}} = \frac{n_g L}{2c}\frac{\sqrt{\sigma_1\sigma_2}}{1-\sigma_1\sigma_2}\ . \tag{2.28}$$

Each of these parameters is a measure for the ability of a resonator to store energy, with the following physical interpretations [1, 24]. The resonator quality factor Q represents the number of electric field oscillations that occur before the initial stored energy is reduced by a factor of $1/e$. Therefore higher resonant frequency cavities have larger Q for given resonator parameters. Cavity finesse $\mathcal{F}$ indicates the number of round trips the circulating wave completes until the energy is reduced to the $1/e$ point (with an additional 2π factor). The time elapsed for the initial energy be reduced to the $1/e$ point is the photon lifetime τ_p, and for optical resonators is typically on the order of picoseconds. In the following, FWHM will simply be referred to as the linewidth, with units specifying whether frequency or wavelength is being denoted. Similarly, free spectral range will be referred to as FSR, with units indicating either resonant frequency or wavelength separation.

It is illustrative to calculate the spectral parameters of the example microring resonator shown in Fig 1a. Using the stated device parameters (assuming $n \approx n_g$) along with (2.22) and (2.23), the linewidth is 1.11 nm or 138 GHz. The FSR is calculated from (2.24) and (2.25) to be 2.89 THz, or 23.1 nm. From (2.26) the quality factor is Q=1401 and (2.27) gives a finesse of $\mathcal{F}$=21. Lastly, the photon lifetime is determined from (2.28) to be τ_p=1.15 ps.

3 Chapter 3: Microring-Based Optical Switching Fabric

3.1 Introduction

Fiber optic systems require switches for routing signals between nodes attached to the network. Switching is typically performed by electronic systems. At each network node, an optical-to-electrical (OE) conversion is performed followed by electronic buffering. The electrical data is forwarded to the desired output port, where electrical-to-optical (EO) conversion is performed, and then launched on fiber to the next network destination. Electronic switches are specifically designed for a given data rate and networking protocol. As a result, they need to be replaced when next generation data rates and protocols are introduced to the network [25]. Also, the conversion to and from the electrical domain necessitates large numbers of optoelectronic devices at the switch. Furthermore, processing the vast amount of electrical data can currently consume more than 10 kW of power [26]. These requirements are significant cost factors that drive research into new switching technologies that improve performance and reduce cost [27, 28].

Optical switching fabrics offer potential advantages over electrical implementations, because the signals are switched in the optical domain. In this way, the switch is transparent in terms of data rate and protocol, and would not require updates to support future system upgrades. While electronic processing is still required to control the state of the fabric, electrical power is not dissipated in transferring the actual data bits through the switch. Optical switches exist as discrete components such as dual-channel directional couplers or 2x2 Mach-Zehnder interferometers, however, cascading many such devices into a scalable fabric results in a bulky system with high

cost. Integrated optical solutions are desired for high switch densities and reduced manufacturing cost.

In section 3.2 a 2x2 optical switch element is described for use in optical switching fabrics. The switch is based on a 2nd-order microring add-drop resonator, and can be cascaded to form a scalable fabric topology. Design of the element is presented, and a prototype 4x4 switch fabric is proposed in section 3.3. The fabric performance is evaluated by simulating simultaneous switching of 40 Gbps data, along with a 2 Gbps millimeter-wave optical signal with a 40 GHz RF carrier.

3.2 Resonant Switching Element Design

To form a scalable switching fabric, a suitable 2x2 switching element is required. Microring-based switches are attractive devices due to the compact footprint which allows dense integration, and therefore a large number of input and output ports can be supported. Also, the resonant behavior allows the switch to operate with low power consumption since relatively small changes in refractive index, and therefore small drive voltages, are required to change between on- and off-states.

A 2nd-order microring switch depicted using a series-coupled ring structure is shown in Fig. 3.1a. The double ring configuration improves the sharpness of the filter and also maintains direction of signal propagation in the forward direction. Input and output signals are coupled to the resonators by two straight waveguides. When the wavelength of the input lightwave matches the resonance of the rings, the signal is switched from input one to output two (or from

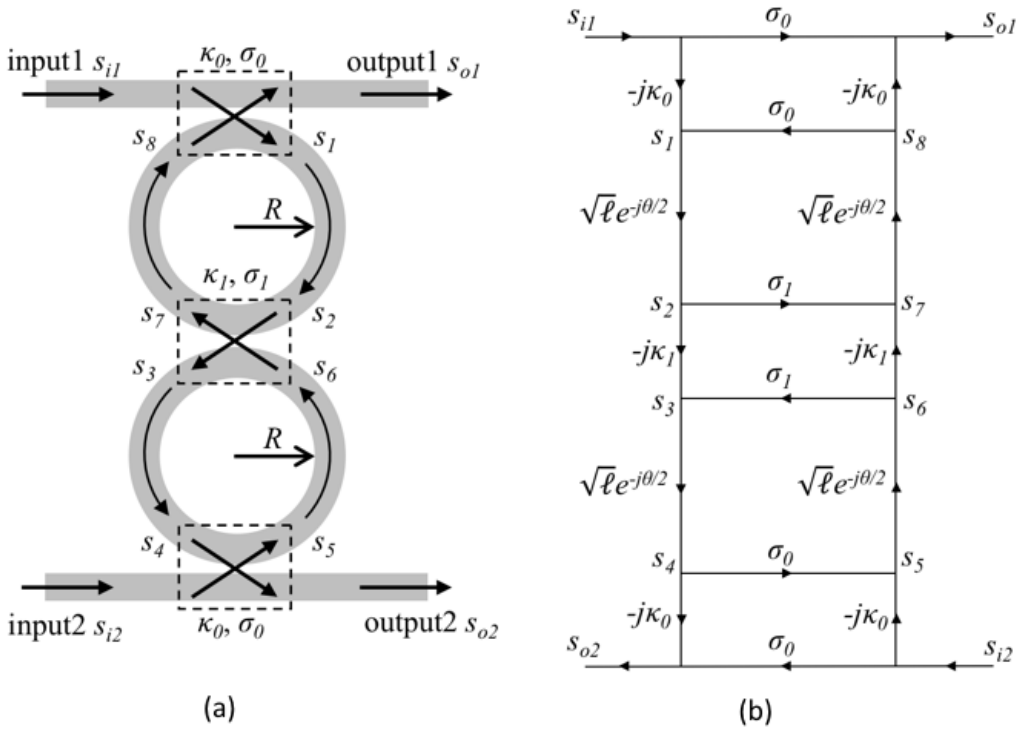

Fig. 3.1 2x2 switch element
A second order, 2x2 microring switch element (a) and corresponding signal flow diagram (b).

input two to output one), thereby achieving the on-state. On the other hand, when the input light does not resonate with the rings the signal will not couple to the adjacent waveguide and the switch is then in the off-state. Switching is achieved through electrical control of the refractive index in the resonators which changes the resonance of the switch. By decomposing the structure in Fig. 3.1a into the signal-flow graph of Fig. 3.1b, Mason's rule can conveniently be used to determine the optical response. The through response can be written as

$$H_t = \frac{s_{01}}{s_{i1}} = \frac{\sigma_0 - \sigma_1\left(1+\sigma_0^2\right)\ e^{-j\theta} + \sigma_0\ ^2 e^{-j2\theta}}{1 - 2\sigma_0\sigma_1\ e^{-j\theta} + \sigma_0^2\ ^2 e^{-j2\theta}} \tag{3.1}$$

and the cross response can be written as

$$H_c = \frac{s_{02}}{s_{i1}} = \frac{j\kappa_0^2\kappa_1\ e^{-j\theta}}{1-2\sigma_0\sigma_1\ e^{-j\theta}+\sigma_0^2\ ^2e^{-j2\theta}} \tag{3.2}$$

where κ_0 is the coupling coefficient between the bus waveguide and the rings, and κ_1 is the coupling coefficient between the two rings. All other variables are as defined previously in section 2.2.

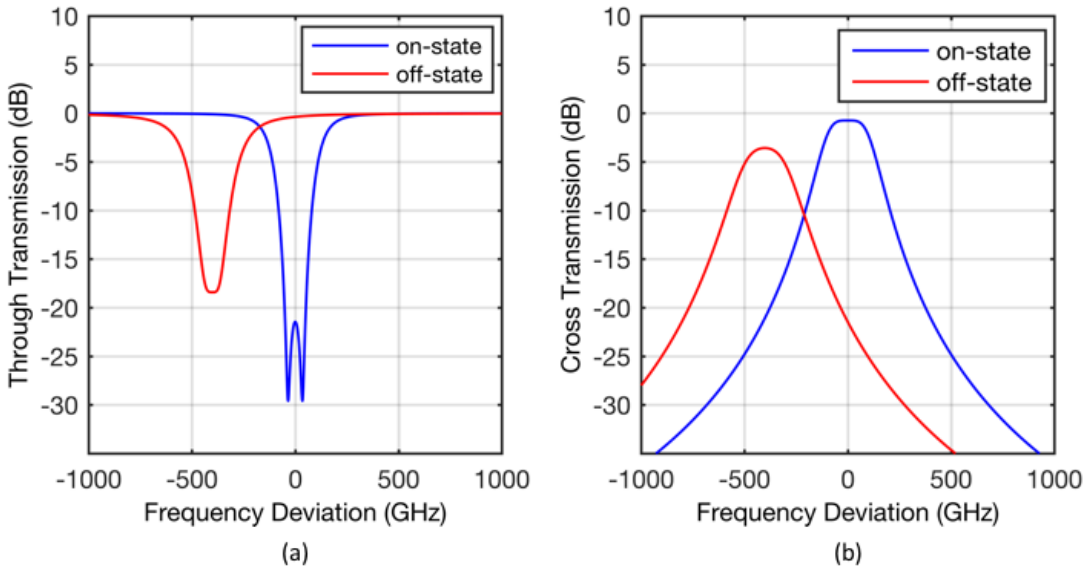

Fig. 3.2 Switch transmission in off- and on-states
Response of the 2x2 switch element at the through (a) and cross (b) outputs. The on-state is shown by the blue curves and the off-state is shown by the red curves.

The second-order switch response in both the on- and off-states is shown in Fig. 3.2. The responses were calculated using absorption and index parameters for a GaAs based quantum well modulator structure, previously analyzed in [29, 30]. Application of voltage bias to the modulator produces a blue shift in the quantum well absorption edge, and is accompanied by a change in refractive index according to the Kramers-Kronig relations [1]. An effective radius of R=5 μm was used with n=3.3, and the waveguide-ring and ring-ring coupling coefficients were κ_0=0.4 and κ_1=0.08. These values were chosen in order to achieve the on-state where the cross response has a flat,

boxlike shape whereas the through port simultaneously shows a deep notch with over 20 dB of isolation over a bandwidth of 100 GHz. The input light has a wavelength of λ=1016.4 nm which corresponds to the m=51 resonance number of the switch.

To activate the switch, the effective index of refraction is increased by Δn=0.0045 which lowers the resonant frequency by $\Delta f_r=(\Delta n/n)f_r$=402 GHz (corresponding to a red-shift in wavelength of $\Delta\lambda_r$=1.33nm). For the active waveguide structure under consideration, this corresponds to an applied voltage of less than one volt. In the off-state, Fig. 3.2a shows that the input light is not coupled to the switch and passes straight through to the output port with a small insertion loss of IL_t=0.4 dB and the crosstalk to the cross port is less than 20 dB as seen in Fig. 3.2b.

In the on-state, the input light is coupled through the switch to the adjacent waveguide and leaves through the cross port with an insertion loss of IL_c=0.8dB and the crosstalk to the through port is again less than 20 dB. The low insertion loss of the switch is critical for application in a largely scalable fabric since the input optical signals will pass through many cascaded switch elements, accumulating loss along the way. Note that the responses in Fig. 3.2a change shape when the switch changes state. This is due to a change in absorption in the active waveguide from α_{on}=10 cm^{-1} in the on-state to α_{off}=50 cm^{-1} in the off-state [30].

3.3 Prototype Switching Fabric Topology and Simulation Results

The 2x2 switching elements discussed in the previous section can be arranged in the topology shown in Fig. 3.3, as a 4x4 example. With this arrangement the fabric is non-blocking, that is, when a given pathway between input and output is established any other pathway may also be established with the remaining input and output ports, provided that each input is routed to a unique output port. Another advantage of this

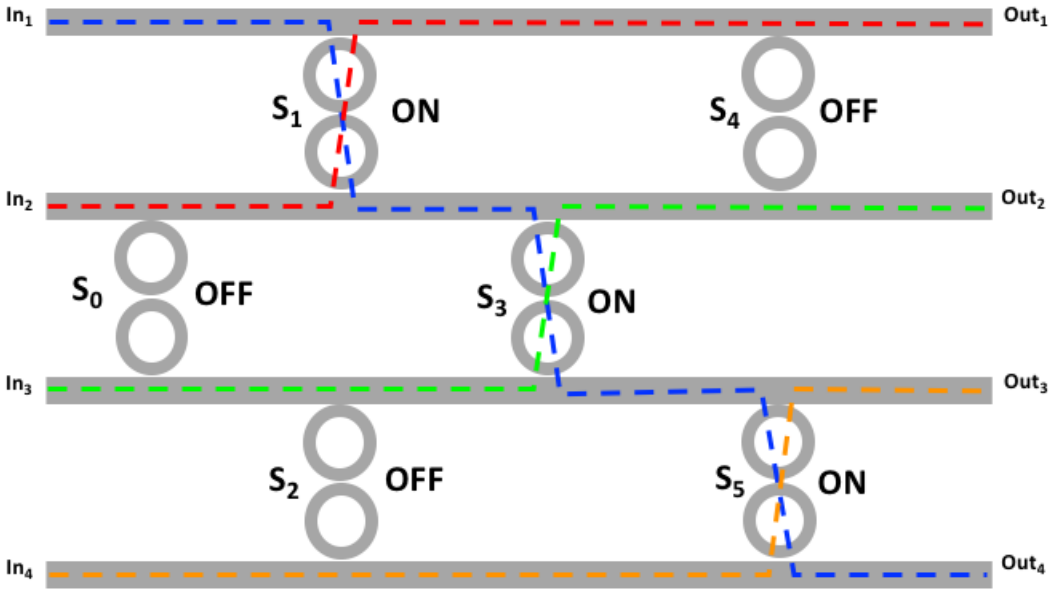

Fig. 3.3 Prototype switching fabric
Switching fabric topology with four inputs and four outputs. In this example, switches S_1, S_3, and S_5 are in the on-state while the remaining switches are in the off-state. The connected pathways through the fabric are shown by the dashed lines.

topology is that there are no waveguide crossings that introduce optical losses that could limit the scalability of the switching fabric [31]. The fabric also offers the potential for wavelength division multiplexing capabilities as shown in Fig. 3.3 by the inclusion light blue colored switches. In this situation, the light blue switches would

have a different resonant frequency, allowing inputs with signals on multiple wavelengths to be routed independently, while sharing the straight bus waveguides.

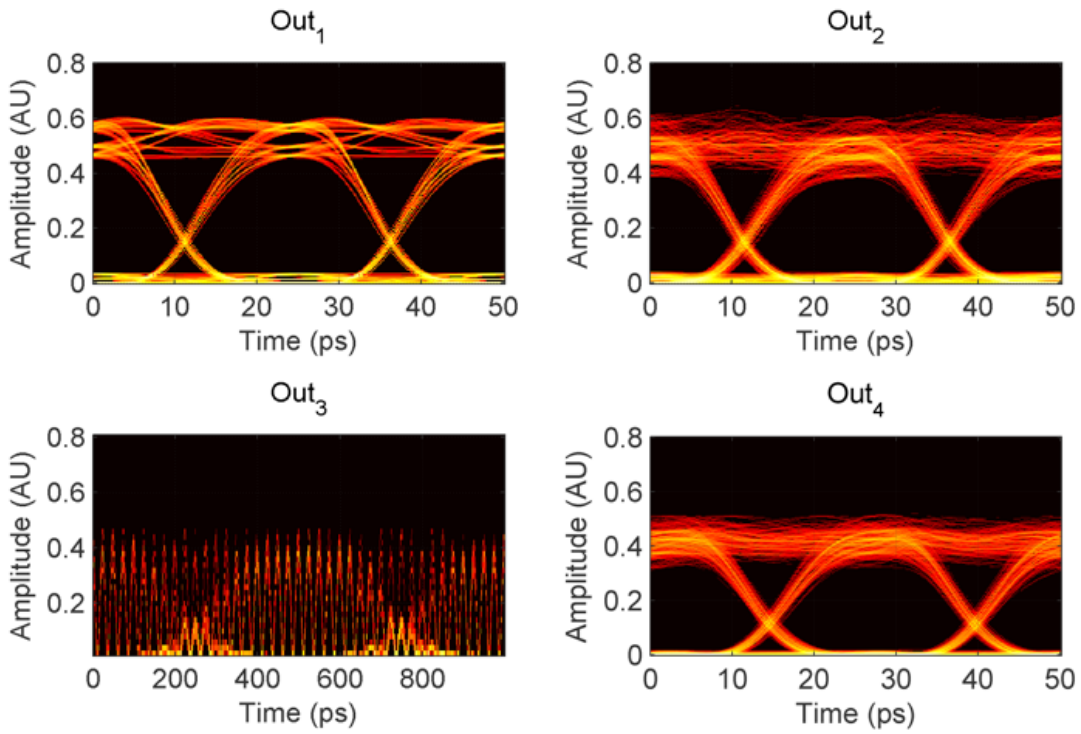

Fig. 3.4 Switching fabric simulation
Simulated eye diagrams at the switching fabric output ports. Outputs 1, 2, and 4 show wide open eyes for data at 40 Gbps. Output 3 shows an open eye at 2 Gbps with the 40 GHz millimeter-wave carrier superimposed.

To validate the switching fabric operation, a time-domain simulation of the fabric shown in Fig. 5 is performed. The fabric is chosen to be in the state where switch S1, S3, and S5 are on while the remaining switches are off. The individual elements are designed identically to the switch element discussed in section 3.2. To show the opportunity for switching high-speed baseband data along with mm-wave optical signals, 40 Gbps NRZ pseudo-random data is input to ports 1-3 while a 40 GHz optical-carrier-suppressed (OCS) [32] signal modulated by 2 Gbps data is applied to input 4.

For this fabric state, the established pathways are shown by the dashed lines in Fig. 3.3. Fig. 3.4 shows the eye diagrams at the output ports. At output ports 1, 2, and 4 the eyes are wide open showing that the input signals have not been significantly distorted by group delay dispersion or crosstalk while traversing the fabric. The insertion losses of these three channels are different due to the fact that the signals have passed through different numbers of switches in the on- and off- states. The eye diagram at output port 3 also shows an open eye, which is superimposed with the 40 GHz carrier. Due to the wide bandwidth of the individual switching elements, it should be noted that higher data rates and mm-wave carrier frequencies can also be supported by this design and the example here is not at the limit of the fabric throughput.

3.4 Conclusion

An optical switching fabric based on microring resonator switches has been designed and simulated. The 4x4 example presented was able to simultaneously switch three 40 Gbps baseband signals and one 2 Gbps 40GHz carrier mm-wave optical signal. Although microresonators are typically regarded in a narrowband context, the results here show that broadband operation can also be achieved through proper selection of coupling coefficients and on-state absorption.

4 Chapter 4: Microring Resonator Modulators

4.1 Introduction

Over the past decade, microring-based optical modulators have been researched extensively by many groups. The interest lies in the fact that these modulators can be energy efficient, high-speed, and densely integrated into systems requiring a large number of optical interconnections, as in data centers and high-performance computers. Furthermore, when combined with other photonic devices such as photodetectors and wavelength-division multiplexers, highly-integrated optical transceivers are becoming possible [33-35].

Intensity modulation is most commonly obtained from microring resonators in two different ways. In the first method, the refractive index within the ring is changed in order to shift the resonant wavelength, which in turn modulates the intensity transmission through the device [36, 37]. These devices will be referred to as resonance-modulated microring resonators (RM-MR). High modulation efficiency is achieved in RM-MR even for small shifts in the resonant wavelength because the resonators typically have a high quality factor Q, and therefore can have low power consumption. On the other hand, high Q resonators have a long photon lifetime τ_p which limits the rate at which optical power can be injected or extracted from the ring, which imposes a fundamental optical limitation on the modulation speed of the device. This may be mitigated by using lower Q resonators, but at the expense of modulation efficiency. A second method for using the microring as an intensity modulator is to change the coupling coefficient to the resonator while keeping the resonance fixed,

which will be referred to as coupling-modulated microring resonators (CM-MR). This method has been investigated since resonance-enhanced operation is still obtained but the bandwidth is no longer limited by the photon lifetime and therefore there is the potential to be simultaneously low-power and high-speed [38, 39]. Therefore, it is important to quantify the difference in performance limitations between these microring modulators, in order to weigh the tradeoffs involved when designing photonic links.

In this chapter, a small-signal analysis for both types of modulators is developed in order to evaluate the two types of devices in terms of bandwidth, modulation efficiency, footprint, and power consumption. The specific electrode structure of the device, which imposes its own electrical bandwidth limitation and contribution to the overall power consumption, is not considered here. Instead, it is supposed that some parameter of the resonator has been changed, such as index of refraction or coupling coefficient, and the response of the output power to this change is examined. In this way, the fundamental optically-limited performance of the modulators is revealed. If one knows the relationship between drive voltage/current and index of refraction for a specific electrode structure, it is possible to combine that with the derived results to determine the overall speed and power consumption. Note that other authors have also analyzed the performance of these modulators either numerically or using small-signal methods [38, 40-42] and the results have provided significant insight, however simple expressions for the transfer functions and modulation efficiencies are not available. The results within are formulated in terms of the parameters of optical cavities, such as photon lifetime and quality factor Q. These results offer a more lucid view of the

limitations of microring modulators, in a familiar framework of cavity parameters and second-order transfer functions. In addition to descriptions of coupling controlled and index controlled microrings, the results are compared to the traditional Mach-Zehnder modulator (MZM) on the basis of speed, power consumption, and footprint in order to evaluate the merits of each device with respect to the well-known, and widely used MZM.

This chapter is organized as follows. In section 4.2 a small-signal analysis is performed using the differential equations that govern the CMT resonator model, resulting in transfer functions and modulation efficiencies for both RM-MR and CM-MR resonators. In section 4.3 these results are compared with experimental data and in section 4.4 the performance of the modulators are compared and power consumption estimates are presented.

4.2 Small-Signal Approach

Optical modulation is achieved in a microring resonator by varying the parameters of its transfer characteristics, such as the resonant frequency or the coupling coefficient. For example, Fig. 4.1a shows a microring with time-varying refractive index $n(t)$, that induces resonance modulation. When the resonant frequency is shifted by Δf_r, due to a Δn, then the transmission of the optical carrier is

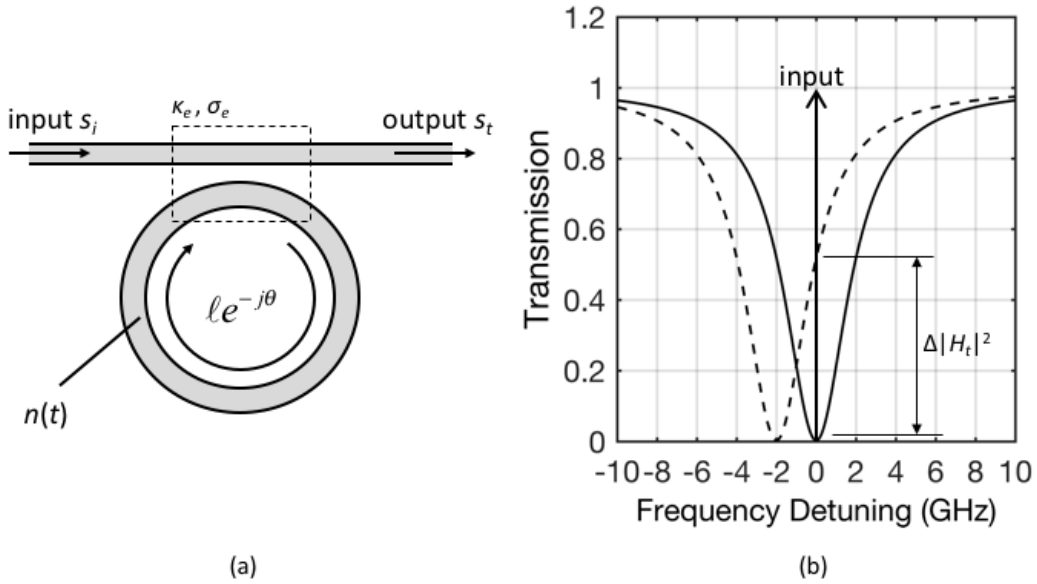

Fig. 4.1 Resonance-modulated microring
Basic resonance-modulated microring resonator with time-varying refractive index (a). Illustration of intensity modulation through resonance shift (b).

modified by $\Delta|H_t|^2$, which gives rise to intensity modulation as illustrated in Fig. 4.1b. In this section the transfer functions between small-signal perturbations of the resonator parameters and the small-signal output power are found. First, a general approach to finding the transfer functions is outlined, which is then applied to analyze two types of modulation. The framework for carrying out the small-signal analysis is presented in terms of index modulation in the ring. However, the same procedure is followed for any type of microring modulation.

Consider varying the index sinusoidally so that $n(t) = n + \Delta n \cos(\omega_m t)$ where n is the DC index, Δn is the modulation amplitude, and ω_m is the angular modulation frequency. The sinusoidal index perturbation will impart the output wave s_t with upper and lower sidebands at $\omega_0 + \omega_m$ and $\omega_0 - \omega_m$, respectively, where ω_0 is the (constant) carrier frequency of the input CW light source. The output wave can then be written as

$$s_t = s_{t0}e^{j\omega_0 t} + s_{t1}^{+}e^{j(\omega_0+\omega_m)t} + s_{t1}^{-}e^{j(\omega_0-\omega_m)t} \tag{4.1}$$

where s_{t1}^{+} and s_{t1}^{-} are complex amplitudes of the upper and lower sidebands, which are proportional to Δn, and s_{t0} is the amplitude of the transmitted carrier. Note that the energy amplitude $a(t)$ is similarly imparted with sidebands of amplitude a_1^{+} and a_1^{-}. The output power of the modulator is the absolute value, squared, of (4.1) which consists of two beat signals generated between the carrier and each sideband, and the self-beating of the carrier. In the small-signal regime, where the modulation depth is much less than unity, the second-order harmonic that arises from the beating of upper and lower sidebands can be neglected, as well as the DC contribution from self-beating of the sidebands. With these adjustments the output power has the form

$$P_{out} = |s_t|^2 = |s_{t0}|^2 + \mathrm{Re}\left\{\left(s_{t0}^{*}s_{t1} + s_{t0}s_{t1}^{-*}\right)e^{j\omega_m t}\right\}. \tag{4.2}$$

In general, the modulator output power can be written as

$$P_{out}(t) = P_{DC} + \Delta p\cos(\omega_m t + \phi) = P_{DC} + \mathrm{Re}\left\{H_n(\omega_m)\Delta n e^{j\omega_m t}\right\} \tag{4.3}$$

where $P_{DC} = |s_{t0}|^2 = |H_t|^2 P_{in}$ is the DC output power, Δp is the small-signal output power amplitude, ϕ is the phase angle of the small-signal output power, and $H_n(\omega_m)$ is the linearized transfer function for index modulation, which specifies the frequency dependent response of the output power to a change in index. Comparing (4.2) and (4.3), the transfer function in terms of the complex amplitudes is found to be

$$H_n(\omega_m) = \frac{\Delta p}{\Delta n} = \frac{s_{t0}^{*}s_{t1} + s_{t0}s_{t1}^{-*}}{\Delta n} \tag{4.4}$$

The same procedure is followed to analyze the response of the modulator to changes in other cavity parameters such as $\Delta\kappa_e$ or $\Delta\alpha$. The focus of the next sections will be to find the sideband amplitudes s_{t1}^{+} and s_{t1}^{-} through a small-signal analysis of (2.6) and

(2.7), which are then used with (4.4) to find the transfer functions for resonance modulation and coupling modulation.

4.2.1 Resonance Modulation

It was previously shown how changing the resonant frequency of a microring produces optical intensity modulation in Fig. 4.1. Here, the transfer function between index change and output power is derived. Substituting

$$\omega_r = \omega_{r0} + \Delta\omega_r \frac{e^{j\omega_m t}}{2} + \Delta\omega_r \frac{e^{-j\omega_m t}}{2} \tag{4.5}$$

and

$$a = a_0 + a_1^+ \frac{e^{j\omega_m t}}{2} + a_1^- \frac{e^{-j\omega_m t}}{2} \tag{4.6}$$

into (2.6) yields

$$\begin{aligned} & j\omega_0 a_0 e^{j\omega_0 t} + j\left(\omega_0 + \omega_m\right) a_1^+ \frac{e^{j(\omega_0+\omega_m)t}}{2} + j\left(\omega_0 - \omega_m\right) a_1^- \frac{e^{j(\omega_0-\omega_m)t}}{2} \\ & = \left(j\left[\omega_r + \Delta\omega_r \frac{e^{j\omega_m t}}{2} + \Delta\omega_r \frac{e^{-j\omega_m t}}{2} \right] - \frac{1}{\tau} \right)\left(a_0 e^{j\omega_0 t} + a_1^+ \frac{e^{j(\omega_0+\omega_m)t}}{2} + a_1^- \frac{e^{j(\omega_0-\omega_m)t}}{2} \right) \\ & - j\mu_e s_{i0} e^{j\omega_0 t} \end{aligned} \tag{4.7}$$

Examining (4.7), notice that the equation can be separated into three new equations, by equating terms that have the same oscillation frequency. Neglecting the higher order oscillation terms, and cancelling the common exponential factors in each case, yields

$$j\omega_0 a_0 = \left(j\omega_{r0} - \frac{1}{\tau} \right) a_0 - j\mu_e s_{i0} \tag{4.8}$$

$$j\left(\omega_0 + \omega_m\right) a_1^+ = \left(j\omega_{r0} - \frac{1}{\tau} \right) a_1 + \Delta\omega_r a_0 \tag{4.9}$$

$$j\left(\omega_0 - \omega_m\right) a_1^- = \left(j\omega_{r0} - \frac{1}{\tau} \right) a_1^- + \Delta\omega_r a_0 \tag{4.10}$$

which can then be solved for a_0, a_1^+, and a_1^- to obtain

$$a_0 = \frac{-j\mu_e}{j\delta + \frac{1}{\tau}} s_{i0} \tag{4.11}$$

$$a_1^+ = \frac{a_0}{j\left(\delta + \omega_m\right) + \frac{1}{\tau}} \Delta\omega_r \tag{4.12}$$

$$a_1^- = \frac{a_0}{j\left(\delta - \omega_m\right) + \frac{1}{\tau}} \Delta\omega_r \tag{4.13}$$

which are complex energy amplitudes at ω_0, $\omega_0 + \omega_m$, and $\omega_0 - \omega_m$. Using the fact that $s_{t1}^+ = -j\mu_e a_1^+$, $s_{t1}^- = -j\mu_e a_1^-$, and $s_{t0} = s_{i0} - j\mu_e a_0$, obtained from a similar small-signal analysis of (2.7), the carrier and sideband outputs are finally found to be

$$s_{t0} = \frac{j\delta + \frac{1}{\tau} - \frac{2}{\tau_e}}{j\delta + \frac{1}{\tau}} s_{i0} \tag{4.14}$$

$$s_{t1}^+ = \frac{\mu_e a_0}{j\left(\delta + \omega_m\right) + \frac{1}{\tau}} \Delta\omega_r \tag{4.15}$$

$$s_{t1}^- = \frac{\mu_e a_0}{j\left(\delta - \omega_m\right) + \frac{1}{\tau}} \Delta\omega_r . \tag{4.16}$$

The modulation transfer function is then calculated by substituting (4.14)-(4.16) into (4.4), using $\Delta\omega_r = -\omega_r \Delta n/n$, and carrying out some algebraic manipulation to ultimately find

$$H_n\left(\omega_m\right) = \frac{\omega_{r0}}{n_0} \frac{2\delta\mu_e^2 P_{in}}{\delta^2 + \frac{1}{\tau^2}} \frac{j\omega_m + \frac{1}{\tau}}{\left(j\omega_m\right)^2 + j\frac{2\omega_m}{\tau} + \frac{1}{\tau^2} + \delta^2} . \tag{4.17}$$

Finally, the response from index modulation to output power modulation becomes a second-order system that can be written in the standard normalized form as

$$H_n(\omega_m) = \delta \frac{8\omega_{r0}P_{in}}{n_0\omega_n^4\tau_e\tau} \frac{j\omega_m\tau + 1}{\left(j\frac{\omega_m}{\omega_n}\right)^2 + \left(j\frac{\omega_m}{\omega_n}\right)2\zeta + 1} \tag{4.18}$$

where $\omega_n^2 = \delta^2 + \tau^{-2}$ is the undamped natural frequency and $\zeta = 1/\tau\omega_n$ is the damping ratio. This normalization allows the frequency dependent factor of $H_n(\omega_m)$ to be unity at DC. The first factor of (4.18) is the DC gain of the transfer function, or DC modulation efficiency, and will be referred to as $\eta_n = |dP_{out}/dn| = |H_n(0)|$.

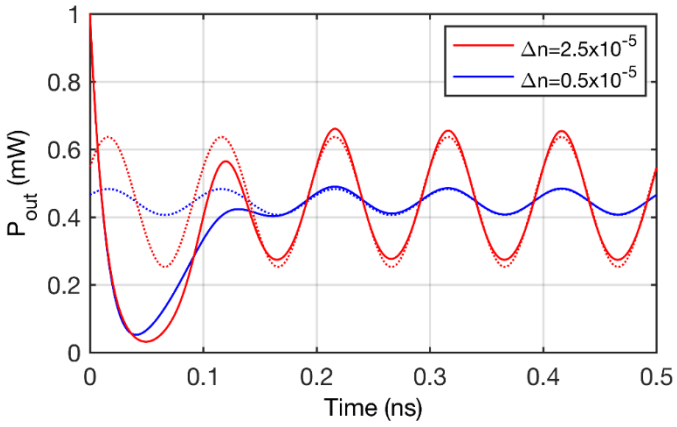

Fig. 4.2 Comparison of time-varying output power
Comparison between the simulated differential equations (solid curves) of (2.6) and (2.7), and the small-signal model (dotted curves) given by (4.18) and (4.3).

Fig. 4.2 shows the modulator output power in response to sinusoidal modulation at $f_m = \omega_m/2\pi$ =10 GHz, for two values of Δn. The solid curves are computed using (2.6) and (2.7), while the dashed curves are obtained from (4.18) and (4.3). The resonator parameters used in these simulations were n=3, L=62.8 μm (a ring radius of R=10 μm), κ_e=0.15, α=5 dB/cm, δ=2 GHz, P_{in}=1 mW, and m=121 so that the operation is near a resonant wavelength of λ_r=1.558 μm. Also, in this example f_n =

$\omega_n/2\pi$ =4.3 GHz and ζ=0.868. Fig. 4.2 shows that in the steady-state, after the initial transient response of the solid curves has settled (after about five times τ_p), the small-signal model agrees very well with the numerically simulated differential equation.

The frequency response given by (4.18) is plotted in Fig. 4.3a, with CR swept from strongly undercoupled (CR<1) to strongly overcoupled (CR>1). The same resonator parameters have been used that were given in the previous paragraph,

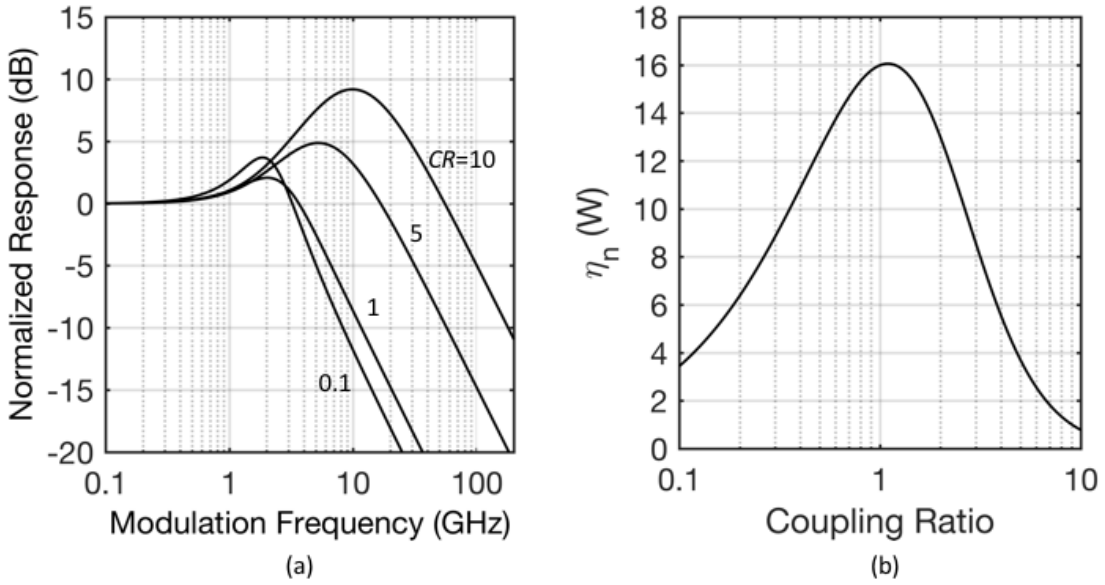

Fig. 4.3 Resonance-modulated frequency response
Normalized frequency response (a) with coupling ratio as a parameter. Modulation slope efficiency vs. coupling ratio (b).

except the coupling ratio has been varied by holding α constant and varying κ_e. The normalized magnitude responses in Fig. 4.3a show that the 3dB bandwidth of the modulator may be increased by increasing the coupling ratio. As the coupling ratio increases the photon lifetime decreases, thereby increasing ω_n as well as the 3dB bandwidth. Note that this bandwidth extension comes at the cost of reduced modulation efficiency, and therefore an increase in power consumption. Fig. 4.3b shows that η_n is

actually at a maximum near critical coupling, while in the heavily overcoupled case of *CR*=10, η_n is reduced by over a factor of ten.

We can find a simplified expression for η_n by setting the modulator to critical coupling (*CR*=1), where Fig. 4.3 showed that the efficiency is near maximum. Setting ω_m=0 and $\tau_e^{-1} = \tau_\ell^{-1}$ in (4.18) and simplifying yields

$$\eta_n = \frac{2\tau^2\delta}{\left(1+\tau^2\delta^2\right)^2}\frac{\omega_r}{n_0}P_{in} \tag{4.19}$$

for critically coupled microring modulators. Further simplification is obtained by specifying that the frequency detuning be equal to one half of the resonator linewidth ($|\delta| = \Delta\upsilon/2$). This value of detuning results in an insertion loss of IL=3 dB, which is the same IL of a Mach-Zehnder modulator, biased at the linear operating point. Setting $|\delta| = \Delta\upsilon/2$ in (4.19), the modulation efficiency reduces to

$$\eta_n = \frac{\omega_{r0}\tau_p}{n_0}P_{in} = \frac{Q}{n_0}P_{in}, \tag{4.20}$$

which explicitly shows that for index modulation in a microring, the efficiency is proportional to the photon lifetime, or quality factor, of the cavity. When *CR*=1 and $|\delta| = \Delta\upsilon/2$, it is also possible to find a simple expression for the 3dB modulation bandwidth ω_{3dB}. Taking the squared absolute value of the frequency-dependent portion in (4.18), setting the result equal to 1/2, and then solving for $\omega_m = \omega_{3dB}$ yields

$$\omega_{3dB} = \frac{\Delta\omega}{2}\sqrt{2\left(2+\sqrt{5}\right)} = \frac{1}{2\tau_p}\sqrt{2\left(2+\sqrt{5}\right)} \tag{4.21}$$

and shows that the modulation cutoff frequency is proportional to the cavity linewidth, or inversely proportional to the photon lifetime. Note that this exact solution for ω_{3dB}

agrees well with the approximate result derived in [42]. Lastly, the DC frequency chirp parameter $\alpha_H = -2P_{out}(d\theta/dP_{out})$ can also be determined for the critically coupled modulator [43, 44]. The phase angle of the output field is determined from (2.14) to be $\theta = \tan^{-1}[1/(\tau\delta)]$ which yields

$$\frac{\partial\theta}{\partial n} = -\frac{\tau}{1+\tau^2\delta^2}\frac{\omega_r}{n_0} \ . \tag{4.22}$$

Using (4.19), (4.22), and (2.14), the chirp parameter simply becomes

$$\alpha_H = -2P_{out}\frac{\partial\theta}{\partial P_{out}} = -2\left|H_t(\delta)\right|^2 P_{in}\frac{\partial\theta}{\partial n}\frac{\partial n}{\partial P_{out}} = -2\tau_p\delta \, . \tag{4.23}$$

In the following section the small-signal behavior of the CM-MR is analyzed, using the same procedure followed above.

4.2.2 Coupling Modulation

Coupling-modulated microrings are interesting because the modulation speed is not fundamentally limited by the photon lifetime of the cavity [38, 39]. Fig. 4.4a shows a possible topology for a microring modulator, where coupling control is achieved using a 2-by-2 MZM operated in a push-pull configuration (shown in the dotted box). Fig. 4.4b illustrates this type of modulation, where the depth of the notch is adjusted through a change in κ_e thereby modulating the output power of the microring.

The transfer function for coupling modulation is obtained in this section by applying the same procedure used previously for index modulation. For the sake of brevity the derivations for the sideband amplitudes are omitted. Note, however, that they are obtained in the same manner as in the previous section, by inserting

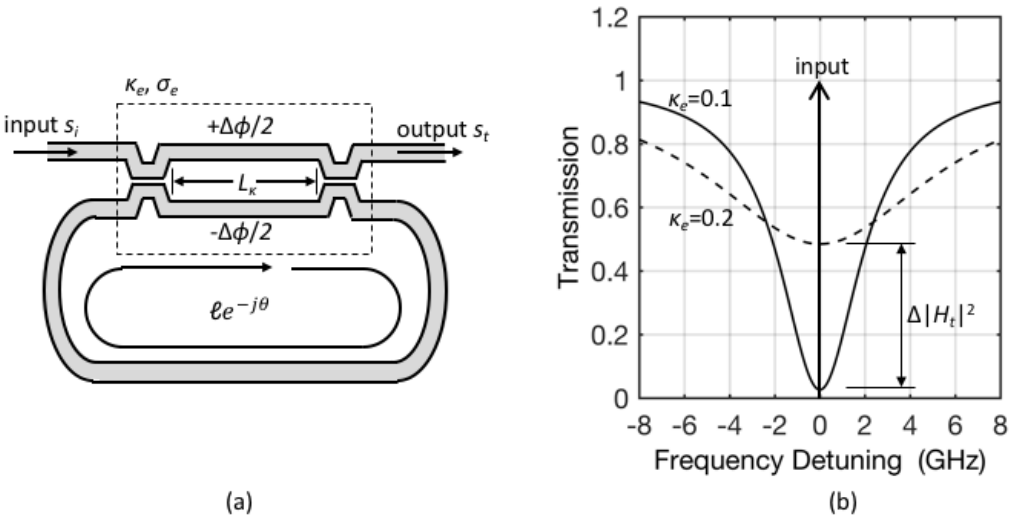

Fig. 4.4 Coupling-modulated microring
A microring resonator utilizing a Mach-Zehnder interferometer for tunable coupling (a). Illustration of transmission modulation by varying the coupling coefficient (b).

$$\mu_e = \mu_{e0} + \Delta\mu_e \frac{e^{j\omega_m t}}{2} + \Delta\mu_e \frac{e^{-j\omega_m t}}{2}$$

and

$$a = a_0 e^{j\omega_0 t} + a_1^+ \frac{e^{j(\omega_0+\omega_m)t}}{2} + a_1^- \frac{e^{j(\omega_0-\omega_m)t}}{2}$$

into (2.6). The result of the small-signal analysis yields

$$s_{t1}^+ = j\mu_e \frac{\mu_e a_0 + j s_i}{j(\delta + \omega_m) + \tau^{-1}} \Delta\mu_e - j a_0 \Delta\mu_e \tag{4.24}$$

and

$$s_{t1}^- = j\mu_e \frac{\mu_e a_0 + j s_i}{j(\delta - \omega_m) + \tau^{-1}} \Delta\mu_e - j a_0 \Delta\mu_e \tag{4.25}$$

while s_{t0} is given by (4.14). Using the fact that $\Delta\mu_e = \Delta\kappa_e/\sqrt{T}$ and substituting (4.24) , (4.25), and (4.14) into (4.4) the transfer function is found to be

$$H_\kappa(\omega_m) = -\frac{G_0 K_0}{\omega_n^2} \frac{\frac{j\omega_m}{K_0}\left[\left(\tau_e^{-1} - \tau^{-1}\right)^2 + \delta^2\right] + 1}{\left(j\frac{\omega_m}{\omega_n}\right)^2 + \left(j\frac{\omega_m}{\omega_n}\right)2\zeta + 1} + G_0\left(\tau_e^{-1} - \tau^{-1}\right) \quad (4.26)$$

where $G_0 = 2\kappa_e P_{in}/(T\omega_n^2)$ and

$$K_0 = \frac{\left(\tau_e - \tau\right)^2\left(\tau_e + \tau\right)}{\left(\tau_e \tau\right)^3} + \frac{\delta^2}{\tau} \ . \quad (4.27)$$

This is a general result that is valid for any coupling ratio or frequency detuning. Typically however, this type of modulator would be operated with the input wavelength on resonance of the cavity, in order to maximize the modulation efficiency. In this case, when δ=0, (4.26) reduces to a much simpler form of

$$H_\kappa(\omega_m) = -\frac{4\kappa_e \tau_p P_{in}}{T}\left(\left|H_{t0}\right|^2 \frac{j\omega_m\tau + 1}{\left(j\omega_m/\omega_n\right)^2 + \left(j\omega_m/\omega_n\right)2\zeta + 1} + H_{t0}\right) \quad (4.28)$$

where $H_{t0} = H_t(0)$ is given by (2.14). Looking at this result, it is interesting to notice that the response consists of two terms, one which is frequency independent. This means that the output power of the modulator can change instantaneously in response to a change in κ_e. This is the reason that coupling modulated microrings have been recently studied, because the modulation rate is not fundamentally limited by the photon lifetime of the resonator [38, 39, 45].

The result given by (4.28) is the modulation response in terms of changes in the coupling coefficient κ_e. In practice, a 2-by-2 Mach Zehnder modulator or a tunable directional coupler may be employed to implement the coupling control [39, 43, 44]. In both types of couplers, the coupling strength is controlled by inducing refractive index changes in the device. Therefore, in order to compare coupling-modulated

microrings to index-modulated microrings, the 2-by-2 MZM shown in Fig. 4.4a is considered, and then the change in coupling coefficient $\Delta\kappa_e$ is found, in response to index change Δn in the arms of the interferometer. For the 2-by-2 MZM operated in the push-pull configuration, the coupling coefficient is given by $\kappa_e = \sin(\phi_d/2)$ where $\phi_d = \omega L_\kappa \Delta n/c$ is the phase difference in the MZI arms, ω is the optical frequency, L_κ is the length of the MZI arms, and Δn is the index difference in the arms [43]. Differentiating κ_e with respect to n yields $\Delta\kappa_e = \omega L_k(1-k_e^2)^{1/2}/(2c)\cdot\Delta n$ as the small-signal relation between index change and the coupling coefficient. This result is used with (4.28) to write the response in terms of index change as

$$H_{\kappa,n}(\omega_m) = -\frac{2\kappa_e Q P_{in}}{n}\frac{L_\kappa}{L}\left(|H_{t0}|^2\frac{j\omega\tau+1}{(j\omega_m/\omega_n)^2+(j\omega_m/\omega_n)2\zeta+1}+H_{t0}\right) \tag{4.29}$$

where it is noticed that, as was the case for index modulation, the response is proportional to the quality factor of the cavity. The added subscript in (4.29) indicates that the transfer function now represents changes in output power due to changes in the refractive index of the MZM coupler. Unlike index modulation, the response is also proportional to κ_e which is small when Q is large, and therefore will act to weaken the response of the coupling modulated resonator. The response is also proportional to the ratio L_κ/L, indicating that the coupling region should occupy as much of the ring circumference as possible. Of course there is a limit to the maximum obtainable value of L_κ/L, so the maximum practical value of L_κ is considered to be one quarter of the total ring length L, in the following discussion.

Fig. 4.5a shows several frequency responses for the CM-MR, with varying coupling ratios. The optical carrier has been placed on resonance (δ=0), the ring length

is L=800 μm, L_κ=200 μm, and α=5 dB/cm. This ring length matches that of the fabricated modulator reported in [39]. The most important feature to notice is

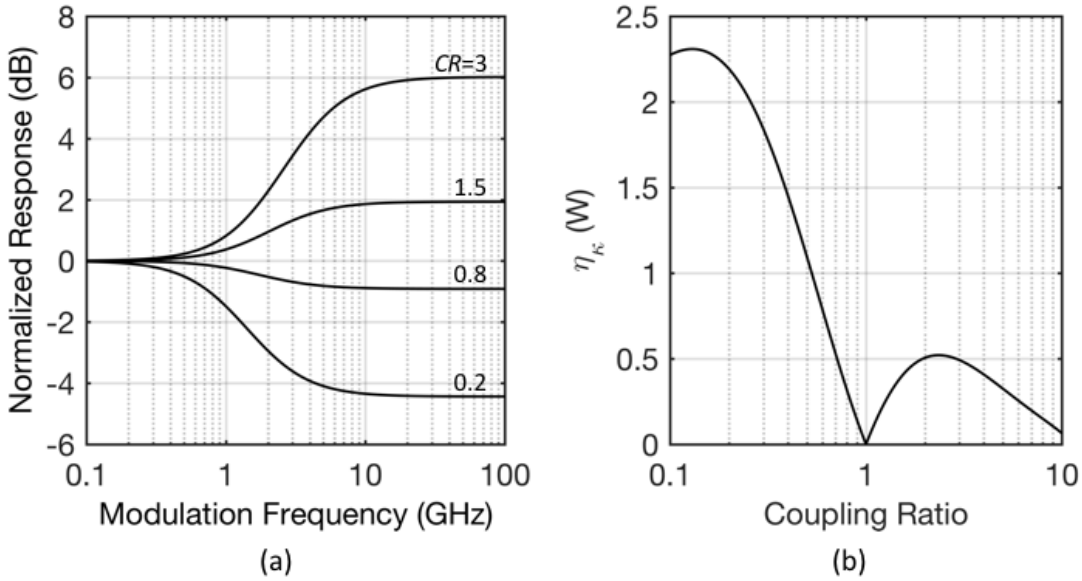

Fig. 4.5 Coupling-modulated frequency response example
Normalized Response with coupling ratio as a parameter (a). Modulation slope efficiency vs. coupling ratio.

that, due to the frequency independent term in (4.29), the response has no high frequency roll off. Unlike the RM-MR, the speed of the CM-MR is not fundamentally limited by the photon lifetime of the resonator, since the output power can change instantaneously in response to a change in coupling strength. Also seen, for undercoupling, the response steps down beyond the natural frequency, with the magnitude of the step increasing for smaller values of *CR*. For overcoupling, the response increases beyond the natural frequency, with a larger increase for larger values of *CR*. The response flattens near critical coupling, but as shown in Fig. 7b, the modulation efficiency η_κ=$|H_\kappa(0)|$ $\eta_\kappa = \left|H_{k,n}(0)\right|$ is significantly reduced near critical coupling and the modulation vanishes completely at *CR*=1 since for critical coupling

H_{t0}=0. Fig. 4.5b also suggests that a coupling modulated microring should be operated in the undercoupled region, in order to obtain the largest possible η_κ.

An expression for the DC modulation efficiency is obtained from (4.29) by setting ω_m=0 and rewriting H_{t0} as $H_{t0} = (1 - CR)/(1 + CR)$, which provides

$$\eta_\kappa = \left| -4\kappa_e \sqrt{1-\kappa_e^2}\, \frac{Q}{n} \frac{L_\kappa}{L} \frac{1-CR}{(1+CR)^2} P_{in} \right| \tag{4.30}$$

as the result. In order to compare this value to that of a MZM and the result from (4.20) , the modulator should again be configured to have a 3-dB insertion loss. Depending on whether the modulator is overcoupled or undercoupled, there are two cases where the modulator has IL=3 dB. Setting $|H_{t0}|^2$=1/2 these appropriate conditions are found to be CR=3+2·2$^{1/2}$ and CR=3-2·2$^{1/2}$, for overcoupling and undercoupling, respectively. With these two values of CR determined, the modulation efficiency at IL=3 dB becomes

$$\eta_\kappa = \kappa_e \sqrt{1-\kappa_e^2}\, \frac{Q}{n} \frac{L_\kappa}{L} \left(\sqrt{2}-1\right) P_{in} \tag{4.31}$$

for the overcoupled case, and

$$\eta_\kappa = \kappa_e \sqrt{1-\kappa_e^2}\, \frac{Q}{n} \frac{L_\kappa}{L} \left(\sqrt{2}+1\right) P_{in} \tag{4.32}$$

for the undercoupled case. Since κ_e is generally small in the undercoupled case, this result can be simplified using the approximation $\sqrt{1-\kappa_e^2} \approx 1$.

4.3 Model Validation

In a recent report, microring modulators were demonstrated for both coupling and resonance modulation. The devices were fabricated using the IBM Silicon CMOS

Integrated Nanophotonics process [46, 47], and used PN junction phase shifters to control the refractive index via the injection of free carriers [39]. A microscope image of one of the devices in shown in Fig. 4.6. Each modulator contained a phase shifter within the ring as well as a 2-by-2 MZM for coupling control, and therefore the devices could operate as resonance-modulated rings as well as coupling-modulated rings. Also the devices contained resistive thermal tuners, so that the DC resonant frequency could be adjusted via the thermooptic effect. The MZM couplers were implemented with the same PN junction phase shifters and were driven in push-pull mode. In order to isolate the optically limited response from the influence of the device electrodes, reference MZMs with an identical structure as used for coupling control were tested, and the obtained frequency response was then used to calibrate out that contribution to the overall response.

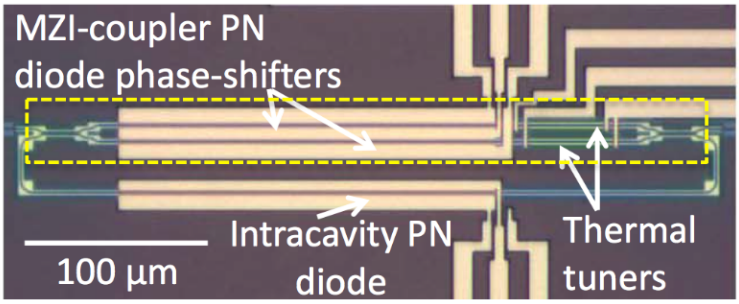

Fig. 4.6 Fabricated microring modulator image
Microscope image of the fabricated microring modulator reported in [39]. The device is constructed such that both resonance and coupling modulation are possible.

Fig. 4.7 shows the experimental data for both types of modulation. Two values of detuning are shown for index modulation, while for coupling modulation the carrier was aligned to the microring resonance. Also shown, by the dashed curves, are the small-signal frequency responses calculated from (4.18) and (4.29) using the parameters provided in [39]. It is seen that the results derived above fit well with the

experimental results, accurately capturing the optically limited dynamics of the index modulated ring as well as the reduced damping that results from larger detuning frequency. The coupling-modulated responses also agree well, and are relatively flat since the ring is near critical coupling, a characteristic which was illustrated in Fig. 4.5.

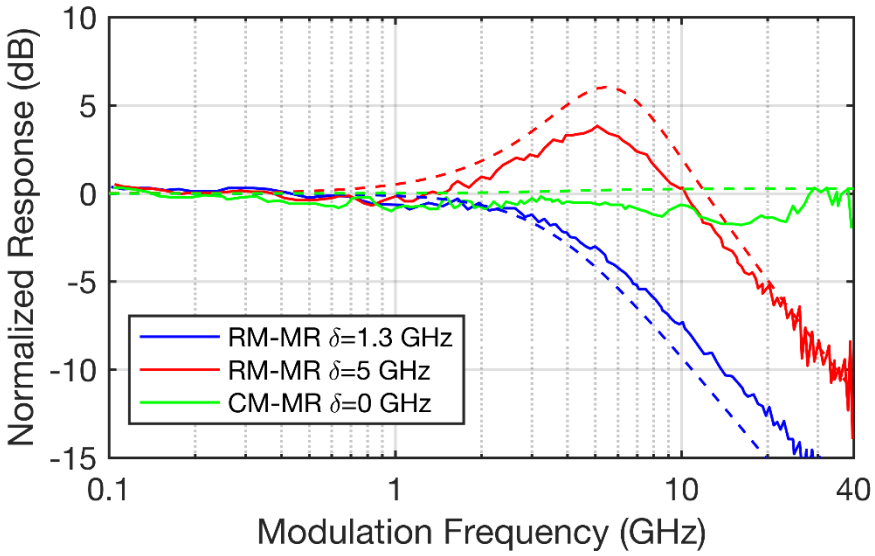

Fig. 4.7 Experimental comparison
Comparison of the transfer functions given by (4.18) and (4.29) to the experimental data reported in [39]. Solid curves are measurements and dotted curves result from the small-signal analysis. The parameters of the modulator are L=800 μm, $\Delta v = 6$ GHz, λ_r=1550 nm, FSR=84 GHz, and CR=0.9387.

4.4 Discussion

Using the results of sections 4.2.1 and 4.2.2 the merits of both types of modulators can now be compared in terms of efficiency, bandwidth, and footprint. In order to make fair comparisons, the insertion loss of each device is set equal to IL=3 dB since this is the insertion loss of a MZM operating at the linear bias point, where the modulation efficiency is maximum. Thus, the widely deployed and understood MZM performance becomes a benchmark for comparison with microring modulators. Note that this is the insertion loss introduced due to the operating point of the

modulator, additional insertion loss is introduced in the input and output waveguides of the device, and will reduce the modulation efficiency due to the reduction of P_{in}.

The ideal MZM output power is given by

$$P_{out} = P_n e^{-\alpha L} \cos^2\left(\frac{\phi_d + \phi_0}{2}\right) \tag{4.33}$$

where $\phi_d = \omega L n_d / c$ is the phase difference between the MZM arms, n_d is the difference in effective index between the arms, L is the modulator length, ω is the frequency of the input CW light, ϕ_0 is the bias point phase difference between the arms, and α is the attenuation coefficient in the MZM waveguides. Setting the MZM at the linear bias point, $\phi_0 = \pi/2$, and differentiating (4.33) with respect to n_d yields

$$\eta_{MZM} = \left|\frac{dP_{out}}{dn_d}\right| = \frac{P_{in}}{2} e^{-\alpha L} \cos\phi_d \frac{2\pi L}{\lambda} \approx e^{-\alpha L} \frac{\pi L}{\lambda} P_{in} \tag{4.34}$$

as the MZM modulation efficiency when ϕ_d is small, i.e. small-signal modulation.

Fig. 4.8 shows the modulation efficiency versus α, using (4.20), (4.31), (4.32), and, (4.34) for RM-MR, CM-MR, and the MZM. The loss coefficient α depends on which material system the modulators are built in as well as the fabrication quality of the waveguide sidewalls. First, it is seen that the resonance-modulated microring (blue curve) has the highest efficiency for all values of α, and also has the smallest footprint of ~20x20 μm^2. The 3-dB bandwidth of the RM-MR, given by Eq. (4.21), is

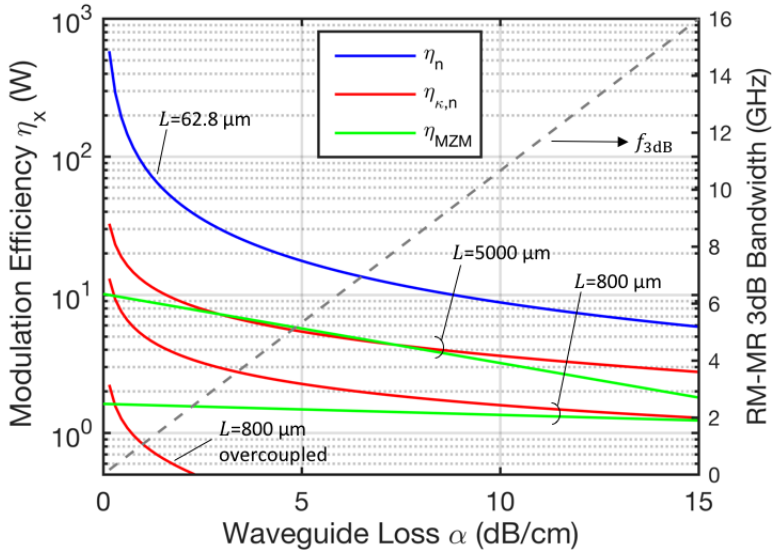

Fig. 4.8 Slope efficiency comparison
Comparison of slope efficiencies as a function of waveguide loss α. For the RM-MR, the 3dB bandwidth is shown on the right y-axis.

shown on the right-hand side of Fig. 4.8 and is increasing with α as the linewidth also increases, at the expense of efficiency. One interesting property of this type of modulator is that, for critical coupling, the η_n vs. α curve is independent of L, which can be seen by rewriting (4.20) as

$$\eta_n = \frac{Q}{n} P_{in} = \frac{\omega_r \tau_p}{n} P_{in} = \frac{\omega_r}{n} \frac{T}{\alpha L} \frac{P_{in}}{1+CR} = \frac{1}{2} \frac{\omega_r}{c\alpha} P_{in} \tag{4.35}$$

and therefore all critically-coupled and half linewidth-detuned RM-MR modulators have the same efficiency for a given waveguide loss, resonant frequency, and optical input power. RM-MR modulators can therefore be scaled down in size without reducing modulation efficiency.

The CM-MR modulation efficiencies are shown in Fig. 4.8 by the red curves for two values of L, and IL=3 dB. First note that the 3-dB modulation bandwidth for the CM-MR and MZM is not plotted because, when the electrical response of the modulator electrode is neglected, the frequency response for these modulators does not

roll off at high frequencies. Also note that for the overcoupled situation, the efficiency is the weakest due to the low Q obtained when $CR=3+2\cdot 2^{1/2}$ and will not be considered further. The undercoupled CM-MR, however has a much stronger response due to the higher Q when $CR=3-2\cdot 2^{1/2}$, and is shown for L=800 μm and L=5 mm where L_κ/L=4 is assumed. For comparison, MZM efficiencies are plotted (green curves) with the same two values of L. When L=800 μm, the CM-MR is more efficient the MZM across all values of α. When the length is increased to L=5000 μm however, the efficiencies are approximately equal when the loss is greater than α=3 dB/cm. If the length were increased further, the MZM would become more efficient since $\eta_{MZM} \propto L$, as seen in (4.34), while for the CM-MR $\eta_{n,k} \propto \sqrt{L}$. The latter relation can be seen by rearranging Eq. (4.32), with L_κ/L=4, to show

$$\eta_{\kappa,n} = \frac{\omega_r}{n}\frac{1}{c}\sqrt{\frac{L}{\alpha}}\frac{\sqrt{CR}}{1+CR}\left(1+\sqrt{2}\right)P_{in} \tag{4.36}$$

which also reveals that the CM-MR is less sensitive to variations in α than the RM-MR since $\eta_{\kappa,n} \propto 1/\sqrt{\alpha}$ while $\eta_n \propto 1/\alpha$. The footprints of the CM-MR and MZM, for equal L, are similar but with different aspect ratios. For example, in [39] and [48], CM-MRs were demonstrated with an elongated racetrack topology, such that the coupling region was approximately one half of the total ring length, i.e. $L_\kappa/L\approx$1/2. In these situations the CM-MR is about half the length of an MZM with the same L, but also about twice as wide.

In sections 4.2.1 and 4.2.2 the modulation efficiencies were derived in terms of refractive index change, without concern for specific electrode structures, or physical mechanisms responsible for the index control and the contribution to the modulator

operation. This allowed analysis of the optically-limited modulation response, and although the results suggest which modulators would be most power efficient for certain configurations, the power dissipation was not quantified. The analysis can be extended to provide estimates for power consumption, however, if the properties of a certain device configuration are known, i.e. the voltage-to-index relationship $\eta_e = |dn/dV|$ which will be referred to as the electrode efficiency. This parameter encapsulates the physical mechanism for the index change, as well as the confinement factor between the active waveguide region and optical mode. Knowing a specific η_e, the small-signal output power of a given modulator can be written as

$$\Delta p = MP_{DC} = \left|\frac{dp}{dn}\right|\left|\frac{dn}{dV}\right|\Delta V = \eta_x \eta_e \Delta V \tag{4.37}$$

where $M = \Delta p / P_{DC}$ is the desired modulation depth and η_x is one of the modulation efficiencies previously derived, depending on which type of modulator is to be analyzed. Solving for ΔV in (4.37) gives $\Delta V = MP_{DC}/(\eta_x \eta_e)$ as the required peak drive voltage required to achieve a certain modulation depth. The average dynamic power dissipation, when the electrode is driven with a DC-balanced pseudo random bit stream (PRBS) [49], can be expressed as $P_{dyn} = (1/4)CV_{pp}^2 BR$ with V_{pp} being the peak-to-peak amplitude of driving voltage signal ($V_{pp} = 2\Delta V$), *C* is the capacitance of the electrode structure, and *BR* is the bitrate of the input PRBS. This expression then becomes

$$P_{dyn} = \frac{1}{4} C \left(\frac{2MP_{DC}}{\eta_x \eta_e} \right)^2 BR \tag{4.38}$$

as the dynamic power dissipation if a certain C and η_e is known. For example in silicon-on-insulator (SOI) platforms, modulators based on the metal-oxide-semiconductor

(MOS) structure or lateral/vertical p-n junctions have been well represented in the literature [50]. Both structures rely on the plasma dispersion effect, which alters the refractive index in the structure by manipulating the free carrier concentration in the waveguides either through field-effect in the MOS devices, or carrier injection/depletion in the p-n junction devices. In [51], MOS electrode structures are investigated and the authors report an electrode efficiency of η_e=2.32 x 10^{-5} V^{-1} and a capacitance of C=26.4 pF for a 3.45 mm long electrode, to give a capacitance per unit length of C'=7.65 fF/μm. Using this information with Fig. 4.8 and (4.38), the dynamic power dissipation can be estimated, per Gbps of data modulation, for the modulators described in Fig. 4.8 when implemented with such a MOS structure. For example, when α=5 dB/cm the RM-MR consumes 258 μW/Gbps. When L=800 μm, the CM-MR consumes 49.7 mW/Gbps and the MZM consumes 1.7 W/Gbps. When L=5 mm, the dynamic power dissipation is also 49.7 mW/Gbps for the CM-MR and for the MZM it is 196 mW/Gbps. Note that even though in this case $\eta_{\kappa,n} \approx \eta_{MZM}$, the CM-MR consumes less power since $L_\kappa = L/4$ is used to calculate the capacitance while L is used for the MZM. It is also interesting that the power dissipated by the CM-RM does not change with increased L. This is because P_{dyn} is proportional to $C = C'L$ while $\eta_{\kappa,n}$ is proportional to $\sqrt{L}$, and therefore the power consumption of the CM-MR is independent of L. The required voltage swing however, will decrease with increasing L. This is important since the voltage swings available to the modulator are often determined by the drive circuitry, which for CMOS circuits, would typically be limited to V_{pp}=1-2 V.

To verify the validity of (4.38), the predicted P_{dyn} is compared to the quoted value for a depletion-mode, PN junction based RM-MR presented in [37]. In that work,

the authors report a wavelength shift of $|d\lambda_r/dV|$=10 pm/V. Using the relation $d\lambda_r/dn = (\lambda_r/n)(L_a/L)$, where L_a is the length of the active waveguide in the ring, the wavelength shift is converted to the electrode efficiency through $\eta_e = |dn/dV| = |d\lambda_r/dV| \cdot |dn/d\lambda_r|$. Using n=4, typical for SOI waveguides [52], and L_a/L≈0.7 the electrode efficiency becomes η_e=4.31e-5 V^{-1}. The reported RM-MR quality factor is 8300, and the input optical power was approximately P_{in}=50.2 μW which yields η_n=0.104 W, given by (4.20). The approximate capacitance of the electrode is C=125 fF, the DC optical output power is P_{DC}=12.6 μW, and an extinction ratio ER=3 dB (M=1/3). The estimate therefore, using the small-signal analysis above, is found by substituting these parameters into (4.38) to obtain P_{dyn}=109 μW/Gbps which agrees reasonably well with the reported value of 120 μW/Gbps.

In addition to the dynamic power dissipation, there will be power consumed by biasing and stabilizing the modulators. For both types of microring modulators, it is crucial that the resonance be correctly aligned to the incoming laser wavelength, or modulation will be impaired or lost completely. The resonant frequency in microrings is often tuned by placing heater pads within the ring, which tune the resonance through the thermooptic effect, and also add to the total power consumption of the device. In addition, since resonant modulators are very sensitive to index variation, these modulators will require stabilization circuitry to maintain the alignment of the input wavelength to the resonance due to environmental temperature fluctuations [53]. In general these contributions to the total power dissipation are often neglected in the literature, as well as the laser power, but should be accounted for when comparing modulators and calculating power budgets for optical transmitters.

4.5 Conclusion

We have derived the small-signal transfer functions for both RM-MR and CM-MR modulators on the basis of CMT. From these results the modulation efficiencies were obtained along with the 3-dB modulation bandwidth. To validate the developed small-signal model, the transfer functions were compared with experimental data, and found to agree well. Modulation efficiencies for the RM-MR and CM-MR modulators were compared with each other and with the common MZM. Finally, an expression for the dynamic power dissipation was presented and found to provide good agreement to data reported in the literature.

5 Chapter 5: Resonant-Cavity Enhanced Thyristor Photodetector

5.1 Introduction

The number of short reach optical interconnects deployed in data communication networks is increasing to meet requirements for more throughput in data centers, and high performance computing systems [3, 54]. This is due to advantages over electrical interconnects such as increased bandwidth, reduced cable density, longer link distances enabled by low loss optical fiber, and low transceiver power consumption. However, as total bandwidth is scaled up to keep pace with growing demands, thermal requirements dictate that increased performance be accompanied by more efficient, lower power transceivers.

Typical transceivers utilize vertical cavity surface emitting lasers (VCSELs) in transmitters and pin photodiode-based optical receivers, to perform the required electro-optic and opto-electric conversions. The receiver also incorporates a transimpedance amplifier (TIA), for current to voltage conversion, and limiting amplifiers (LA) to create voltage levels compatible with subsequent electronics [4, 55]. Because of the circuitry required to amplify the photodiode output, the receiver may be responsible for over 50% of the power consumed by the optical link [54], and therefore improvements in receiver efficiency can significantly decrease the total energy needed to power the expanding usage of short reach optical links. In the pursuit for higher bandwidth and more efficient conversion, a thyristor-based photoreceiver has been

proposed which has the potential to achieve lower overall power consumption, higher sensitivity, and high bandwidth [56].

The photoreceiver was described as an optoelectronic thyristor, containing n- and p-type modulation doped heterointerfaces located adjacent to quantum well (QW) channels. In addition to the anode and cathode contacts, electrical access to stored charge in the device is provided by contacting both sets of QW channels. The thyristor operates as a photoreceiver by switching between bistable operating points, in response to incoming optical pulses. An optical input to the thyristor produces photocurrent, which populates the QWs and triggers switching to the low impedance on-state. Without optical input, the contacts to the QW channels remove stored charge thereby allowing the device to unlatch and return to the high impedance off-state. Simulated results of this thyristor configuration show greater than 1 V output swing for 500 μW of input power, at a data rate of 40 Gbps [56]. The theoretical model for the thyristor-based photoreceiver is an extension of the analysis presented for the two-terminal device [57], in which the current-voltage characteristic is predicted and confirmed by experimental data. Three-terminal devices have also been fabricated that incorporated an injector contact to one of the QW sets, and the analytical framework presented agrees with device measurements [58]. These devices had anode contacts covering the device surface so measurement of the optoelectronic response was not possible.

In this chapter, experimental results are presented for a two-terminal thyristor device under optical illumination. An annular shaped anode contact provides an aperture that allows the optical signal to be coupled into the device. Also, since the optical absorption in the quantum wells is limited by small active region thickness, the

devices incorporates top and bottom distributed Bragg reflectors (DBR) to form a resonant cavity that enhances the quantum efficiency. The devices are characterized in terms of off-state photocurrent response, where the device behaves similar to a pin photodiode. Also, the lowering of switching voltage with input optical power is evaluated and the optical power needed to trigger switching is observed. Since the device does not incorporate the third and fourth terminals, device switch-off cannot be characterized. In addition, since the device is resonant, the spectral selectivity of these responses are investigated.

Section 5.2 describes the epitaxial layers for the thyristor detector along with the optical cavity design. Device fabrication is discussed in section 5.3 and the experimental results are presented in section 5.4. Discussion of the results is provided in section 5.5.

5.2 Epitaxial Layer Design and Characterization

The device material was grown by molecular beam epitaxy in a Varian Mod Gen II system, on a semi-insulating (SI) GaAs substrate, according to the layer sequence in Table 5.1. First, an undoped, 27.5 pair GaAs/AlAs DBR was grown to form the bottom mirror, followed by the thyristor epilayers. Silicon (carbon) doped GaAs and wide bandgap $Al_{0.7}Ga_{0.3}As$ layers form the n-type cathode (p-type anode) contact layers and bottom (upper) cladding regions, respectively. Undoped intermediate bandgap $Al_{0.15}Ga_{0.85}As$ layers of thickness d_{b1}=300 Å and d_{b2}=300 Å along with n- and p-type modulation dopings form potential barriers to the top and bottom active regions, which are comprised of sets of three $In_{0.2}Ga_{0.8}As$ quantum wells 60 Å thick, separated by 100 Å GaAs spacer layers. Uniting the upper and lower active

regions is a thick common-collector $Al_{0.15}Ga_{0.85}As$ layer with thickness d=5,200 Å. From top to bottom, the resulting structure is a p-i-n-i-p-i-n thyristor structure. The overall thickness of the thyristor cavity was designed to be 4.5-λ thick at the 980 nm design wavelength, a total thickness of L=12,400 Å.

Table 5.1 Epitaxial Layer Structure

Composition	Type	Doping Conc. (cm^{-3})	Thickness (Å)	Description
GaAs	p++	1.0e20	600	anode
GaAs	p+	7.0e18	650	
$Al_{0.70}Ga_{0.30}As$	P	5.0e17	1000	cladding
$Al_{0.15}Ga_{0.85}As$	i		300	n-side barrier (d_{b1})
$Al_{0.15}Ga_{0.85}As$	n+	3.5e18	80	modulation doping
GaAs	i		45	buffer
$In_{0.20}Ga_{0.80}As$ x3	i		60	upper MQW active region
GaAs x3	i		100	
$Al_{0.15}Ga_{0.85}As$	i		5200	common-collector (d)
GaAs x3	i		100	lower MQW active region
$In_{0.20}Ga_{0.80}As$ x3	i		60	
$Al_{0.15}Ga_{0.85}As$	i		75	buffer
$Al_{0.15}Ga_{0.85}As$	p+	7.0e18	25	modulation doping
$Al_{0.15}Ga_{0.85}As$	i		300	p-side barrier (d_{b2})
$Al_{0.70}Ga_{0.30}As$	N+	3.5e18	1000	cladding
GaAs	n+	3.5e18	2800	cathode
AlAs x27	i		845	27.5-pair DBR
GaAs x27	i		710	
AlAs	i		845	
GaAs Substrate	SI			

After the growth and prior to wafer processing, a reflectance measurement was performed to characterize the resonant wavelength of the epitaxial structure. Fig. 5.1a shows the measured reflectance spectrum, along with the results of a transfer

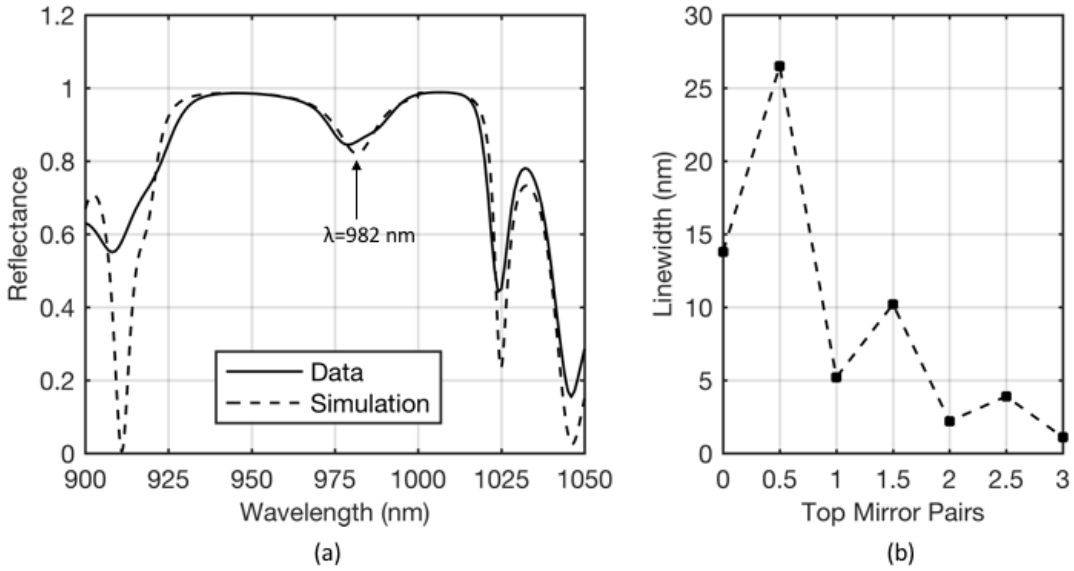

Fig. 5.1 Epi wafer characterization
Measured and simulated reflectance spectra (a) of the as-grown epitaxial stack. Resonance linewidth for varying number of top dielectric DBR mirror pairs (b).

matrix method (TMM) simulation [21, 59, 60]. The TMM results agree well with the data across the reflectance stopband, including capturing the resonant wavelength at 982 nm. The deviations from measurement at shorter wavelengths are likely due to inaccuracies in the refractive index models which, for shorter wavelengths, leads to larger errors in the propagation phase shifts incorporated in the TMM calculation.

The fabricated device utilizes a top DBR in order to enhance the cavity resonance. Continuing the TMM analyses, Fig. 5.1b shows the cavity linewidth as a function of the number of top mirror pairs. On resonance the detector responsivity will be enhanced by increasing the reflectance of the top DBR, though the spectral response will become narrower as the linewidth decreases, due to the increased cavity quality factor Q. Two top mirror pairs were deposited in order to maximize absorption, at the expense of a narrow linewidth of 2 nm, as seen in Fig. 5.1b. Measurement of the cavity linewidth is discussed in section 5.4.

5.3 Device Fabrication

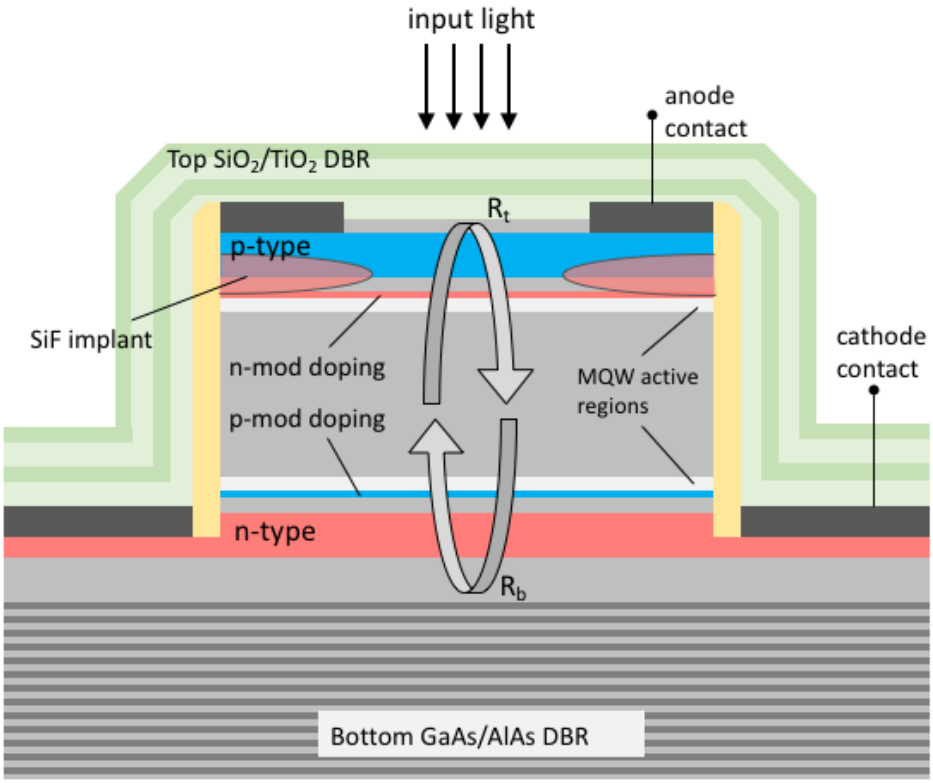

Fig. 5.2 Resonant thyristor detector cross section
Depiction of the device cross section following fabrication.

The device fabrication was performed as follows. A nitride layer was deposited and patterned to define the optical aperture (typically 8–16 μm in diameter). SiF ions were implanted to guide the photocurrent and the corresponding internally produced current components. Tungsten based metallurgy was then deposited, patterned and etched to define the top mesa. The etch was continued in the semiconductor to the n+ contact layer at the bottom of the structure. Then PECVD nitride was deposited and a high temperature rapid thermal anneal (RTA) at 850˚C and 15 seconds was performed to activate the implant. The RTA process conditions are chosen to provide sufficient activation, while minimizing diffusion of the charge sheet dopants, and has been seen

to not significantly impact the device characteristics. Next, Au-based ohmic contacts were applied to the n+ contact layer and the top anode metal, followed by an anneal step at 400˚C. Lastly, a mask was patterned to open the aperture and the nitride and metal layers were etched away to the semiconductor surface. The final step is to deposit pairs of SiO_2/TiO_2 layers to form a top DBR mirror for the detector cavity enhancement. Last, metal contact areas are formed by etching through the mirror. The finished device cross section in shown in Fig. 5.2.

5.4 Experimental Results

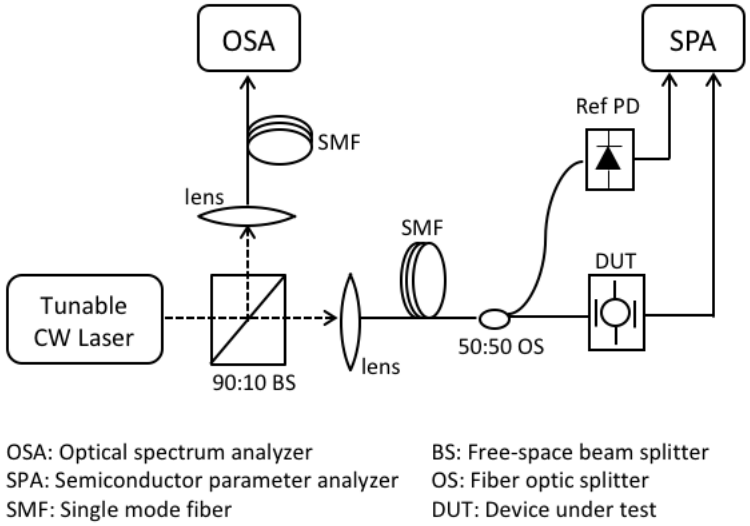

Fig. 5.3 Experimental setup
Experimental test setup for resonant-cavity photodetector characterization.

The two-terminal thyristor devices studied in this work were characterized with input light, as it transitions from the off- to on-state. The devices were probed with an optical input from a wavelength-tunable Ti:Sapphire laser (Spectra-Physics 3900), using cleaved single mode fiber. The experimental set up is shown in Fig. 5.3. A free-space beam splitter (BS) was used to tap off 10% of the laser output and direct it to an

optical spectrum analyzer (OSA Agilent 86140), in order to monitor the laser wavelength. The remaining power was coupled into single mode fiber (SMF) with a lens and then fed equally into a silicon reference photodiode (PD ThorLabs SM05PD1B) and the thyristor DUT, by using a 3-dB fiber optic splitter (OS). A semiconductor parameter analyzer (SPA Agilent 4155C) measured the I-V characteristics as the input power and wavelength were swept. The reference PD, with known responsivity (R_p=0.6 A/W at 980 nm), was monitored during testing in

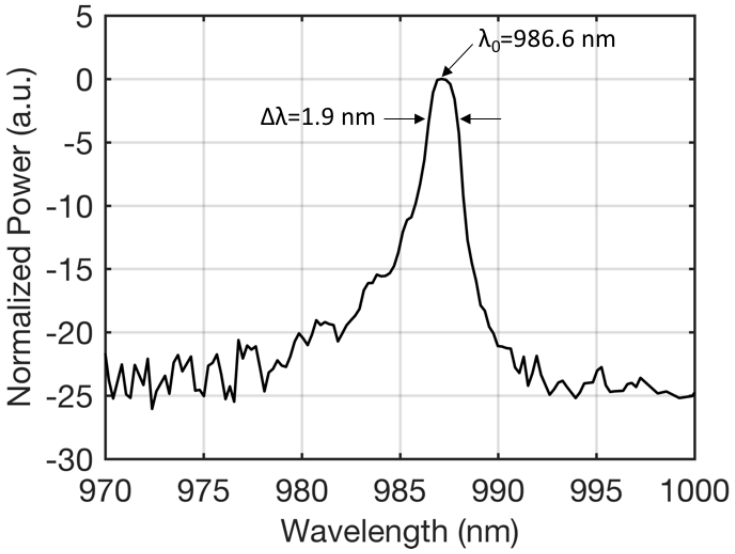

Fig. 5.4 Detector spontaneous emission spectrum
Measured spontaneous emission power spectrum of the detector. The device was forward biased in the on-state with 10 mA drive current.

order to calibrate the optical power level into the DUT. Light was coupled into the DUT at normal incidence. All measurements were taken at ambient room temperature and without any thermal stabilization.

Because the devices were processed using reticles cleaved from the original epi wafer, examining the linewidth of the cavity by reflectance measurement was not possible, due to sample size limitation of the reflectometer. Instead, The spontaneous

emission spectrum was measured by forcing 10 mA of current through the device, collecting the emission with single mode fiber, and directing the output to the OSA. Fig. 5.4 shows the measured spectrum, where the linewidth is about 1.9 nm and close to the predicted value of 2 nm shown in Fig. 5.1b, and the resonant wavelength is about 986.6nm.

Fig. 5.5a shows typical I-V curves for the detector, with varying levels of P_{in} and with the input tuned to the λ_0=986.6 nm resonant wavelength of the device. There are three distinct regions of operation: 1) a high impedance off-state for current less than ~100 μA, 2) a negative differential resistance region where the device is in regenerative positive feedback and forces the device to switch, and 3) a low impedance on-state for currents above ~800 μA. On a given current-voltage curve, the onset of switching is denoted by a switching voltage V_{sw} and switching current I_{sw}, while the onset of the on-state is denoted by a holding voltage V_h and holding current I_h. For example, with the laser off, the switching point is at V_{sw}=4.7 V and I_{sw}=83 μA, and the holding point is at V_h=1.9 V and I_h=830 μA. When the laser is

turned on, the optical input generates a photocurrent that populates the quantum wells, and reduces the switching voltage. As seen in Fig. 6, as P_{in} is increased from P_{in}=0 μW to P_{in}=403 μW the switching voltage is reduced by about 3.5 V, and the optical input has almost completely removed the high impedance off-state from the device. Fig. 5.5b shows a simple photoreceiver circuit where a load resistor R_L is connected from cathode to ground. The dashed line in Fig. 6a is the load line for R_L=1 kΩ, showing the operating points in the off- and on-states. The device turn-on occurs when the optical input power reduces V_{sw}, such that the I-V curve no longer intersects the load line in the off-state, causing the device to latch into the on-state operating point.

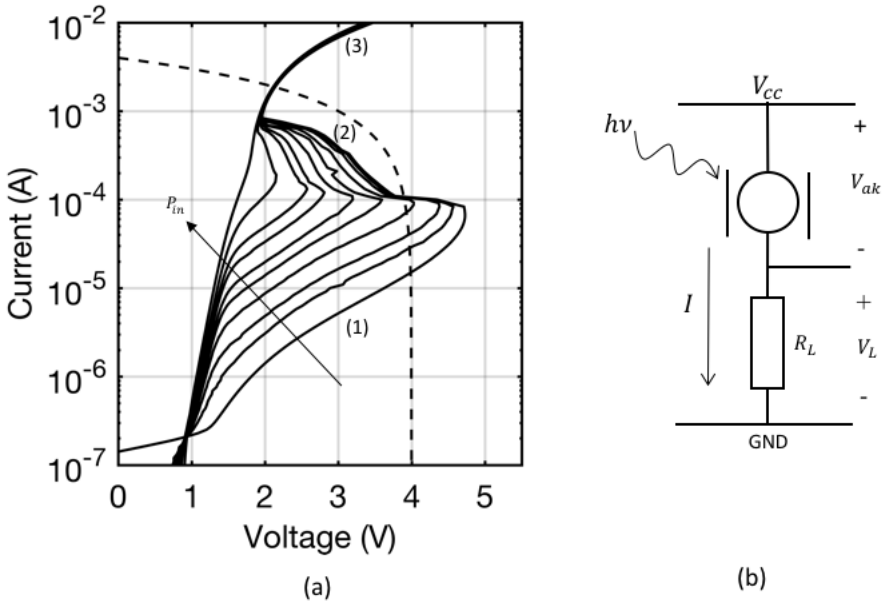

Fig. 5.5 Detector Characteristics
Thyristor I-V curves (a) for varying levels of P_{in}=[0, 3, 7, 17, 30, 43, 73, 102, 190, 409 μW]. The input light is tuned to match the device resonance at λ=986.6 nm. A simple photoreceiver circuit (b) with a load resistor connected between cathode and ground. The dashed curve shows the load line with a R_L=1 kΩ resistor and a supply voltage V_{cc}=4 V.

In Fig. 5.6 the current and switching voltage are shown versus the input optical power, with the laser on resonance at λ=986.6 nm. As seen in Fig. 5.6a, the device current increases linearly with P_{in}, and the slope of the response is steeper for increasing applied voltage bias V_{cc}. The slope efficiency $\eta_d = \Delta I/\Delta P_{in}$ of the detector response increases with bias since, as will be discussed in section 5.5, a larger bias yields more internal gain for the generated photocurrent. For a bias of V_{cc}=2, 3, and 4 V the slope efficiencies, obtained from linear fits to the data, are η_d=0.46, 1.45, and 3.96 A/W respectively. Also seen is an increased dark current due to larger voltage bias. Fig. 5.6b shows that as the input light is increased to P_{in}=73 μW the switching voltage is reduced, approximately linearly, by about two volts. A linear fit yields a switching efficiency parameter, denoted $\eta_{sw} = \Delta V_{sw}/\Delta P_{in}$, of about η_{sw}=-27 mV/μW. Also shown in Fig. 5.6b are the levels of V_{sw} that will trigger the device to

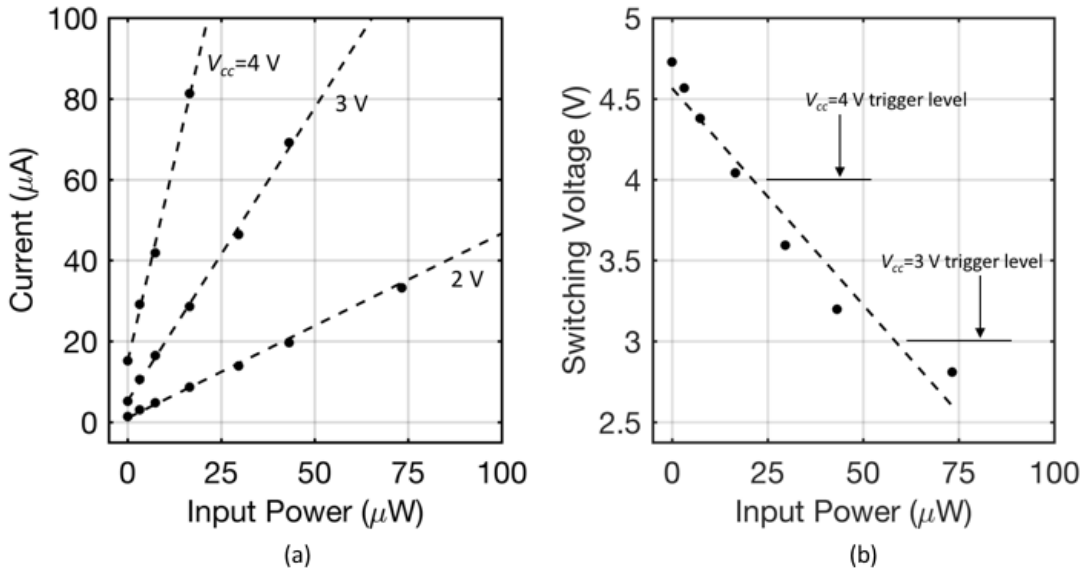

Fig. 5.6 On-resonance photoresponse
Device current at three bias voltages (a), and switching voltage (b), versus optical input power. For both measurements the input wavelength is on-resonance at λ=986.6 nm. The dashed lines are linear curve fits.

switch, when placed in a circuit that has that voltage as the supply. If the supply is 4 V then the device triggers for P_{in} > 20 μW, and P_{in} > 60 μW will switch the device when the supply is 3 V. Upon switching, the detector latches into the on-state as shown in Fig. 5.5a, where a R_L=1 kΩ load resistor intersects the device I-V characteristic at about 2.1 V and 2 mA of current. Thus, when the detector is switched on with P_{in}=20 μW, a large-signal current gain of 125 and an output voltage of V_L=1.9 V is obtained. Compared to conventional pin diode photodetectors, the device here shows relatively large dark currents likely arising from excess recombination centers, and will be addressed further in the section 5.5. While this limits the device sensitivity in general, optical power levels at the receiver in short-reach data links exceed tens of microwatts, making this detector suitable for this application. In terms of saturation power, the detector here operates as a switch, triggering when a certain optical input threshold is reached and is not intended to respond linearly at large input powers. This differentiates

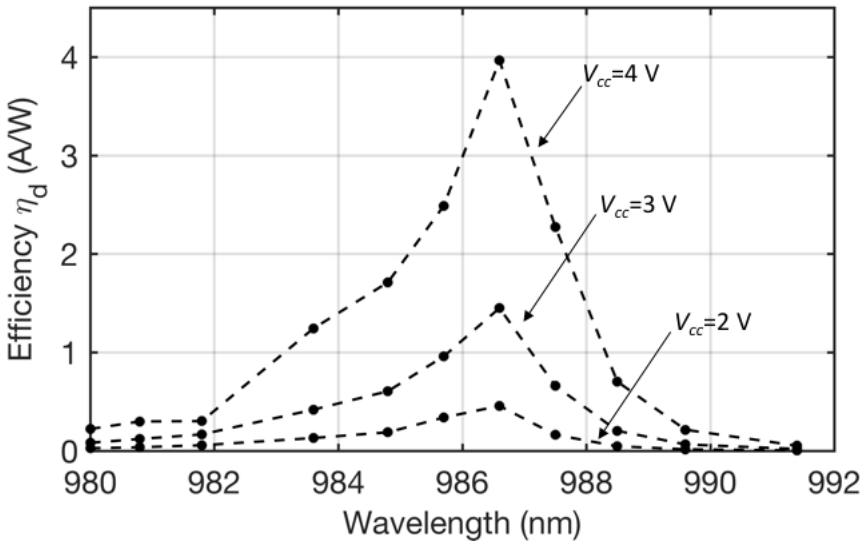

Fig. 5.7 Detector spectral response
Spectral dependence of the detector slope efficiency η_d, for three bias voltages. Measured data are shown by the markers and the dashed lines are to guide the eye.

the presented device from pin detectors, where operation into the milliwatt range is desired before exhibiting nonlinearities.

In order to examine the spectral dependence of η_d, the above measurements were repeated for input wavelengths spanning from 980 nm to 992 nm. At each wavelength, η_d was obtained at three bias voltages. The results are shown in Fig. 5.7, which shows that the response is strongest when the input light is tuned to the device resonance. Once again, for larger bias voltages the response is enhanced because the internal current gain in the device increases with bias. From Fig. 5.7, the FWHM of the response is about 2 nm and is independent of V_{cc}. However, since the absolute value of η_d increases with V_{cc}, then a bandwidth for which the slope efficiency exceeds a minimum can be defined. For example, at V_{cc}=4 V the bandwidth where η_d>1 A/W is greater than 5 nm. The useful spectral width of the detector is therefore not strictly limited to the FWHM of the cavity resonance.

5.5 Discussion

In section 5.4, the slope efficiency η_d of the detector was shown to increase with increasing bias voltage. This is in contrast to pin photodiodes, that have a constant responsivity when reverse biased. The difference in optoelectronic response between the detector in this work and conventional photodiodes, is that the thyristor exhibits internal bipolar current gain. The current-voltage characteristics for similar two- and three- terminal devices were previously analyzed in detail, and correlated well to experiment [57, 58]. Three-terminal thyristors were reported that incorporated an injector contact which allowed for electrical access to the n-type quantum wells [58]. By injecting current directly into the top active region, similar control over the

switching characteristic of the device was obtained as seen in Fig. 5.5a, though optoelectronic testing was not possible due to lack of an aperture in the anode contact. Without current injection, the switching voltage was similar to the present device with V_{sw}=4.1 V, though the switching current was lower, by about a factor of twenty, at a value of I_{sw}=3.8 μA. The previous fabrication process was without implantation, and the increased switching current seen here is possibly due to increased recombination centers in the implanted region, resulting from incomplete removal of lattice damage after RTA. Also note that device simulations based on the theory presented in [56-58] accurately predict the switching and holding voltages, but tend to underestimate the device current compared to current-voltage characteristics obtained from measurement. Excessive recombination due to surface-states on the device sidewalls, and recombination centers in the epilayers are suspected as contributing factors to this discrepancy, and are currently under investigation. The previously reported device analysis is summarized here, in terms of the current gain. First the current gain mechanism is described, then its value is extracted by decoupling it from η_d using an estimation of the quantum efficiency.

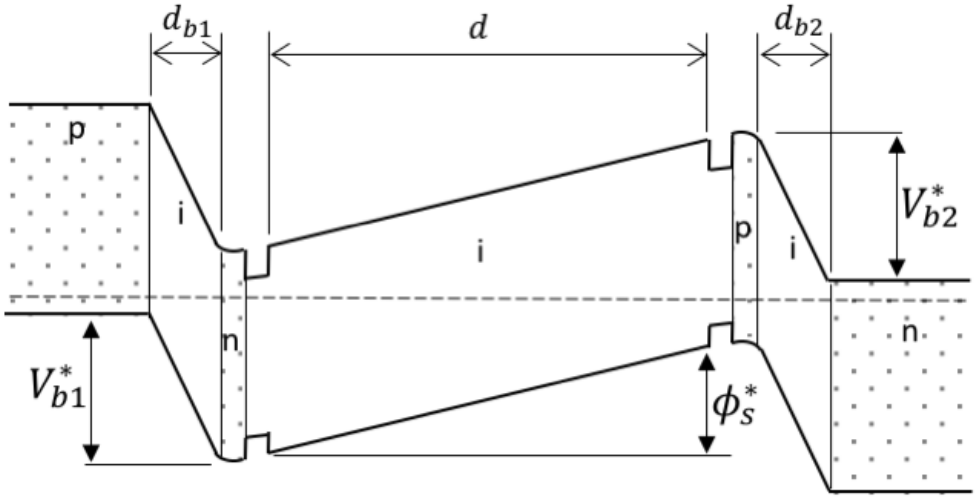

Fig. 5.8 Equilibrium energy band diagram
Simplified energy band diagram of the device in the off-state.

Fig. 5.8 shows a simplified energy band diagram for the detector in thermal equilibrium. The structure may be viewed as cross-coupled pnp and npn bipolar transistors (HBTs), where the base of the pnp is connected to the collector of the npn, and the base of the npn is connected to the collector of the pnp. These are bipolar inversion channel field effect transistors (BICFETs), in which the modulation doped quantum wells perform the function of the base [61]. Due to the p-i-n-i-p-i-n layer structure, there are essentially three junctions formed: 1) a p-i-n emitter junction of the pnp bipolar from the anode to the n-type modulation doped QWs, 2) a n-i-p collector junction from the n-type QWs to the p-type QWs which is the common

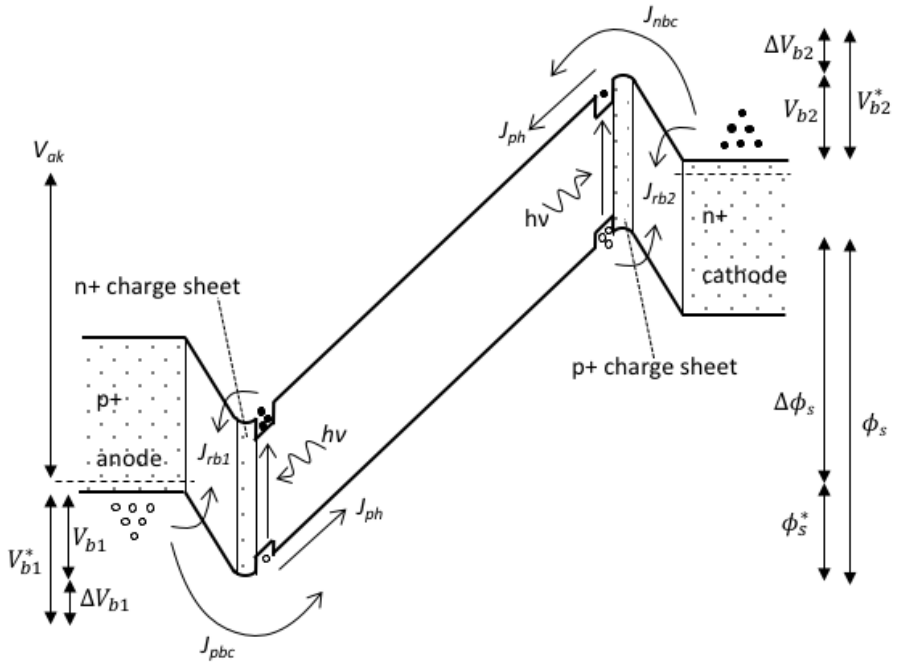

Fig. 5.9 Off-state energy band diagram
Detector energy band diagram in the off-state with a bias V_{ak}. Internal voltages and current components are labeled.

collector for both bipolars, and 3) a p-i-n emitter junction for the npn bipolar, from the p-type QWs to the cathode. The built-in voltage for the top, middle, and bottom junctions are denoted as V_{b1}, ϕ_s, and V_{b2} respectively, with the asterisk defining the values at equilibrium.

Fig. 5.9 shows the energy band diagram when biased in the off-state with a voltage V_{ak}, and under optical illumination. The device is essentially a capacitive divider in the off-state, with capacitances across the barrier regions $C_b = \varepsilon/d_b$ and the d-region $C_d = \varepsilon/d$. Since $d >> d_b$ most of the applied voltage drops across the d-region, as shown in Fig. 5.9 by the large increase in ϕ_s, relative to the small decreases in V_{b1} and V_{b2}.

The voltage drops are related to the applied voltage as

$$V_{ak} = \Delta V_{b1} + \Delta V_{b2} + \Delta\phi_s \tag{5.1}$$

where $V_{b1} = V_{b1}^* - \Delta V_{b1}$, $V_{b2} = V_{b2}^* - \Delta V_{b2}$, and $\phi_s = \phi_s^* + \Delta\phi_s$. The forward bias across the emitter junctions causes a small leakage current to flow through the device, as holes are emitted over the top junction and electrons over the bottom barrier through current components J_{pbc} and J_{nbc}, respectively. These carriers drift in opposite directions across the common-collector region, where they end up in their respective quantum wells. The upper (lower) quantum wells serve as the base of the pnp (npn) bipolar transistors contained in the thyristor, and the carrier concentrations in the wells provide the base currents. With an optical input to the thyristor, photo-generated carriers populate the quantum wells further, and contribute to the base recombination currents J_{rb1} and J_{rb2} by thermionic emission from the wells, to the barrier regions. The total junction currents will consist mostly of holes at the pnp emitter junction and electrons at the npn emitter, since the emitters are doped heavily with respect to the carrier concentrations in the wells, and the fact they are wide bandgap materials. Therefore, a given photocurrent will cause a larger total current to flow through the device, which constitutes the internal current gain inherent to the thyristor photodetector. This gain should also increase with voltage bias as observed experimentally, since the emitter junctions will become more strongly forward biased, driving the BJTs further into the forward-active operating mode.

In Fig. 5.6a, the off-state photoresponse of the detector was seen to be linear, with a slope efficiency η_d. This response, however, is a multiplication of the detector responsivity and the internal current gain. An estimation of responsivity therefore allows these two factors to be decoupled, since η_d has been measured experimentally. Responsivity is given as $R_p = q\eta/h\nu$ where q is the electron charge, η is the quantum

efficiency, and $h\nu$ is the photon energy. The quantum efficiency of a single-pass photodetector is

$$\eta = (1-R)\left[1-e^{-\Gamma\alpha_{qw}L}\right] \tag{5.2}$$

where R is the reflectance of the top air-semiconductor interface, α_{qw} is the absorption coefficient in the active regions, L is the cavity length, and $\Gamma = n_{qw}L_{qw}/L$ is the confinement factor for the active regions. Using R=0.31, α_{qw}=3500 cm^{-1}, α=10 cm^{-1}, L=12,400 Å, and Γ=0.029, the single-pass quantum efficiency is only η=0.00864 due to the thin total active region thickness. Inclusion of the DBR mirrors in the calculation, yields a resonant-cavity enhanced quantum efficiency, since light circulating in the optical cavity makes many passes through the active regions, and the maximum intensity I_{max} in the cavity is larger than that incident I_{inc} on the detector. With R_t as the top mirror reflectance, the quantum efficiency can be expressed as [1], [62]

$$\eta = \frac{(1-R_t)}{(1-r)^2}\left[1-e^{-\Gamma\alpha_{qw}L}\right] \tag{5.3}$$

where r is the round trip field attenuation factor given by $r^2 = \exp(-2\alpha_r L)$and the distributed attenuation coefficient for the cavity is

$$\alpha_r = \alpha + \Gamma\alpha_{qw} + \frac{1}{2L}\ln\left(\frac{1}{R_t R_b}\right). \tag{5.4}$$

For the device presented, the top (bottom) DBR reflectance is calculated to be R_t=0.877 (R_b=0.9988), and (4) gives α_r=646 cm^{-1} and therefore r=0.923. Substituting into (5.3) then gives a quantum efficiency of η=0.26, and the responsivity at 986 nm ($h\upsilon$=1.28 eV) becomes R_p=0.2 A/W. This calculated responsivity value is less than the measured detector slope efficiency η_d presented in section 5.4, and therefore supports the

prediction for internal current gain in the device. Writing the detector slope efficiency as $\eta_d = \beta R_p$ the current gain is then estimated to be β=7.3 and 19.8 at a bias of 3 V and 4 V, respectively.

It should be noted that the current gain calculated above is likely an underestimation due to the following reasons. First, as seen in Fig. 5.2 the current confining SiF implant has a lateral straggle which restricts the current flow to the center of the device, under the optical aperture. Therefore, if the incoming optical beam from the single mode fiber extends into the implanted regions, the generated photocurrent will not contribute efficiently to the intrinsic device current. This is an effective reduction in lateral overlap of the optical intensity within the cavity with the active portions of the QWs. Second, the electric field inside the cavity forms a standing wave pattern, and the above calculation assumes the QWs are located at the maximums of the distribution. Though the cavity was designed so that the QWs are located at maximums of the field intensity in order to maximize absorption, the active regions (including spacers) are 480 Å thick and it is therefore not possible for all the wells to be perfectly aligned to a peak of the field distribution. This would result in a reduction in confinement factor and therefore the calculated quantum efficiency. Lastly, polarization-dependence of the detector response could influence the results, if the angle of incidence of the light is not normal to the surface of the device as intended. This is due to the polarization-dependent absorption coefficient in QWs, when the incident light is not traveling perpendicular to these layers. Though the laser source used in the experiment outputs a linearly polarized beam, polarization maintaining components were not used in the test setup and the polarization state at the detector is

unknown. Coupling light to the detector at normal incidence should mitigate this type of dependence. All of these considerations can negatively impact the quantum efficiency of the detector, and therefore the current gain in the device is likely larger than estimated. Nevertheless, the simplified calculation above establishes baseline values of the current gain and gives insight into the factors influencing the overall off-state thyristor photoresponse.

5.6 Conclusion

A thyristor-based photodector was fabricated and the optoelectronic response characterized experimentally. Owing to the resonant cavity design, a peak detector slope efficiency of η_d=4 A/W was demonstrated at the resonant wavelength, and is greater than 1 A/W over a 5 nm spectral bandwidth, despite the thin active regions. By estimating the device responsivity, a bipolar photocurrent gain of approximately β=20 was obtained at 4 V bias. Operated in the large-signal switching mode, the detector requires P_{in}=20 μW and 60 μW of input power to switch to the on-state, for a bias voltage of 4 V and 3 V respectively. This corresponds to a 1.9 V output voltage when connected to a 1 kΩ load. The device shows promising results in that photocurrent amplification, and large output voltage are obtained simultaneously using a single device, providing the necessary functionality of a photoreceiver circuit.

6 Chapter 6: Thyristor Photodetector Turn-On Analysis

6.1 Introduction

In Chapter 5, a two-terminal thyristor photodetector that operates as an optoelectronic switch was presented. Details of the structure, fabrication, and experimental results are available in [63]. Note that high-speed measurement of the device turn-on was not possible for these devices due to lack of suitable pad layout for RF probing. Future device layouts will be modified to allow high-speed measurements.

In this chapter, the turn-on speed of the detector is analyzed theoretically, in response to a step optical input. This differs from the RC-limited rise time of conventional photodiodes because the thyristor is inherently a nonlinear device. However, in the off-state a linear relationship between the detector current and the optical input power exists, until the current exceeds the switching current, and the detector switches to the on-state. The turn-on time is then limited by the speed at which the device current can be raised above this critical value. The time needed to raise the device current above the critical value can be short because of the internal photocurrent gain and low capacitance. Note that the turn-off time for the detector requires additional device terminals that provide electrical access to charge stored in the device, and has been previously analyzed numerically [56]. Here, an analytical model for the detector is developed in order to derive an expression for the turn-on time, in terms of the device resistances, capacitances, photocurrent gain, and optical input power. Section 6.2 summarizes the device operation in terms of internal device voltages and currents. An equivalent circuit model is developed in section 6.3, that yields the off-state step

response for the detector. In section 6.4 the result is discussed in terms of switching criteria for high-speed performance, and an expression for the turn-on time is given.

6.2 Thyristor Photoreceiver Principles

A photoreceiver circuit based on the thyristor photodetector is shown in Fig. 6.1a, where a load resistor R_L is connected between the cathode and ground, in order to establish the off- and on-state operating points. The current-voltage (I-V) characteristic for the previously described detector [63] under optical illumination is shown in Fig. 6.1b, with the dotted line giving the load line provided by R_L=500 Ω. The circuit has two stable operating points OP_1=(4 V, 15 μA) and OP_2=(2.3 V, 3.3 mA), the intersections of the I-V curve and load line. The load line intersects the I-V curve at a third location between these points, but in this region the device exhibits negative differential resistance and therefore is unstable. The circuit is switched on when the optical input P_{in} is sufficient to increase the thyristor current above the switching current I_{sw}, such that the load line no longer intersects the I-V curve in the high impedance off-state. This initiates regenerative feedback of the internal device

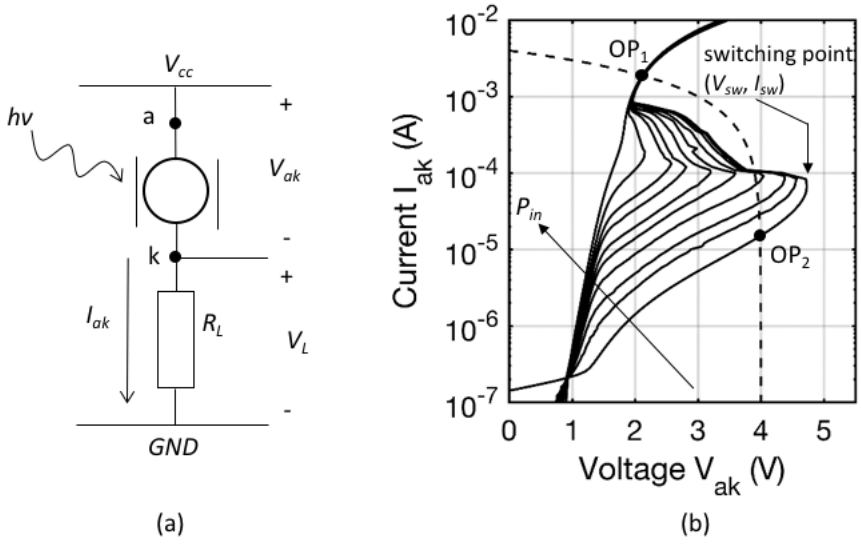

Fig. 6.1 Photoreceiver circuit characteristic
A thyristor photoreceiver circuit (a) incorporating a load resistor. Current-voltage characteristic with optical illumination (b), along with the R_L=200 Ω load line and operating points.

currents, and drives the thyristor into the low impedance mode at the on-state operating point OP_2.

The physical mechanism by which the thyristor photodetector switches in response to optical input is illustrated using the energy band diagram in Fig. 6.2. Here, the device is biased with a voltage V_{ak} in the off-state, with the relevant current components and voltages shown. A detailed theoretical model for the current-voltage characteristics has been presented previously and compared to experiment [57, 58], and the relevant results are presented here. The primary voltages in the device are the barrier region

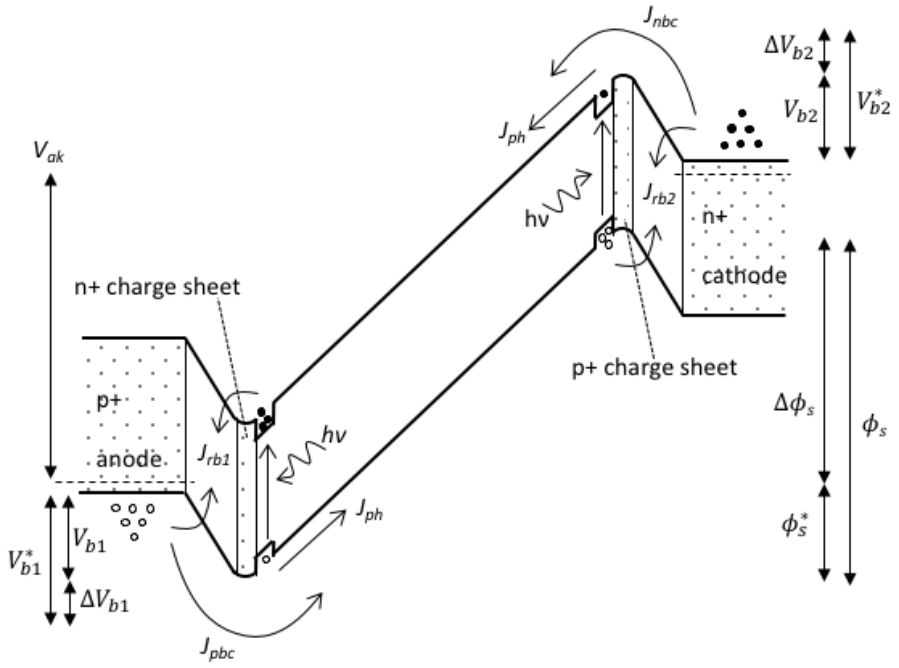

Fig. 6.2 Off-state energy band diagram
Detector energy band diagram in the off-state with a bias V_{ak}. Internal voltages and current components are labeled.

voltages V_{b1} (V_{b2}) and the common-collector region voltage ϕ_s. The overall voltage equation for the device is

$$V_{ak} = \Delta V_{b1} + \Delta V_{b2} + \Delta\phi_s \tag{6.1}$$

where ΔV_{b1}, ΔV_{b2}, and $\Delta\phi_s$ are the voltage drops across the associated regions. In the forward blocking mode, the junction formed across the common-collector region is reverse biased while the two barrier junctions are forward biased, and as a result most of the applied voltage in the off-state is dropped across this region.

The stored charge in device is expressed by a charge equation associated with each modulation doped heterojunction, given by

$$Q_{01} = qL_{z1}n_{01} + C_{b1}\left(V_{b1}^* - \Delta V_{b1}\right) + C_d\left(\phi_s^* + \Delta\phi_s\right) \tag{6.2}$$

and

$$Q_{02} = qL_{z2}p_{02} + C_{b2}\left(V_{b2}^{*} - \Delta V_{b2}\right) + C_{d}\left(\phi_{s}^{*} + \Delta\phi_{s}\right) \tag{6.3}$$

where the voltages denoted with asterisks are equilibrium values, L_{z1} (L_{z2}) are the n-type (p-type) quantum well thicknesses, $C_{b1} = \varepsilon/d_{b1}$ ($C_{b2} = \varepsilon/d_{b2}$) and $C_d = \varepsilon/d$ are the capacitances of the n-side (p-side) barrier and common- collector regions, which are unintentionally doped. Also, $Q_{01} = qd_{01}N_{s01}$ ($Q_{02} = qd_{02}N_{s02}$) is the depletion charge in the modulation-doped charge sheets, and n_{01} (p_{02}) are the electron (hole) densities in the n-type (p-type) quantum wells.

The dominant current components in the device are also shown in Fig. 6.2. As a pnpn type structure, the device may be viewed as cross-coupled bipolar transistors, where the collector of the pnp (npn) transistor is connected to the base of the npn (pnp) transistor. The bipolar devices in the structure are bipolar inversion channel field effect transistors (BICFETs), in which the modulation doped quantum wells perform the function of the base [61]. The p-type emitter (anode) supplies holes to the p-type QW by thermionic emission over the barrier created by the n-type modulation doping. This is the collector current J_{pbc} of the pnp portion of the structure. A similar current flows from the n-type emitter (cathode) over the barrier created by the p-type modulation doping, and supplies the n-type quantum well with electrons. This is the collector current J_{nbc} of the npn BJT portion of the structure. The collector currents are

$$J_{pbc} = J_{pbc0}e^{\Delta V_{b1}/V_T} \tag{6.4}$$

and

$$J_{nbc} = J_{nbc0}e^{\Delta V_{b2}/V_T} \tag{6.5}$$

where the saturation currents J_{pbc0} and J_{nbc0} have been derived previously in detail [57]. Photocurrent generated in the device by optical absorption in the quantum wells also supplies carriers to both wells. The photocurrent density is expressed in terms of quantum efficiency η, photon energy $h\nu$, and the input optical intensity S_{in} as

$$J_{ph} = \frac{q\eta}{h\nu} S_{in} = R_p S_{in} \tag{6.6}$$

where $R_p = q\eta/h\nu$ is the responsivity. The dominant source of carrier loss from the wells is recombination in the barrier regions. Electrons in the n-type quantum well recombine with holes from the anode in the n-side barrier through the recombination current J_{rb1}, while holes in the p-type quantum well recombine with electrons from the cathode through the recombination current J_{rb2}. These currents have also been previously derived and are given as

$$J_{rb1} = J_{rb10} \sqrt{\frac{n_{01}}{n_{01}^*}} e^{\Delta V_{b1}/V_T} \tag{6.7}$$

and

$$J_{rb2} = J_{rb20} \sqrt{\frac{p_{02}}{p_{02}^*}} e^{\Delta V_{b2}/V_T} \tag{6.8}$$

with n_{01}^* (p_{02}^*) being the equilibrium electron (hole) concentrations in the n-type (p-type) quantum wells.

Having defined the important currents, voltages, and charge in the device when operating in the off-state, the thyristor switching process can now be illustrated. Consider the energy band diagram of Fig. 6.2 in the absence of light. The device is in the high impedance mode conducting a small leakage current due to the weak voltage bias across the barrier regions, because as previously noted, most of the applied voltage

drops across the common-collector region, and therefore ΔV_{b1} and ΔV_{b2} are small. When an optical input is supplied, n_{01} increases in response to the photocurrent which promotes recombination through J_{rb1} due to the square root dependence in (6.7), also acting to increase the bias ΔV_{b1} across the barrier. The increased bias in turn increases the collector current J_{pbc} due to the exponential dependence given by (6.4). Next, the increased supply of holes over the n-side barrier leads to an increase of p_{02}, which increases the recombination in the p-side barrier J_{rb2}, and increases the corresponding barrier bias ΔV_{b2}. This, in turn, increases J_{nbc} according to the exponential dependence in (6.5) and electrons are emitted over the p-side barrier where they contribute to an increase in n_{01}. Therefore, not only does the optical input populate the quantum wells, but internal feedback between the device currents will also contribute to the carrier build up. If the optical input is sufficiently high, the feedback will become regenerative and the quantum well carrier concentrations will increase rapidly without bound. According to (6.2), the sum of the charge in the quantum well, barrier region capacitor, and collector region capacitor are equal to that of the charge sheet doping. Therefore if n_{01} increases dramatically, then one of the remaining two terms must decrease. But since ΔV_{b1} simply increases monotonically with total device current [58], it is $\Delta\phi_s$ that must decrease. This corresponds to a collapse of the collector voltage, which allows the barriers to become strongly forward biased, and switch the thyristor from operating point OP_1 to OP_2. Finally, note that n_{01} will not increase indefinitely, but will become stabilized by additional current components that become relevant when operating in the on-state. Also note that this discussion could have started from the point of view of the p-type quantum well, and a similar argument results when p_{02} begins to increase

regeneratively. In actuality, both processes happen simultaneously in response to input light.

If the optical input in the previous discussion was not sufficient to switch the device, a different situation arises. Rather than switching the device to the on-state, the thyristor remains in the off-state conducting a current induced by the incident light. This current is not simply the photocurrent given by (6.6), due to the internal bipolar gain of the thyristor action. This can be seen by noting that the total current flowing in the anode is $J_a = J_{pbc} + J_{rb1}$ and that J_{rb1} is directly modulated by J_{ph} through the dependence on n_{01}. Therefore, a given photocurrent generates a larger current at the device terminals because of internal bipolar amplification, with common-base current gains given by

$$\alpha_1 = \frac{J_{pbc}}{J_{pbc} + J_{rb1}}, \qquad \alpha_2 = \frac{J_{nbc}}{J_{nbc} + J_{rb2}} \tag{6.9}$$

for the pnp and npn BJT portions of the structure, respectively. The current gain provided in the thyristor is an important parameter in determining the performance of the photoreceiver circuit, as it aids in the charge build up in the quantum wells. Ultimately, the time needed to initiate switching to the on-state is determined by the

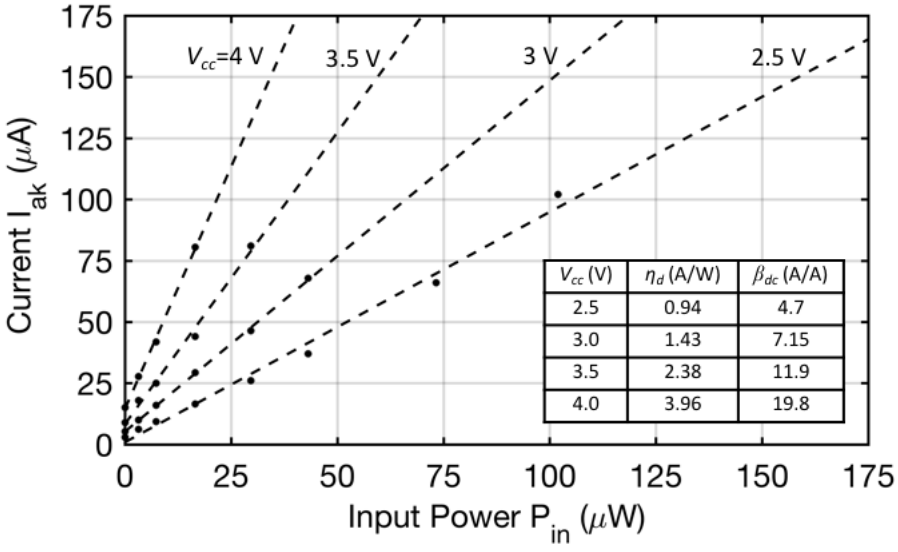

Fig. 6.3 Detector photoresponse
Measured detector current I_{ak} for varying levels of optical input power P_{in}. The current is larger for increased bias V_{cc}, as a result of increased current gain in the device. Detector slope efficiency η_d and the estimated photocurrent gain β_{dc} are tabulated in the inset.

time required to increase the detector current above the switching current and then collapse the common-collector voltage.

In Chapter 5, experimental results for fabricated thyristor detectors showed a linear dependence between the detector current I_{ak} and the optical input power P_{in}. The measured detector current as a function of input power is shown in Fig. 6.3, for different bias voltages V_{cc}. The current is linear with P_{in}, and the detector slope efficiency $\eta_d = \Delta I_{ak}/\Delta P_{in}$ of the response increases with bias voltage. The slope efficiency was determined to be dependent on the dc photocurrent gain $\beta_{dc} = \Delta i_{ak}/\Delta i_p$ and the responsivity $R_p = \Delta i_p/\Delta P_{in}$, such that $\eta_d = \beta_{dc} R_p$. After estimating the responsivity to be R_p=0.2 A/W, the photocurrent gain was obtained after extracting η_d from the measured data. These results are summarized on the inset in Fig. 6.3. In the next section

these observations are used to create an equivalent circuit for the detector, that includes internal gain.

6.3 Turn-On Analysis

The switching process is illustrated in Fig. 6.4, where the thyristor current-voltage characteristic is shown for three values of increasing input power P_{in}, along with a load line. Initially the detector operates at point A in the off-state when the optical input is off or very small. As P_{in} increases the detector current I_{ak} rises as the operating point moves upwards along the load line towards point B. For sufficient P_{in}

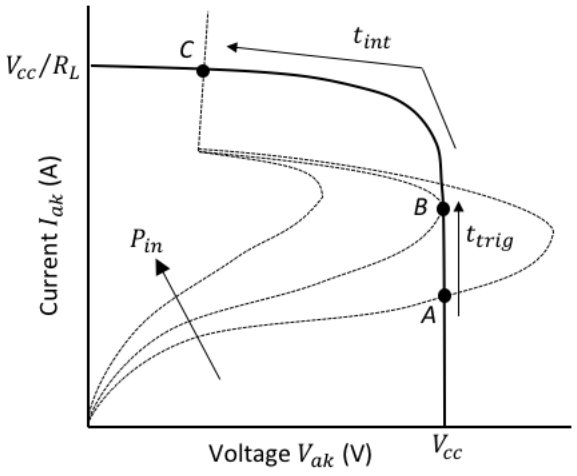

Fig. 6.4 Thyristor switching process
Current-voltage characteristic of the thyristor detector for three, increasing values of P_{in}. The load line is shown by the dark curve and the detector current is depicted on a logarithmic scale.

the detector current will exceed the switching current, and the operating point will move above point B. In this situation the operating point is in the negative resistance region of the device characteristic, which is not a stable operating point, and therefore the detector is triggered to switch to the low impedance on-state, at point C. For high speed operation, the time needed to transition the operating point from point A to point

B is therefore a critical parameter for triggering switching, and will be denoted as t_{trig}. Once triggered, the voltage across the common-collector region ϕ_s collapses while the thyristor turns on, and the operating point moves from point B to point C. The duration of this portion of the turn-on time is dependent on the internal device dynamics as the detector latches on, and is denoted t_{int}. The total turn-on time for the detector then becomes $t_{on} = t_{trig} + t_{int}$. In the following analysis, the turn-on time t_{on} is derived using an equivalent circuit model for the photoreceiver.

The currents shown by Fig. 6.3 correspond to detector current in Fig. 6.4, as the operating point moves along the segment of the load line connecting points A and B. Since the detector is linear in the off-state, a small-signal equivalent circuit can be used to analyze the response using linear system theory. Fig. 6.5 shows the equivalent circuit representation for the photoreceiver, where each of the three junctions in the thyristor is represented by a parallel combination of the respective junction capacitance and resistance. Because the junctions are each formed across unintentionally doped layers d_{b1}, d_{b2}, and d, the capacitances are not voltage-dependent. The nodes in the circuit are labeled with the terminals for the pnp (E_1, B_1, C_1) and the npn (C_2, B_2, E_2), to illustrate that the thyristor is represented by two BICFETs with cross-coupled base-to-collector connections. Also shown are current-dependent current sources which represent the collector currents of the pnp and npn portions of the thyristor, along with the current generator i_p producing the photocurrent.

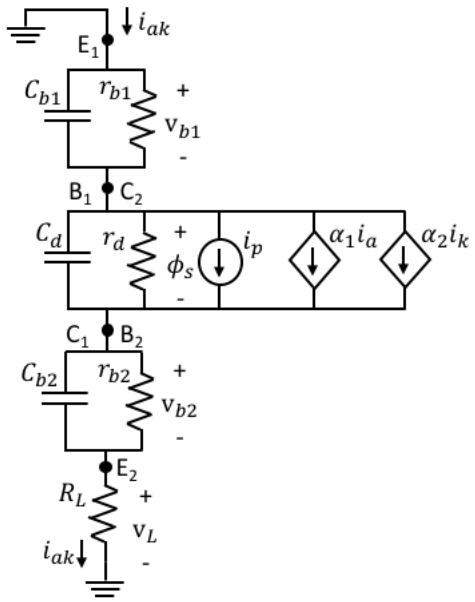

Fig. 6.5 Equivalent circuit model
Small-signal equivalent circuit for the thyristor-based photoreceiver, in the off-state.

Nodal analysis of the circuit gives the transfer function for the small-signal detector current i_{ak} with respect to the small-signal photocurrent i_p as

$$H_\beta(s) = \frac{i_{ak}(s)}{i_p(s)} = \frac{Z_d}{(1-\alpha)Z_d + Z_{b1} + Z_{b2} + R_L} \tag{6.10}$$

where Z_{b1}, Z_{b2}, Z_d, are the parallel combinations of the junction impedance components, e.g., $Z_d = r_d/(1 + sr_dC_d)$, and $\alpha = \alpha_1 + \alpha_2$. Taking $Z_{b1} = Z_{b2} = Z_b$, since d_{b1} and d_{b2} are designed to be equal, and substituting expressions for the junction impedances into (6.10) yields

$$H_\beta(s) = \frac{r_bC_bs + 1}{R_Lr_bC_bC_ds^2 + r_b\left[(1-\alpha)C_b + 2C_d\right]s + (1-\alpha) + 2r_b/r_d} \tag{6.11}$$

where the approximation $r_b, r_d \gg R_L$ has been used. The result is a second-order transfer function which can be written in pole-zero form, by factoring the denominator, to obtain

$$H_\beta(s) = K\frac{(s-z_1)}{(s-p_1)(s-p_2)} \tag{6.12}$$

where the poles are

$$p_1 = -\frac{1}{r_b C_b}\frac{1-\alpha+2r_b/r_d}{1-\alpha+2C_b/C_d} \tag{6.13}$$

and

$$p_2 = -\frac{1}{R_L C_d}(1-\alpha+2C_d/C_b)\ , \tag{6.14}$$

the zero is $z_1 = -1/(r_b C_b)$, and $K = 1/(C_d R_L)$. Using partial fraction expansion, (6.12) can finally be written approximately as the sum of two first-order terms

$$H_\beta(s) = \frac{\beta_{dc}-\beta_{ac}}{1-s/p_1} + \frac{\beta_{ac}}{1-s/p_2} \tag{6.15}$$

where the dc photocurrent gain is $\beta_{dc} = 1/(1-\alpha+2r_b/r_d)$ and the high frequency photocurrent gain is denoted $\beta_{ac} = 1/(1-\alpha+2C_d/C_b)$. Using the derived expression for β_{dc}, the values of α for the detector results shown in Fig. 6.3 can therefore be estimated. Using r_b/r_d=100, then α=0.81, 0.88, 0.94, and 0.97 for V_{cc}=2.5, 3.0, 3.5, and 4 V respectively. Fig. 6.6 shows the magnitude response for varying values of α. For this example and in the remaining calculations, d_{b1}=d_{b2}=300 Å, d=5200 Å, and a D=10 μm diameter device is chosen along with a load R_L=500 Ω. The device capacitances then become C_b=290 fF, C_d=17 fF, and the

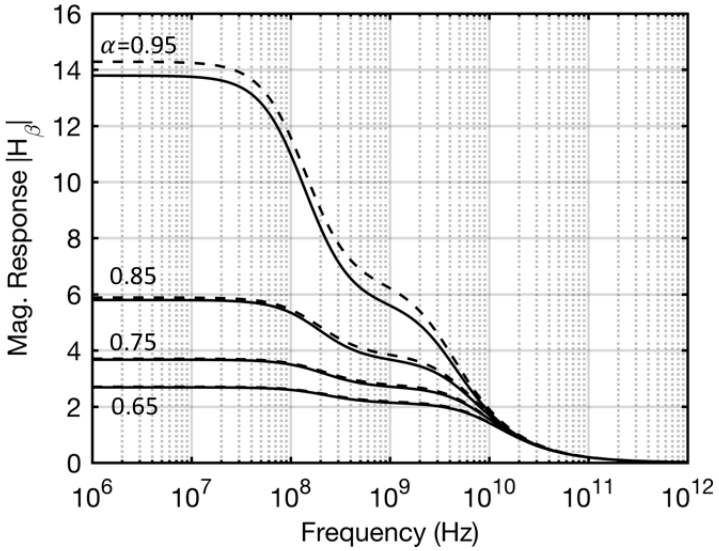

Fig. 6.6 Detector magnitude response
Off-state detector magnitude response for varying values of α. The solid curves show the exact response as given by (6.10) while the dotted curves show the approximate result of (6.15).

high resistivity common-collector junction resistance is estimated from Fig. 6.1b to be r_d≈200 kΩ and r_b≈2 kΩ. The solid curves are calculated from the exact transfer function in (6.10) while the dashed curves are the result of the approximated result in (6.15). Since $r_b C_b \gg R_L C_d$, p_1 is located at a much lower frequency than p_2 and the response is dominated at low frequencies by the first term in (6.15), with a dc value of β_{dc}. At higher frequencies the response becomes dominated by the second term in (6.15), where the response is seen to flatten out to a magnitude approximately equal to β_{ac}, and then rolls off at 20 dB/decade beyond the corner frequency defined by p_2. Overall, the response increases for larger α, increasing β_{dc} more rapidly than β_{ac} since $(C_b/C_d) > (r_b/r_d)$ in this example.

The transient response for the detector current i_{ak} in response to a step input of photocurrent i_{p0} is found by calculating the inverse Laplace transform $\mathcal{L}^{-1}\{s^{-1}H_\beta(s)i_{p0}\}$, where $H_\beta(s)$ is given by (6.15). The resulting step response is

$$i_{ak}(t) = [\beta_{dc} - \beta_{ac}]\left(1 - e^{-\frac{t}{\tau_b}}\right) i_{p0} + \beta_{ac}\left(1 - e^{-\frac{t}{\tau_d}}\right) i_{p0} + I_0 \qquad (6.16)$$

where the time constants are $\tau_b = -1/p_1$ and $\tau_d = -1/p_2$, and the dark current flowing in the detector at time t=0 is I_0. Substitution of the circuit values along with α=0.9, gives the time constants as τ_b=1040 ps and τ_d=39 ps, and therefore the two terms in (6.16) will contribute to the step response at drastically different time scales. Initially, the second term dominates and the current will rise to a value of $i_1 = \beta_{ac} i_{p0}$ in a time $t \approx 4\tau_d$. Next, the second term stops increasing and the current rises, relatively slowly, to a final value of $i_2 = \beta_{dc} i_{p0}$ at time $t \approx 4\tau_b$. As discussed in the following section, dependent on the detector parameters and the level of the input photocurrent, the detector may be triggered slowly, quickly, or not at all.

During the second portion of the turn-on process, the common-collector voltage ϕ_s collapses rapidly as the detector operating point transitions from B to C in Fig. 6.4, and the current rises to the on-state value. Since the device is under regenerative feedback as it latches on, the transition time is independent of input photocurrent. The time t_{int} to complete this process is limited by the carrier transit time across the common-collector of thickness d, as well as the discharge time of the internal capacitance $C_d = \varepsilon/d$. After switching is triggered the differential resistance of the detector falls to the on-state value, which for the example device in Fig. 6.1b is r_{on}=185 Ω, and the impedance presented to C_d becomes $(r_{on} \parallel R_L)$. Using R_L=500 Ω and C_d=17 fF, the *RC*-limited 90% to 10% discharge time is therefore $t_{RC} = 2.2(r_{on} \parallel R_L)C_d = 5$ ps. The transit time for a device with d=5,200 Å and an average drift velocity

v_{drift}=1.5·10^7 cm/s is t_{drift}=3.5 ps. Since the contributions are comparable, the total internal switching time depends on both limiting factors and can be written as

$$t_{\text{int}} = \sqrt{t_{RC}^2 + t_{drift}^2} \tag{6.17}$$

and for the example values used above becomes t_{int}=6.1 ps. This result is consistent with numerically simulated results that reported t_{int}=5 ps [56]. Because t_{int} depends only on structural parameters that determine the internal capacitance and dynamic resistances, it cannot be reduced by increasing the input photocurrent, and becomes the ultimate limit for the speed of the detector turn-on time t_{on}. This ultimate limit is impacted by device design and the degree to which ballistic transport becomes important in a scaled device. By decreasing the distance d and increasing the launching electric field at each heterojunction, ballistic velocities greater than 2·10^7 cm/s may be realized. The fastest turn-on time is therefore obtained by minimizing t_{trig}, which as discussed in the following section, requires a certain level of input photocurrent and internal thyristor photocurrent gain.

6.4 Discussion

The triggering time for the detector is given by the time needed for the detector step response in (6.16) to exceed the switching current. Depending on the

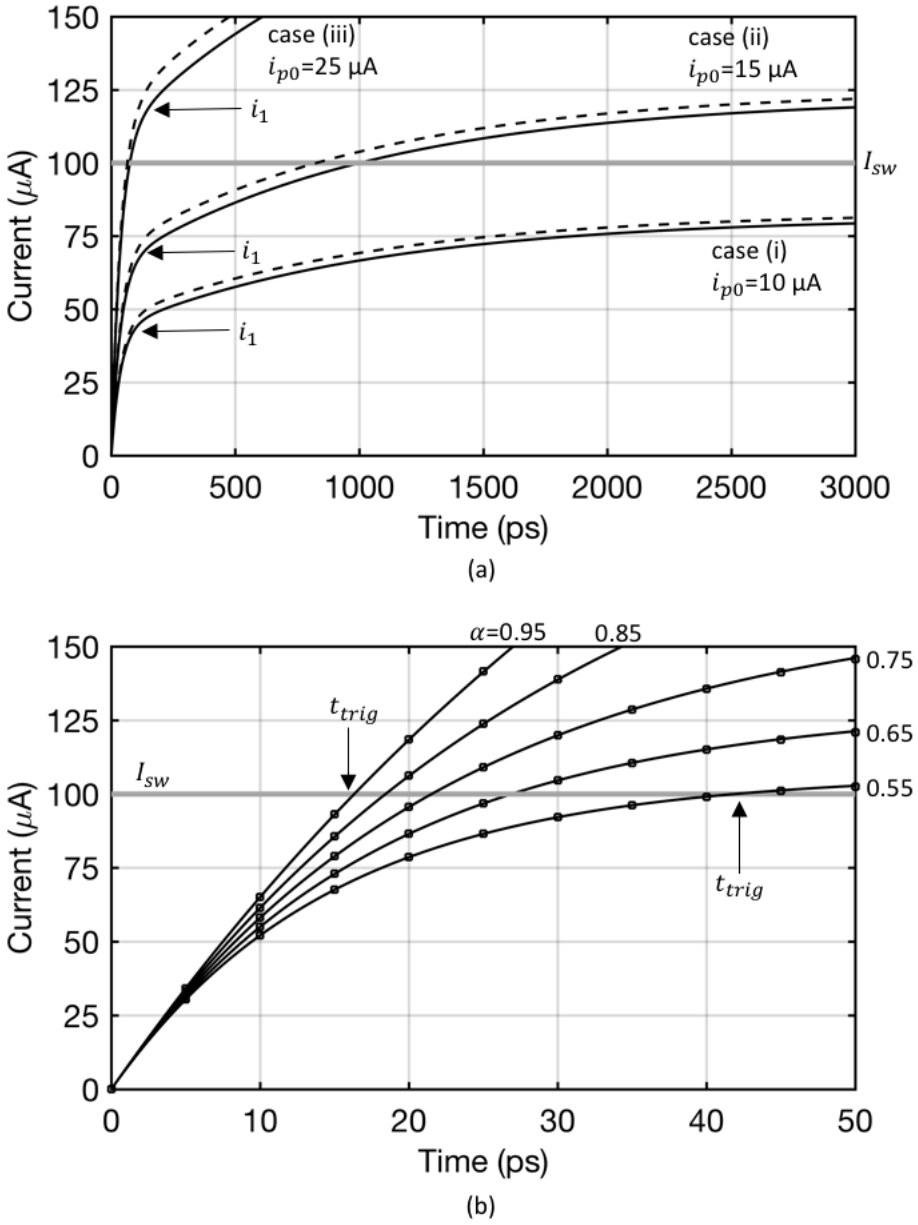

Fig. 6.7 Detector step response
Off-state detector step response for different values of photocurrent step amplitude i_{p0} (a). The three operating mode cases are shown where (i) the detector does not trigger, and (ii) the detector is triggered slowly, and (iii) the detector is triggered quickly. Step response on a shorter time scale (b) with varying values of α. The trigger time is reduced for increasing α.

amplitude of the photocurrent input, and the detector parameters three situations arise: (i) the detector does not trigger, (ii) the detector trigger time is long, and (iii) the detector trigger time is short. These three cases are illustrated by varying i_{p0} in Fig.

6.7a with α=0.9, I_{sw}=100 μA, and circuit values given previously. Case (i) occurs for i_{p0}=10 μA yielding $i_1 < I_{sw}$ and $i_2 < I_{sw}$, such that the final value of the step response does not exceed the switching current. Here, the step response never intersects I_{sw} because i_1=46 μA and i_2=83 μA, and the detector does not trigger. Increasing the photocurrent to i_{p0}=15 μA produces the case (ii), where $i_1 < I_{sw}$ and $i_2 > I_{sw}$. Since i_2=125 μA the detector does trigger, but at a relatively long time of t_{trig}≈1 ns, since the rise in current is governed by the long time constant τ_b when i_{ak} finally intersects I_{sw}. The solid curves in Fig. 6.7a have been obtained from a numerical calculation for the step response of (6.10), while the dotted curves result from the approximate form in (6.16). Case (iii) occurs when i_{p0}=25 μA, because $i_1 > I_{sw}$. In this situation triggering occurs while the step response is rising quickly, due to the small time constant τ_d in the second term of (6.16). The resulting trigger time is t_{trig}=75 ps, substantially faster than the triggering time obtained when i_{p0}=15 μA. For operation as a high speed photoreceiver, this is therefore the desired mode of operation. Fig. 6.7b shows the step response on a shorter time scale for different values of α and i_{p0}=60 μA. Holding the photocurrent constant and increasing α decreases the trigger time. As α is increased from α=0.55 to α=0.95, the speed of the response increases, and t_{trig} is reduced from t_{trig}=42 ps, to t_{trig}=16 ps. These considerations show that both input photocurrent and internal current gain are important for high speed turn-on.

The square markers in Fig. 6.7b are computed using only the second term in (6.16), while the solid curves are computed numerically from the exact transfer

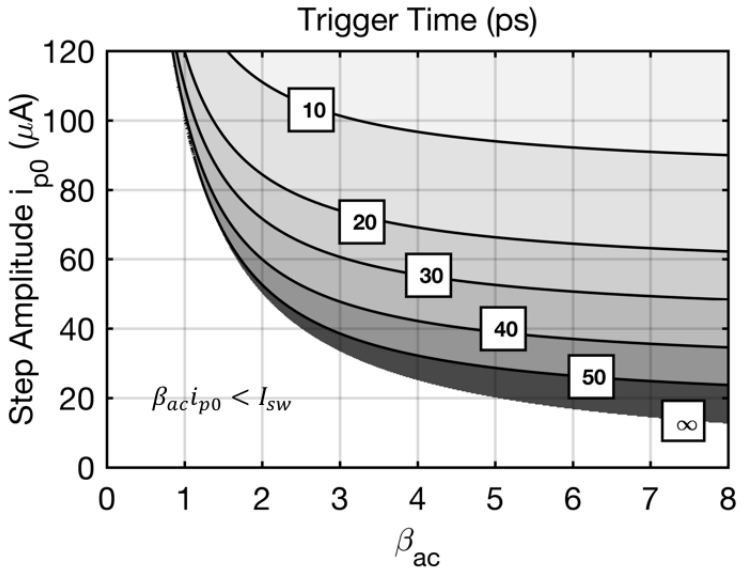

Fig. 6.8 Trigger time contours
Trigger time t_{trig} contours as a function of step amplitude i_{p0} and high frequency current gain β_{ac}. The unshaded region corresponds to the situation where $\beta_{ac} i_{p0} < I_{sw}$, where the case (iii) solution for t_{trig} does not exist.

function in (6.10), and the results are indistinguishable for the initial transient that is governed by τ_d. An expression for the trigger time is obtained by setting the second term in (6.16) equal to I_{sw} and solving for $t = t_{trig}$ to give

$$t_{trig} = \tau_d \ln\left[\frac{1}{1-\left(\frac{I_{sw}-I_0}{\beta_{ac} i_{p0}}\right)}\right] \tag{6.18}$$

The result shows that the trigger time is proportional to $R_L C_d$, and therefore may be reduced by device scaling. Also, for a given I_{sw}, increasing i_{p0} will also reduce t_{trig}, so it is important to maximize optical coupling into the detector and to maximize the responsivity since $i_{p0} = R_p P_{in}$. Lastly, α should be large enough to obtain sufficiently high frequency photocurrent gain β_{ac}. Fig. 6.8 shows t_{trig} contours as a function of i_{p0} and β_{ac} as given by (6.18). The unshaded region corresponds to $\beta_{ac} i_{p0} < I_{sw}$ and

therefore the case (iii) solution for t_{trig} does not exist. Increasing the high frequency photocurrent gain beyond β_{ac}≈4 yields little reduction of t_{trig} at a given photocurrent step amplitude. Increasing the step amplitude, with β_{ac}=4, decreases t_{trig} dramatically over i_{p0}=30 μA to i_{p0}=60 μA, with a lesser impact for further increase. Finally, the total turn-on time for the thyristor-based photoreceiver becomes $t_{on} = t_{trig} + t_{on}$, and is obtained using (6.17) and (6.18).

6.5 Conclusion

The turn-on time for a thyristor-based photoreceiver has been derived by analyzing an equivalent circuit model for the detector, in the off-state. It is determined that for high speed operation, the condition $i_1 > I_{sw}$ should be satisfied, such that the device triggers on a time scale controlled by the short time constant τ_d. The result reveals that the turn-on time depends not only on the $R_L C_d$ time constant, but also the value of the photocurrent gain, which has been derived in terms of the individual bipolar emitter-collector gains. For typical device parameters d_{b1}=d_{b2}=300 Å, d=5200 Å, D=10 μm, R_L=500 Ω, β_{ac}=5, and i_{p0}≥60 μA the analysis yields turn-on times less than 25 ps, which is suitable for application in high-speed, short reach optical links. Furthermore, a noise analysis of the off-state detector is possible by using the presented equivalent circuit model, as it allows the equivalent noise bandwidths to be evaluated. The impact of noise will yield a t_{trig} that is itself a random variable, which can influence the receiver bit error rate and define appropriate incident power levels. This analysis will be pursued in a future work.

7 Chapter 7: Conclusions

This dissertation has investigated resonant-cavity devices for application in high-speed optical interconnects. The performance improvements that arise from resonance-enhanced sensitivity were established through a combination of theoretical analysis, simulation, and experiment.

An optical switching fabric based on the second-order microring topology was designed and simulated. Through careful selection of the coupling coefficients in the switch, a 4x4 prototype fabric was proposed. Simulated results show that 40 Gbps digital signals and mm-wave optical signals can traverse the fabric, maintaining good signal integrity at the output ports.

A theoretical model for microring modulation was presented, in which optically-limited bandwidth is quantified. The small-signal approach allowed for both index-modulated and coupling-modulated devices to be analyzed, with resulting frequency responses that agree well with experimental data from the literature. Extension of the analysis to include electrode capacitance allowed the dynamic power dissipation to be predicted accurately.

A novel GaAs based thyristor photodetector design was presented, and characterized experimentally. Due to the bistable switching behavior, output voltages compatible with CMOS logic circuits were obtained without the use of amplification. Despite the thin active regions in the devices, incorporation of the resonant cavity to enhance the absorption along with the internal current gain produced a detector with slope efficiency of 4 A/W, across a 5 nm spectral width at 980 nm.

The turn-on speed of the photodetector was quantified analytically, based on the experimental results. Linearity of the off-state photoresponse allowed an equivalent circuit model for the detector that includes photocurrent gain. Analysis of the circuit demonstrated the importance of current gain for achieving fast rise times. Using parameters obtained for the experimentally demonstrated device, the rise times less than 25 ps were predicted.

The author expects that research activity in this field will continue to be pursued, as the data center demand for low-power, high-bandwidth interconnects grows.

A Appendix A: Performance of Subsampled Analog Optical Links

A.1 Introduction

Analog optical links offer a variety of performance advantages for handling microwave signals due to the wide bandwidth of optoelectronic devices and low attenuation of optical fiber. Additionally, the link may be designed to perform RF signal processing functions such as filtering, multiplexing, and frequency conversion, all with the added capability of low-loss signal transport over many kilometers. Due to these benefits, microwave photonic links have been studied for applications such as communications, radar, phased antenna arrays, electronic warfare, and analog-to-digital conversion [64-73].

Frequency conversion in optical links has been demonstrated with high dynamic range, low conversion loss, and moderate noise figures [66, 67]. These link configurations are generally similar in that the RF/IF signal is applied to a modulator that is fed with an optical local oscillator (LO). The optical LO may be derived by heterodyning two laser modes, modulating a CW laser with an electrical LO, or by using a pulsed optical source such as a mode-locked laser (MLL) [68-71]. This last approach has gained interest in recent years due to the development of MLLs with GHz repetition rates, picosecond pulse widths, and femtosecond timing jitter. These properties yield narrow-linewidth frequency combs that can provide very stable frequency conversion at multiples of the MLL fundamental frequency. In the time-domain, the optical pulse-train samples the RF signal as it passes through the

modulator. Using subsampling techniques, bandlimited RF signals may be translated near baseband, i.e. frequency conversion. Also referred to as undersampling, bandpass sampling, or downsampling, the technique involves sampling a bandpass signal at rate less than the maximum frequency content. This intentionally introduces aliasing so that a baseband signal replica may be reconstructed. Note that the sampling frequency must still satisfy the Nyquist sampling theorem, such that the modulation bandwidth, i.e. instantaneous bandwidth, of the RF signal must be less than half the sample rate. Also note that subsampling is distinct from equivalent-time sampling which is used in many sampling oscilloscopes. There, periodic waveforms are sampled over many signal cycles to generate the sampled waveform, while subsampling operates in real time on arbitrary, band-limited RF signals. The optoelectronic sampler has many performance advantages over purely electronic sampling circuits. First, the sampling errors originating from timing instabilities of the sampling signal are superior due to the fact that MLL timing jitter can be orders of magnitude smaller than state-of-the-art electronic clocks. Second, the emergence of high-speed optical modulators enables RF signals with very high carrier frequencies to be subsampled. For example, electrooptic modulation has been demonstrated above 100GHz, well beyond the capabilities of electronic samplers [74]. These properties have led to development of photonic ADC architectures which leverage these advantages [71, 72, 75].

This paper provides expressions for the link gain, spurious-free dynamic range, and noise figure in an attempt to recognize fundamental capabilities and limitations of subsampled optical links. In addition, design considerations are presented, such as sampling frequency selection, device limitations, and pulse width implications. It is

acknowledged that the gain of subsampled links has been derived elsewhere and that optical pulse width limitations have been discussed qualitatively [76]. In this work, the impact of timing jitter in the pulsed laser source is included, since it influences the noise figure and the spurious-free dynamic range. Timing jitter is especially important in subsampled links due to the large errors that occur when sampling high frequency RF signals. Also, the pulse width effects have been quantified and the conditions for distortion-free subsampling are provided. Finally, the link is discussed in terms of effective number of bits (ENOB) so that it may be assessed as a front end for photonic ADC systems. The link conversion gain is also derived here, for the sake of completeness.

This chapter is organized as follows: Section A.2 outlines the link architecture, the sampling rate criteria, and provides a derivation of the subsampled link conversion gain. Comparison to other downconverting links is also provided. Section A.3 presents the noise properties of the link, including timing jitter on the sampling pulse-train, and section A.4 presents the spurious-free dynamic range. Comments on ADC application are at the end of this section.

A.2 Conversion Gain

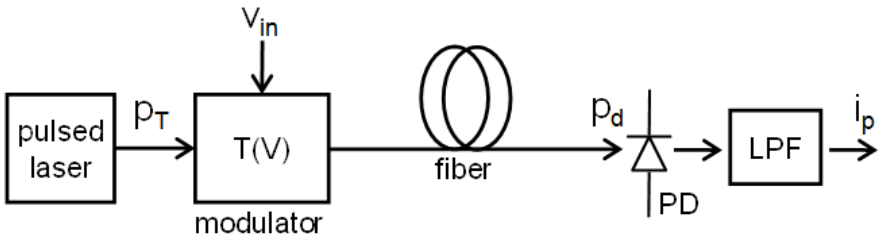

Fig. A.1 Sampled analog optical link architecture
Generic photonic sampling link consisting of a pulsed laser source, an optical modulator with transmission T(V), a length of optical fiber, a photodiode (PD) and a lowpass filter (LPF).

A generic photonic sampling link that uses intensity modulation and direct detection (IM-DD) is shown in Fig. A.1. The output of a pulsed optical source is passed through an optical intensity modulator, which is fed with the input RF signal $v_{in}(t)$. This impresses the input signal onto the pulses, effectively sampling the input voltage. The pulses then travel through a length of fiber to a photoreceiver, which converts the optical samples into electrons and provides lowpass filtering to eliminate unwanted spectral content produced by the sampling process. At the input of the modulator the optical pulse train may be written as

$$p_T(t) = P_p \sum_{n=-\infty}^{\infty} p(t - nT_r) = P_p \sum_{n=-\infty}^{\infty} c_n e^{jn2\pi f_r t} \qquad \text{(A.1)}$$

where $p(t)$ is the individual pulse shape which is normalized to a peak value of unity, P_p is the peak pulse power, and T_r is the pulse repetition time between successive pulses. The rightmost result is the Fourier series of the pulse train with coefficients c_n and fundamental frequency $f_r = 1/T_r$. The coefficients are related to the Fourier

transform of the pulse shape $P(f)$, and are given as $c_n = P(nf_r)/T_r$. To keep the analysis general, the modulator optical transmission is defined as

$$T\left(\mathrm{v}_{in}\right) = a_0 + a_1\mathrm{v}_{in} + a_2\mathrm{v}_{in}^2 + a_3\mathrm{v}_{in}^3 + \ldots \tag{A.2}$$

which is a Taylor series expansion of $T(V)$ about the bias voltage. The higher ordered terms of (2) give rise to distortion that impacts the dynamic range of the link. Under desired operation, however, the modulation depth is small and to first-order these terms may be neglected. A quadrature-biased Mach-Zehnder modulator (MZM) is commonly used, such that $V_{bias} = V_\pi/2$ where V_π is the switching voltage. In this case $a_0 = 1/2$ and $a_1 = -\pi/(2V_\pi)$ [73]. Under the small modulation depth simplification, the optical power incident on the photoreceiver is

$$\begin{aligned} &p_d\left(t\right) = t_0 p_T\left(t\right) T\left(\mathrm{v}_{in}\right) \approx \\ &t_0 a_0 P_p \sum_{n=-\infty}^{\infty} c_n e^{jn2\pi f_r t} + t_0 a_1 \mathrm{v}_{in}\left(t\right) P_p \sum_{n=-\infty}^{\infty} c_n e^{jn2\pi f_r t} \end{aligned} \tag{A.3}$$

which consists of two terms; the original pulse train scaled by the DC modulator transmission a_0 and the product of the input signal and pulse train scaled by the linear modulation coefficient a_1. The factor t_0 is included to account for any optical losses between the laser and detector. Taking the Fourier transform of (A.3), to reveal the frequency-domain effects of the sampling process, yields

$$P_d\left(f\right) = t_0 a_0 P_p \sum_{n=-\infty}^{\infty} c_n \delta\left(f - nf_r\right) + t_0 a_1 P_p \sum_{n=-\infty}^{\infty} c_n V_{in}\left(f - nf_r\right) \tag{A.4}$$

where the frequency shifting property of the Fourier transform has been used. This outcome shows the well-known result of sampling in that the signal spectrum has been replicated at integer multiples of the pulse repetition rate. This is illustrated in Fig. A.2

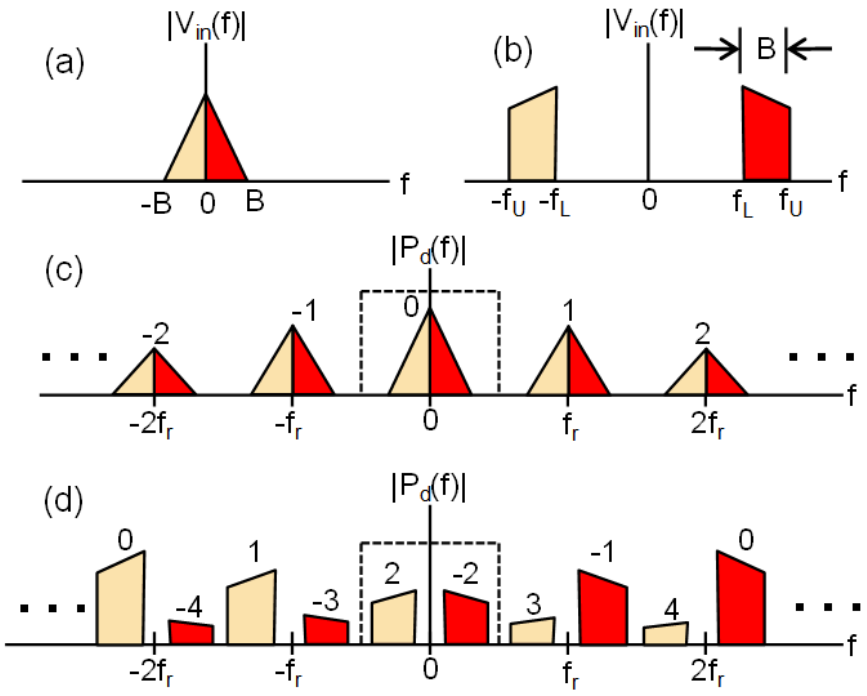

Fig. A.2 Signal spectrums in the sampled link
Input baseband (a) and bandpass (b) signal spectrums. Spectrums of the optical signal at the photoreceiver input for baseband (c) and bandpass (d) sampling. The numbers above the spectrum replicas correspond to the value of *n* in (A.4) and the photoreceiver frequency response is shown by the dotted rectangle. The *n*=0 spectrums correspond to the un-shifted replicas.

for both baseband (a) and bandpass (b) type input signals. For the bandpass case where down-conversion is desired, Fig. A.2d shows that signal replicas appear near baseband and the down-converted signal is then reconstructed by the lowpass response of the photoreceiver. In the baseband case shown in Fig. A.2c the photoreceiver response simply reconstructs the original baseband signal without any frequency translation. If instead the receiver were designed to have a bandpass response, it would be possible to reconstruct an up-converted version of the baseband signal, though this will not be pursued further in this paper. Also present in (A.4) is a scaled version of the pulse train spectrum which is not typical of the sampling process but results here due to the DC

term of the modulator transmission. This term has been neglected in Fig. A.2c-d for clarity.

In order for the sampled signal to accurately represent the original continuous-time signal, the replicated spectrums in (A.4) must not overlap or distortion due to aliasing will result. The sampling theorem provides the necessary criteria as $f_s > 2B$ where B is the modulation bandwidth of the RF input signal. This criteria is valid for both baseband sampling where the maximum signal frequency is equal to B, and for bandpass sampling where the maximum signal frequency can be much larger than B. The question of sampling frequency choice for bandpass sampling then remains, since there can be many rates that satisfy $f_s > 2B$ and do not introduce aliasing errors. The criteria which guarantees error-free bandpass sampling is given as [77]

$$\frac{2f_U}{N} \le f_s \le \frac{2f_L}{N-1} \tag{A.5}$$

and

$$1 \le N \le \left\lfloor \frac{f_U}{B} \right\rfloor \tag{A.6}$$

where f_L and f_U are lower- and upper-frequency bounds of the signal, N is an integer, and $\lfloor x \rfloor$ is the floor function which returns the largest integer smaller than x. Note that an anti-alias filter is generally required to band-limit the input signal. For the interested reader, practical bandpass sampling considerations such as the tolerance to sampling frequency error and guard-band allocation are also discussed in [77].

The conversion gain of the sampled link can be derived by assuming a sinusoidal input voltage $\mathrm{v}_{in}(t) = V_0 \cos 2\pi f_{RF} t$ that lies on some frequency interval

$[f_L, f_U]$. If the photoreceiver has a responsivity η and an ideal lowpass response with cutoff $f_s/2$ then substituting $\mathrm{v}_{in}(t)$ into (A.3) gives

$$i_p(t) = I_{avg}\left[1+\frac{a_1|c_M|}{t_0 a_0 c_0}V_0\cos\left(2\pi f_{IF}t+\angle c_M\right)\right] \tag{A.7}$$

where $I_{avg} = \eta P_p a_0 c_0 t_0$ is the DC photocurrent and the intermediate frequency is $f_{IF} = |f_{RF} - Mf_s|$ with $M = (N-1)/2$ for odd N and $M = N/2$ for even N. The conversion gain of the link is then found to be

$$\begin{aligned} G_c &= \frac{P_{IF}}{P_{RF}} = \frac{\left\langle i_p^2\right\rangle R_d}{\left\langle \mathrm{v}_{in}^2\right\rangle / R_m} = \left(\frac{I_{avg}|a_1||c_M|}{a_0 c_0}\right)^2 R_m R_d \\ &\overset{MZM}{=} \left(\frac{\pi I_{avg}}{V_\pi}\chi_M\right)^2 R_m R_d \end{aligned} \tag{A.8}$$

with R_m being the resistance of the modulator electrodes and R_d being the load resistance of the photoreceiver. Note that an equivalent result is derived and verified experimentally in [76], where the frequency response of the modulator and photodetector has been included. The gain depends on the average photocurrent, the linear modulation coefficient, and the ratio of $|c_M|$ to c_0 which will be referred to as χ_M so that $\chi_M = |c_M|/c_0$. Equation (A.8) is a general result that can be applied to any analog optical link where the optical source is either periodic or CW. For instance, when the optical source is a CW laser there is no frequency conversion, so M=0, c_0=1, χ_M=1, and then (A.8) reduces to the gain expression for CW links i.e. $G_{CW} = \left(\pi I_{avg}/V_\pi\right)^2 R_m R_d$ [78]. In the case of the series modulator configuration, where the

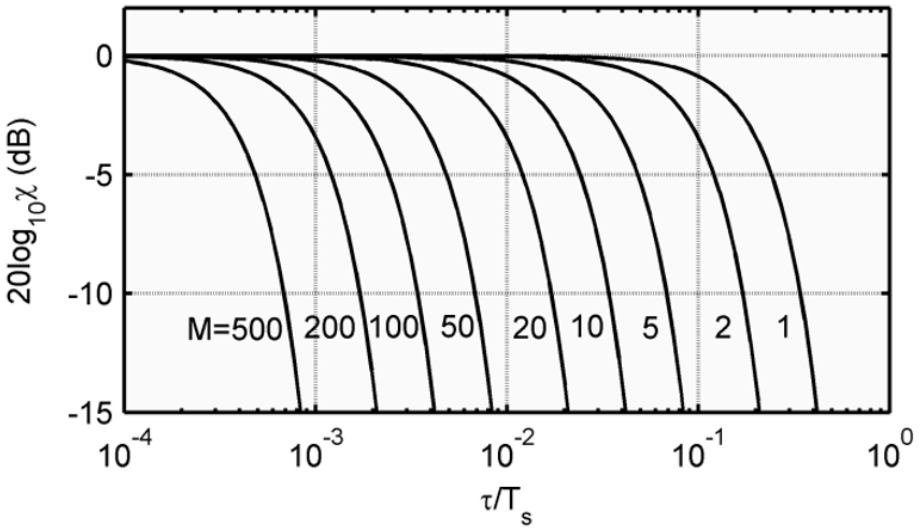

Fig. A.3 Pulse width consideration
Ratio $\chi_M = |c_M|/c_0$ versus duty cycle for a Gaussian pulse train. Here, *M* denotes the *M*-th harmonic of the optical pulse train. For larger choices of *M* in the subsampled link, the duty cycle must be reduced to maintain a given conversion gain.

electrical LO and RF signal are applied to the first and second modulators respectively, $|c_M| = J_M/2$ where J_M is the maximum value of the M^{th}-order Bessel function and c_0=1/2. In this case (A.8) reduces to the conversion gain of the link which is given as $G_{series} = \left(\pi I_{avg} J_M/V_\pi\right)^2 R_m R_d$ [66]. The value of χ_M depends on the duty cycle of the optical pulse-train. A Gaussian pulse-train, for example, has Fourier series coefficients $c_M = \sqrt{\pi}(\tau/T_s)\exp[-(\pi M\tau/T_s)^2]$ and therefore when $(\tau/T_s) \ll 1/M$ the exponential tends to unity so that $c_0 \approx c_M$ and $\chi_M \approx 1$. The result is that the conversion gain of an undersampled link given in (A.8) reduces to the CW link-gain-relation, provided that the duty cycle is sufficiently small. Fig. A.3 shows the ratio $\chi_M = |c_M|/c_0$ versus duty cycle for a Gaussian pulse-train. For a given average photocurrent it can be shown that $(\tau/T_s) \leq (0.187/M)$ is required for the gain given in (A.8) to be within 3 dB of the CW link-gain for which χ_M=1. Note that the subsampled link is more efficient than the

series modulator configuration in terms of average laser power. Because of the 3 dB optical loss incurred by the extra quadrature-biased modulator in the link, twice as much laser power is required to obtain a given DC photocurrent. Furthermore, if the pulse-train duty cycle is sufficiently small, the series modulator conversion gain is reduced by a factor J_M^2 compared to the undersampled link.

The conversion gain model presented is based on an optical power model rather than optical field. It is useful for revealing fundamental characteristics of subsampled links, but is limited in that the influence of chromatic dispersion can not be evaluated. In addition, the optical power model will not describe links that employ optical filtering, since optical filters rely on interference and must be analyzed using optical fields. Chromatic dispersion in analog optical links, with conventional double side band modulation (DSB), causes a power reduction in the link output due to the fact that the optical sidebands travel through fiber at different velocities. When the two sidebands have a π-phase difference at the detector, then the respective beat notes with the optical carrier cancel each other perfectly, resulting in no output RF power. This limits the distance that analog optical signals may be transmitted. Although not analyzed in this work, the various methods used to mitigate the power penalty caused by dispersion in CW links may also be applied to subsampled links. For example, single sideband modulation (SSB) using dual-drive MZMs has been shown to mitigate the effects of chromatic dispersion [79].

A.3 Noise Figure

At the output of the link, the smallest detectable signal is determined by the noise level, while the maximum allowed signal power is limited by compression and

distortion. The total output noise includes thermal contributions from the input and output of the link, shot noise arising from the photodetection process, laser relative intensity noise, optical amplifier excess noise, and jitter noise due to timing fluctuations of the pulsed optical source. At the output of the link, the noise density can be written in terms of a penalty above the shot noise limit as [80]

$$N_0 = \left(2G_c + 1\right) N_{th} + \left(1 + \mathrm{np}\right) N_{sn} + N_j \tag{A.9}$$

where $N_{th} = kT$ with k being Boltzmann's constant and T=290°K, $N_{sn} = 2qI_{avg}R_d$ is the shot noise power spectral density (W/Hz) with q being the electron charge, and np is the noise penalty of the link which is not less than zero. Writing the output noise in this form allows for easy comparison to shot noise limited links which sets the fundamental limit on performance. The last term in (A.9), found only in sampled and frequency-converting links, arises from timing instabilities in either the optical pulse-train or local oscillator as a result of phase noise or timing jitter. In sampled links, timing jitter on the optical pulse-train results in sampling errors, since a given optical pulse does not sample the input signal at the ideal position in time. Fig. A.4 illustrates the effect that variations in the sampling instant have on the sample amplitudes when the input to the modulator is a pure sinusoid. The sampling error ΔV for a particular sample is a function of the timing error ΔT and slew rate of the signal at the sampling instant. Therefore, the

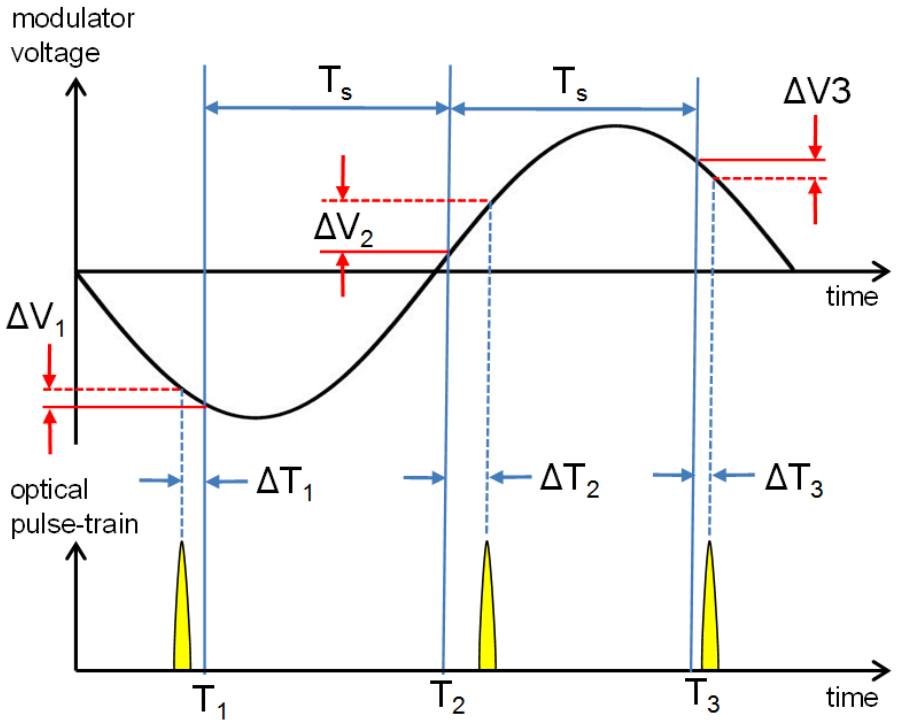

Fig. A.4 Timing jitter diagram
Effect of timing jitter during optical sampling. Each pulse deviates from the ideal position by a time ΔT. This causes a sampling voltage error $\Delta V(t) = [dV(t)/dt]\Delta T(t)$ at the sampling instants. These errors appear as noise contributions in the link output.

largest error is produced in Fig. A.4 is at T_2 since the slope of the signal is largest at that sampling time. When the timing fluctuations are much smaller than the period of the pulse-train, then the error voltage for sampling a sine wave at time t is $\Delta V(t) = [dV(t)/dt]\Delta T(t)$. For $V(t) = V_0 \cos(\omega_{RF} t)$ the mean-square value of the sampling error is [81]

$$V_{err}^2 = \frac{V_0^2 \omega_{RF}^2 \sigma_T^2}{2} \tag{A.10}$$

where σ_T is the rms jitter of the pulse-train and ω_{RF} is the RF carrier frequency. This result shows that the voltage error is proportional to the sine wave amplitude and frequency, as well as the rms timing jitter. For subsampling microwave signals, the

maximum frequency content of the signal is much larger than the bandwidth of the signal. Therefore, the jitter requirements of the sampler are much more stringent compared to baseband sampling. Since this noise source enters the link at the modulator, the contribution to the output noise power density (W/Hz)

$$N_j = G_c \frac{V_{err}^2}{R_m} \frac{2}{f_s} = P_{in} G_c \omega_{RF}^2 \sigma_T^2 \frac{2}{f_s} \tag{A.11}$$

is found by multiplying (A.10) by the conversion gain given in (A.8) and it has been assumed that the noise power due to sampling error is spread evenly across the first Nyquist zone ($0 \leq f \leq f_s/2$).

The noise figure (NF) of the link may be written using (A.9) as

$$NF = \frac{N_{out}}{kTG_c} = \frac{\left(2G_c + 1\right) + \left(1 + \mathrm{np}\right) N_{sn} + N_j}{kTG_c} \tag{A.12}$$

and it is noted that because the jitter noise contribution is dependent on the link input RF power, the noise figure also has this dependency. The question then arises as to what value of input power should be used in calculating the noise figure. An appropriate choice is the maximum spurious-free input power P_{msf} which is defined as the input power for which the power of the third-order intermodulation distortion (IM3) products are equal to the output noise power [82]. This choice provides a worst-case noise figure, since the jitter noise contribution is maximized within the constraint of a distortion-free output signal. Expressions for P_{msf} are derived in [83]. Let us now examine some limiting cases of the noise figure given by

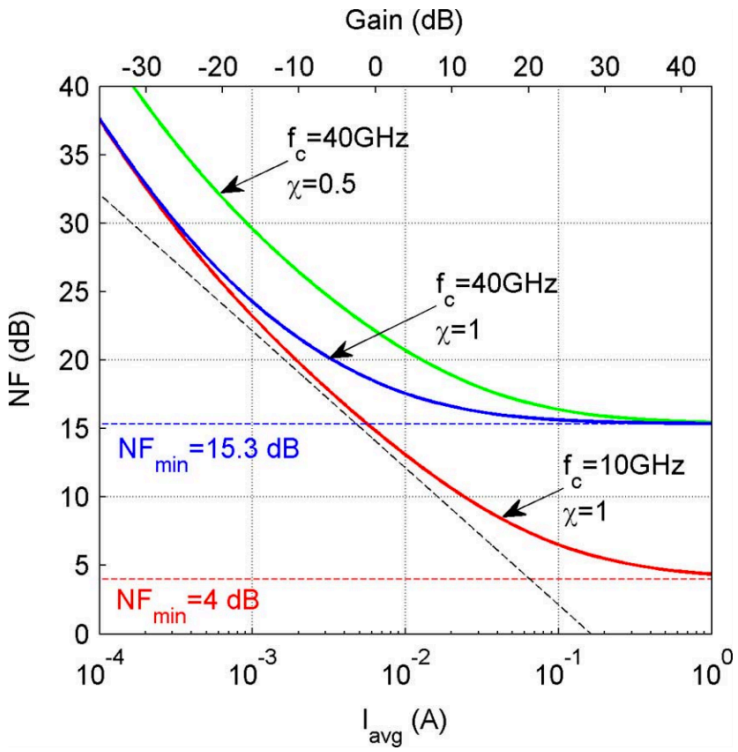

Fig. A.5 Subsampled link noise figure
Noise figure versus average photocurrent for a subsampled link with V_π=1 V, np=0, R_m=R_d=50 Ω, σ_T=10 fs, and B=1 GHz. The solid red and blue curves correspond to microwave carrier frequencies of 10 GHz and 40 GHz respectively and the parameter χ_M=1 was used. A carrier of 40 GHz was used for the green curve but with χ_M=0.5. The dotted black line shows the shot noise limited noise figure and the link gain is shown on the top x-axis for reference.

(A.12). As the gain tends toward infinity, the minimum noise figure is found to be

$$NF_{\min} = \lim_{G_c \to \infty} NF = 2 + \frac{4}{kTBR}\left(\frac{V_\pi}{\pi}\right)^2 \frac{\omega_{RF}^3 \sigma_T^3}{OSR} \tag{A.13}$$

where the jitter-limited P_{msf} has been used and the oversampling ratio (OSR) is defined as $OSR = f_s/(2B)$. Note that because of the jitter noise influence, the minimum noise figure is increased from the 3 dB limit of passively and losslessly impedance matched IM-DD link [75]. In the low-gain limit, the noise figure tends to $NF = 1/G_c$ which is equal to the loss of the link. Fig. A.5 shows the noise figure as a function of average photocurrent for three different cases. The link parameters used were V_π=1 V, np=0,

OSR=1, R_m=R_d=50 Ω, σ_T=10 fs, and B=1 GHz. The conversion gain is shown on the upper x-axis for reference, and the shot noise limited noise figure is shown by the dashed black line. The red and blue curves correspond to microwave carrier frequencies of 10 GHz and 40 GHz, respectively, and a value of χ_M=1 has been used. For the higher carrier frequency of f_c=40 GHz the effect of jitter noise becomes important at lower photocurrent levels and the minimum noise figure is increased by about 11 dB in the high gain limit. The green curve also shows the noise figure when f_c=40 GHz with χ_M=0.5 which reflects a sampling pulse-train with a relatively large duty cycle. Here, the noise figure is increased with respect to the χ_M=1 case but has the same high-gain limit since NF_{min} is not dependent on χ_M. From Fig. A.5 and the previous discussion, the impact of timing jitter on the noise properties of the subsampled link are seen to be significant, and limit the extent to which shot noise limited performance can be obtained. Furthermore, the degradation is increased for higher microwave carrier frequencies, which illustrates the importance of employing low-jitter optical pulse-trains in subsampled links.

A.4 Dynamic Range

As previously mentioned, the upper limit of the RF input power is determined by nonlinearities in the link components, which give rise to distortion and compression. For moderate laser powers, the linearity of the link is limited by the third-order intermodulation distortion produced by the modulator. These distortion products appear in the signal band and can not be filtered out [2]. The spurious-free dynamic range (SFDR) specifies the values of input RF power for which the fundamental output power is greater than the noise floor and for which the IM3 products remain below the

noise floor. The SFDR can be expressed as $SFDR = P_{msf}/P_{min}$, where P_{min} is defined as the input RF power when the fundamental component at the link output equals the output noise power [82]. Using (A.8) and assuming the output noise level at $P_{in} = P_{min}$ is shot noise dominated, the minimum input power can be expressed as

$$P_{\min} = \frac{2}{\chi_M^2}\left(\frac{V_\pi}{\pi}\right)^2 \frac{qB}{I_{avg}R_m} \tag{A.14}$$

As discussed in [83], the maximum spurious-free input power is determined from a cubic expression and yields unwieldy analytical expressions for P_{msf}. If P_{msf} is limited by either shot noise or jitter noise, however, approximate expressions for SFDR can be obtained to give

$$SFDR = \frac{2I_{avg}}{qB}\chi_M^2 \tag{A.15}$$

and

$$SFDR = \frac{2I_{avg}}{qB}\frac{\omega_{RF}\sigma_T}{\sqrt{OSR}}\chi_M^2 \tag{A.16}$$

for the cases of shot noise and jitter noise limited P_{msf}, respectively.

Simulated two-tone test results of a subsampled link are now presented, in order to show the validity the results derived above. For this simulation the RF signal

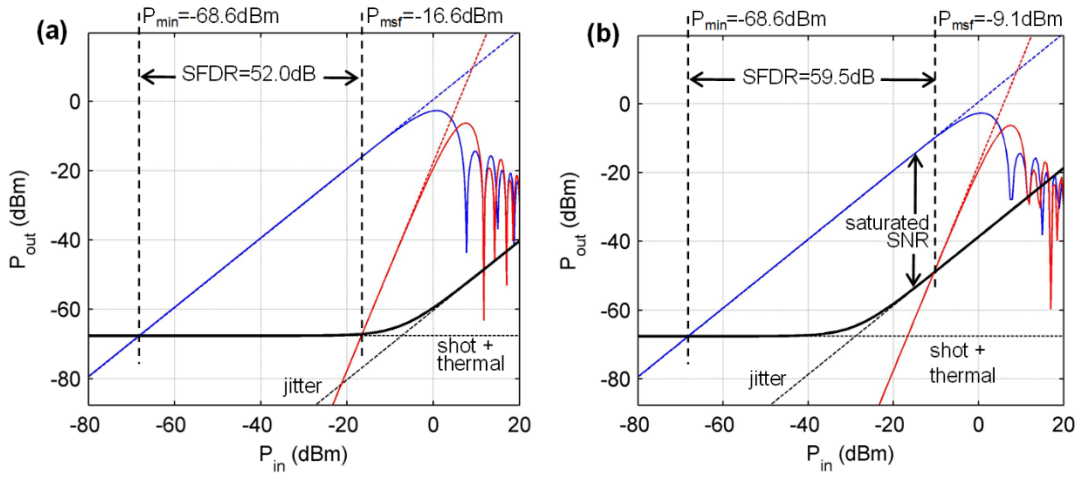

Fig. A.6 Subsampled link dynamic range
Simulated distortion diagrams for a subsampled analog optical link. The blue curve shows the fundamental power and the red curve shows the third-order intermodulation power. Parameters used were f_L=39.5 GHz, f_U=40.5 GHz, f_s=3.91 GHz, τ=5 ps, V_π=1 V, η=0.5 A/W, I_{avg}=10 mA. The timing jitter was assumed to be (a) σ_J=5 fs and (b) σ_J=80 fs. In (b) the SNR saturates to SNR_{sat}=36.8 dB due to the rising jitter noise floor and SFDR=59.5dB. In (a) the jitter contribution to the output noise is negligible and the maximum SNR is equal to SFDR=52.0 dB. Note that although the SFDR is larger for σ_J=80 fs, the maximum SNR is less than that for the σ_J=5 fs case as a result of the jitter-dominated output noise.

occupies the spectrum between f_L=39.5GHz, f_U=40.5GHz, and a sampling frequency of f_s=3.91 GHz (OSR=2) is chosen, determined by using (A.5) and (A.6) with N=21. The laser is assumed to produce Gaussian pulses with τ=5 ps and therefore χ_M=0.686 in this case. The modulator is assumed to be a MZM biased at quadrature with V_π=1 V and the detector is modeled with a responsivity of η=0.5 A/W. Additionally, any nonlinearity in the photodetector is neglected, since for low average photocurrents the modulator nonlinearity is dominant. For large photocurrents, however, this is no longer the case and the impact of photodiode nonlinearity becomes significant, as will be discussed at the end of this section. The signal at the link output was generated in the time-domain and then fast Fourier transformed to extract the amplitudes of the harmonic content in the frequency domain. Fig. A.6 shows distortion diagrams of the

link when the laser power is adjusted so that the average photocurrent in the detector is I_{avg}=10 mA. The blue curve in Fig. A.6 shows the fundamental output power and the red curve shows the third-order intermodulation distortion power. In Fig. A.6a the timing jitter of the laser is assumed to be σ_T=5 fs and in Fig. A.6b a value of σ_T=80 fs is used. The solid black line in Fig. A.6a-b is the total output noise, calculated using (A.9) with *B*=1GHz and *np*=0, and the contributions due to shot plus thermal noise and jitter noise are shown by the dotted black lines. In Fig. A.6a, P_{msf} is limited by shot and thermal noise and in Fig. A.6b P_{msf} is limited by jitter noise. Using (A.15) and (A.16) for these cases, respectively, provides SFDR=51.8 dB and SFDR=59.2 dB which are in good agreement with the simulated results. Note that for the larger jitter noise case of Fig. A.6b, the signal-to-noise ratio (SNR) saturates (SNR_{sat}=36.8 dB above P_{in}≈-30 dBm) as a result of the rising jitter noise floor. This is interesting to note since, although the SFDR is higher for σ_T=80 fs, the SNR is limited to

$$SNR_{sat} = \frac{OSR}{\omega_{RF}^2 \sigma_T^2} \tag{A.17}$$

which is simply the jitter-limited SNR of a sampled signal [81]. In Fig. A.6a, on the other hand, the SNR does not saturate since the output noise is dominated by thermal and shot noise contributions. In this case, the maximum SNR obtainable is simply equal to the SFDR.

Thus far, it has been assumed that the link SFDR is determined solely by modulator nonlinearities. This is valid for low to moderate levels of detector photocurrent. However, to achieve large signal-to-noise ratios and dynamic ranges, IM-DD analog links typically require large photocurrents on the order of tens of

milliamperes. Furthermore, in sampled optical links the peak intensity of pulses arriving at the photodiode is much larger than the DC value. As a result, sampled links may be more sensitive to photodiode nonlinearity than CW links [80, 84]. For large average photocurrents, photodiode saturation limits the small-signal response due to the accumulation of free carriers. These carriers build up in the device depletion layer, giving rise to an electric field that counteracts the depletion field, thereby decreasing carrier velocities and increasing transit times. For pulsed operation, the reduction in carrier transit time leads to a lengthening of the falling pulse edge, which becomes more pronounced for larger peak incident power levels.

To validate the assumption that modulator nonlinearities dominate for moderate photocurrents, the distortion performance of the idealized example link is compared to a commercially available, high-power photodiode. It can be shown that the output-referred third-order intercept point for the link analyzed in this paper is given by $OIP3 = 4(I_{avg}\chi_M)^2 R_d$ and for the parameters used in the previous simulation, this yields OIP3=9.7 dBm. For comparison, Discovery Semiconductors, Inc. offers high-power RF photodiodes with OIP3>45 dBm [85]. Since, the photodiode does not provide gain during the o/e conversion, and the total OIP3 of a cascade of components is determined by an inverse sum much like parallel resistors, the MZM nonlinearity will dominate in this situation [2]. As the average photocurrent is increased, however, the OIP3 of the subsampled link will be gradually reduced along with the SFDR, corresponding to the photodiode contribution.

It was mentioned that subsampling optical links have been used as front ends in photonic ADC architectures. In these applications it is useful to specify performance

metrics in effective number of bits (ENOB). This allows one to determine if an ADCs resolution is limited by the quantization process or by the subsampling photonic front end. Both the SNR and SFDR can be quoted in effective number of bits using [86]

$$SNRbits = \frac{SNR(dB) - 1.76}{6.02} \tag{A.18}$$

and

$$SFDRbits = \frac{SFDR(dB)}{6.02} \tag{A.19}$$

to allow for comparison with a given quantization core.

A.5 Conclusion

The operation and performance of subsampled analog optical links has been analyzed. The sampling criterion has been presented and the link conversion gain was derived as well as the noise figure. Also, in the limit of modulator dominated nonlinearity, the spurious-free dynamic range was derived. Pulse width considerations for the optical pulse train were discussed and then quantified through the χ_M parameter. It was shown how χ_M impacts the gain, noise figure, and SFDR, thereby revealing the impact of pulse width on link performance. Also, timing fluctuations in the pulsed laser were shown to limit the minimum obtainable noise figure as well as the maximum possible SNR of the link. Due to the low-jitter and short pulse widths available from mode-locked lasers, subsampled analog optical links are promising configurations for microwave systems that require downconversion with wide dynamic range. Therefore a sustained interest is expected by the research community, in developing subsampled

analog links for applications such antenna remoting and photonic analog-to-digital conversion.

References

[1] B. E. A. Saleh and M. C. Teich, *Fundamentals of Photonics*, 1991.

[2] D. M. Pozar, *Microwave Engineering*, 3 ed., 2005.

[3] C. Kachris and I. Tomkos, "A Survey on Optical Interconnects for Data Centers," *IEEE Communications Surveys & Tutorials,* vol. 14, pp. 1021-1036, 2012.

[4] J. A. Tatum, D. Gazula, L. A. Graham, J. K. Guenter, R. H. Johnson, J. King*, et al.*, "VCSEL-Based Interconnects for Current and Future Data Centers," *Journal of Lightwave Technology,* vol. 33, pp. 727-732, 2015.

[5] D. Mahgerefteh, C. Thompson, C. Cole, G. Denoyer, T. Nguyen, I. Lyubomirsky*, et al.*, "Techno-Economic Comparison of Silicon Photonics and Multimode VCSELs," *Journal of Lightwave Technology,* vol. 34, pp. 233-242, 2016.

[6] T. David, Z. Aaron, E. B. John, K. Tin, T. R. Graham, V. Laurent*, et al.*, "Roadmap on silicon photonics," *Journal of Optics,* vol. 18, p. 073003, 2016.

[7] T. Pinguet, P. M. D. Dobbelaere, D. Foltz, S. Gloeckner, S. Hovey, Y. Liang*, et al.*, "25 Gb/s silicon photonic transceivers," in *The 9th International Conference on Group IV Photonics (GFP)*, 2012, pp. 189-191.

[8] P. Westbergh, E. P. Haglund, E. Haglund, R. Safaisini, J. S. Gustavsso, and A. Larsson, "High-speed 850 nm VCSELs operating error free up to 57 Gbit/s," *Electronics Letters,* vol. 49, pp. 1021-1023, 2013.

[9] J. Mak, W. Sacher, J. Mikkelsen, T. Xue, Z. Yong, and J. Poon, "Automated Calibration of High-Order Microring Filters," in *CLEO: 2015*, San Jose, California, 2015, p. SW1N.2.

[10] J. R. Ong, R. Kumar, and S. Mookherjea, "Ultra-High-Contrast and Tunable-Bandwidth Filter Using Cascaded High-Order Silicon Microring Filters," *IEEE Photonics Technology Letters,* vol. 25, pp. 1543-1546, 2013.

[11] D. T. H. Tan, A. Grieco, and Y. Fainman, "Towards 100 channel dense wavelength division multiplexing with 100GHz spacing on silicon," *Optics Express,* vol. 22, pp. 10408-10415, 2014/05/05 2014.

[12] J. Xia, A. Bianco, E. Bonetto, and R. Gaudino, "On the design of microring resonator devices for switching applications in flexible-grid networks," in *2014 IEEE International Conference on Communications (ICC)*, 2014, pp. 3371-3376.

[13] H. Yan, L. Huang, X. Xu, S. Chakravarty, N. Tang, H. Tian*, et al.*, "Unique surface sensing property and enhanced sensitivity in microring resonator biosensors based on subwavelength grating waveguides," *Optics Express,* vol. 24, pp. 29724-29733, 2016/12/26 2016.

[14] LiangD, HuangX, KurczveilG, FiorentinoM, and R. G. Beausoleil, "Integrated finely tunable microring laser on silicon," *Nat Photon,* vol. 10, pp. 719-722, 11//print 2016.

[15] X. Li, Z. Li, X. Xiao, H. Xu, J. Yu, and Y. Yu, "40 Gb/s All-Silicon Photodetector Based on Microring Resonators," *IEEE Photonics Technology Letters,* vol. 27, pp. 729-732, 2015.

[16] Q. Xu, B. Schmidt, S. Pradhan, and M. Lipson, "Micrometre-scale silicon electro-optic modulator," *Nature,* vol. 435, pp. 325-327, 05/19/print 2005.

[17] T. Baba, S. Akiyama, M. Imai, N. Hirayama, H. Takahashi, Y. Noguchi*, et al.*, "50-Gb/s ring-resonator-based silicon modulator," *Optics Express,* vol. 21, pp. 11869-11876, 2013/05/20 2013.

[18] A. Roshan-Zamir, B. Wang, S. Telaprolu, K. Yu, C. Li, M. A. Seyedi*, et al.*, "A 40 Gb/s PAM4 silicon microring resonator modulator transmitter in 65nm CMOS," in *2016 IEEE Optical Interconnects Conference (OI)*, 2016, pp. 8-9.

[19] A. Yariv, "Universal relations for coupling of optical power between microresonators and dielectric waveguides," *Electronics Letters,* vol. 36, pp. 321-322, 2000.

[20] S. J. Mason, "Feedback Theory-Further Properties of Signal Flow Graphs," *Proceedings of the IRE,* vol. 44, pp. 920-926, 1956.

[21] L. A. Coldren, *Diode Lasers and Photonic Integrated Circuits*, 2 ed., 2012.

[22] B. E. Little, S. T. Chu, H. Haus, J. Foresi, and J. P. Laine, "Microring resonator channel dropping filters," *Lightwave Technology, Journal of,* vol. 15, pp. 998-1005, 1997.

[23] H. A. Haus, *Waves and fields in optoelectronics*. Englewood Cliffs, NJ: Prentice-Hall, 1984.

[24] W. Bogaerts, P. De Heyn, T. Van Vaerenbergh, K. De Vos, S. Kumar Selvaraja, T. Claes*, et al.*, "Silicon microring resonators," *Laser & Photonics Reviews,* vol. 6, pp. 47-73, 2012.

[25] G. I. Papadimitriou, C. Papazoglou, and A. S. Pomportsis, "Optical switching: switch fabrics, techniques, and architectures," *Journal of Lightwave Technology,* vol. 21, pp. 384-405, 2003.

[26] S. Aleksić, "Electrical power consumption of large electronic and optical switching fabrics," in *2010 IEEE Photonics Society Winter Topicals Meeting Series (WTM)*, 2010, pp. 95-96.

[27] A. W. Poon, L. Xianshu, X. Fang, and C. Hui, "Cascaded Microresonator-Based Matrix Switch for Silicon On-Chip Optical Interconnection," *Proceedings of the IEEE,* vol. 97, pp. 1216-1238, 2009.

[28] B. C. Pile, Y. Zhang, J. Yao, and G. W. Taylor, "Resonant optoelectronic thyristor switches as elements for optical switching fabrics," in *Proc. SPIE 8164, Nanophotonics and Macrophotonics for Space Environments V*, 2011, pp. 81640D-81640D-8.

[29] Y. Zhang, T. A. Vang, and G. W. Taylor, "Transistor based quantum well optical modulator and its performance in RF links," *Proc. SPIE 7817,* p. 781702, August 3 2010.

[30] Y. Zhang, B. Pile, and G. W. Taylor, "Design of micro resonator quantum well intensity modulator," *Optical and Quantum Electronics,* vol. 44, pp. 635-648, 2012/11/01 2012.

[31] S.-Y. Cho and R. Soref, "Interferometric microring-resonant 2 x 2 optical switches," *Opt. Express,* vol. 16, pp. 13304-13314, 2008.

[32] J. Zhensheng, Y. Jianjun, and C. Gee-Kung, "A full-duplex radio-over-fiber system based on optical carrier suppression and reuse," *IEEE Photonics Technology Letters,* vol. 18, pp. 1726-1728, 2006.

[33] "A 25 Gb/s Silicon Photonics Platform," 2012.

[34] S. Assefa, S. Shank, W. Green, M. Khater, E. Kiewra, C. Reinholm*, et al.*, "A 90nm CMOS integrated Nano-Photonics technology for 25Gbps WDM optical communications applications," in *Electron Devices Meeting (IEDM), 2012 IEEE International*, 2012, pp. 33.8.1-33.8.3.

[35] L. Guoliang, A. V. Krishnamoorthy, I. Shubin, Y. Jin, L. Ying, H. Thacker*, et al.*, "Ring Resonator Modulators in Silicon for Interchip Photonic Links," *Selected Topics in Quantum Electronics, IEEE Journal of,* vol. 19, pp. 95-113, 2013.

[36] Q. Xu, S. Manipatruni, B. Schmidt, J. Shakya, and M. Lipson, "12.5 Gbit/s carrier-injection-based silicon micro-ring silicon modulators," *Optics Express,* vol. 15, pp. 430-436, 2007/01/22 2007.

[37] X. Zheng, J. Lexau, Y. Luo, H. Thacker, T. Pinguet, A. Mekis*, et al.*, "Ultra-low-energy all-CMOS modulator integrated with driver," *Optics Express,* vol. 18, pp. 3059-3070, 2010/02/01 2010.

[38] W. D. Sacher and J. K. S. Poon, "Dynamics of microring resonator modulators," *Opt. Express,* vol. 16, pp. 15741-15753, 2008.

[39] W. D. Sacher, W. M. J. Green, S. Assefa, T. Barwicz, H. Pan, S. M. Shank*, et al.*, "Coupling modulation of microrings at rates beyond the linewidth limit," *Optics Express,* vol. 21, pp. 9722-9733, 2013/04/22 2013.

[40] H. Jianxun and Y. Enami, "Numerical Solution of the Dynamics of Microring Resonator Modulators," *Photonics Technology Letters, IEEE,* vol. 22, pp. 969-971, 2010.

[41] Z. Lin, L. Yunchu, J. Y. Yang, S. Muping, R. G. Beausoleil, and A. E. Willner, "Silicon-Based Microring Resonator Modulators for Intensity Modulation," *Selected Topics in Quantum Electronics, IEEE Journal of,* vol. 16, pp. 149-158, 2010.

[42] Y. Tong and C. Xinran, "On Power Consumption of Silicon-Microring-Based Optical Modulators," *Lightwave Technology, Journal of,* vol. 28, pp. 1615-1623, 2010.

[43] F. Koyama and K. Iga, "Frequency chirping in external modulators," *Lightwave Technology, Journal of,* vol. 6, pp. 87-93, 1988.

[44] G. L. Li and P. K. L. Yu, "Optical intensity modulators for digital and analog applications," *Lightwave Technology, Journal of,* vol. 21, pp. 2010-2030, 2003.

[45] Y. Li, L. S. Stewart, and P. D. Dapkus, "High speed silicon microring modulator employing dynamic intracavity energy balance," *Optics Express,* vol. 20, pp. 7404-7414, 2012/03/26 2012.

[46] S. Assefa, W. M. J. Green, A. Rylyakov, C. Schow, F. Horst, and Y. A. Vlasov, "CMOS Integrated Nanophotonics — enabling technology for exascale computing systems," in *2011 Optical Fiber Communication Conference and Exposition and the National Fiber Optic Engineers Conference*, 2011, pp. 1-3.

[47] S. Assefa, S. Shank, W. Green, M. Khater, E. Kiewra, C. Reinholm*, et al.*, "A 90nm CMOS integrated Nano-Photonics technology for 25Gbps WDM optical communications applications," in *2012 International Electron Devices Meeting*, 2012, pp. 33.8.1-33.8.3.

[48] J. C. Rosenberg, W. M. J. Green, J. Proesel, S. Assefa, D. M. Gill, T. Barwicz*, et al.*, "A monolithic microring transmitter in 90 nm SOI CMOS technology," in *Photonics Conference (IPC), 2013 IEEE*, 2013, pp. 223-224.

[49] M. R. Watts, D. C. Trotter, R. W. Young, and A. L. Lentine, "Ultralow power silicon microdisk modulators and switches," in *Group IV Photonics, 2008 5th IEEE International Conference on*, 2008, pp. 4-6.

[50] G. T. Reed, G. Mashanovich, F. Y. Gardes, and D. J. Thomson, "Silicon optical modulators," *Nat Photon,* vol. 4, pp. 518-526, 08//print 2010.

[51] V. M. N. Passaro and F. Dell'Olio, "Scaling and Optimization of MOS Optical Modulators in Nanometer SOI Waveguides," *Nanotechnology, IEEE Transactions on,* vol. 7, pp. 401-408, 2008.

[52] E. Dulkeith, F. Xia, L. Schares, W. M. J. Green, and Y. A. Vlasov, "Group index and group velocity dispersion in silicon-on-insulator photonic wires," *Optics Express,* vol. 14, pp. 3853-3863, 2006/05/01 2006.

[53] K. Padmaraju, J. Chan, L. Chen, M. Lipson, and K. Bergman, "Thermal stabilization of a microring modulator using feedback control," *Optics Express,* vol. 20, pp. 27999-28008, 2012/12/17 2012.
[54] M. A. Taubenblatt, "Optical Interconnects for High-Performance Computing," *Journal of Lightwave Technology,* vol. 30, pp. 448-457, 2012/02/12 2012.
[55] N. Dupuis, D. M. Kuchta, F. E. Doany, A. Rylyakov, J. Proesel, C. W. Baks*, et al.*, "Exploring the limits of high-speed receivers for multimode VCSEL-based optical links," in *Optical Fiber Communications Conference and Exhibition (OFC), 2014*, 2014, pp. 1-3.
[56] G. W. Taylor and H. Opper, "A thyristor-based photoreceiver based on the dual-channel double-heterostructure optoelectronic switch," *Quantum Electronics, IEEE Journal of,* vol. 40, pp. 1074-1086, 2004.
[57] H. Opper and G. W. Taylor, "Current–voltage relations for the dual channel double heterostructure optoelectronic switch," *Journal of Applied Physics,* vol. 94, pp. 1709-1720, 2003.
[58] G. W. Taylor, H. Opper, J. Cai, B. Garber, and R. Basilica, "Derivation of the switch-on parameters in the dual channel double heterostructure optoelectronic switch," *Journal of Applied Physics,* vol. 96, pp. 7612-7624, 2004.
[59] L. A. A. Pettersson, L. S. Roman, and O. Inganäs, "Modeling photocurrent action spectra of photovoltaic devices based on organic thin films," *Journal of Applied Physics,* vol. 86, pp. 487-496, 1999.
[60] R. Michalzik, "VCSELs: Fundamentals, Technology, and Applications," 2013.
[61] G. W. Taylor and J. G. Simmons, "The bipolar inversion channel field-effect transistor (BICFET);A new field-effect solid-state device: Theory and structures," *IEEE Transactions on Electron Devices,* vol. 32, pp. 2345-2367, 1985.
[62] M. S. Ünlü and S. Strite, "Resonant cavity enhanced photonic devices," *Journal of Applied Physics,* vol. 78, pp. 607-639, 1995.
[63] B. C. Pile and G. W. Taylor, "Resonant Cavity Enhanced Thyristor-Based Photodetectors for Optical Receivers," *IEEE Journal of Quantum Electronics,* vol. PP, pp. 1-1, 2016.
[64] T. Berceli and P. R. Herczfeld, "Microwave Photonics—A Historical Perspective," *IEEE Transactions on Microwave Theory and Techniques,* vol. 58, pp. 2992-3000, 2010.
[65] C. H. Cox, *Analog Optical Links - Theory and Practice*, 2006.
[66] R. Helkey, J. C. Twichell, and C. Cox, "A down-conversion optical link with RF gain," *Journal of Lightwave Technology,* vol. 15, pp. 956-961, 1997.
[67] A. Karim and J. Devenport, "High Dynamic Range Microwave Photonic Links for RF Signal Transport and RF-IF Conversion," *Journal of Lightwave Technology,* vol. 26, pp. 2718-2724, 2008.
[68] C. K. Sun, R. J. Orazi, and S. A. Pappert, "Efficient microwave frequency conversion using photonic link signal mixing," *IEEE Photonics Technology Letters,* vol. 8, pp. 154-156, 1996.
[69] R. P. Braun, G. Grosskopf, D. Rohde, and F. Schmidt, "Optical millimetre-wave generation and transmission experiments for mobile 60 GHz band communications," *Electronics Letters,* vol. 32, pp. 626-628, 1996.
[70] C. K. Sun, R. J. Orazi, S. A. Pappert, and W. K. Burns, "A photonic-link millimeter-wave mixer using cascaded optical modulators and harmonic carrier generation," *IEEE Photonics Technology Letters,* vol. 8, pp. 1166-1168, 1996.

[71] P. W. Juodawlkis, J. J. Hargreaves, R. D. Younger, G. W. Titi, and J. C. Twichell, "Optical Down-Sampling of Wide-Band Microwave Signals," *Journal of Lightwave Technology,* vol. 21, p. 3116, 2003/12/01 2003.
[72] J. Kim, M. J. Park, M. H. Perrott, and F. X. Kärtner, "Photonic subsampling analog-to-digital conversion of microwave signals at 40-GHz with higher than 7-ENOB resolution," *Optics Express,* vol. 16, pp. 16509-16515, 2008/10/13 2008.
[73] W. Chang, *RF Photonic Technology in Optical Fiber Links*, 2002.
[74] D. Chen, H. R. Fetterman, A. Chen, W. H. Steier, L. R. Dalton, W. Wang*, et al.*, "Demonstration of 110 GHz electro-optic polymer modulators," *Applied Physics Letters,* vol. 70, pp. 3335-3337, 1997.
[75] P. W. Juodawlkis, J. C. Twichell, G. E. Betts, J. J. Hargreaves, R. D. Younger, J. L. Wasserman*, et al.*, "Optically sampled analog-to-digital converters," *IEEE Transactions on Microwave Theory and Techniques,* vol. 49, pp. 1840-1853, 2001.
[76] J. D. McKinney and V. J. Urick, "Radio-Frequency Down-Conversion via Sampled Analog Optical Links," N. R. Laboratory, Ed., ed. Washington DC, 2010.
[77] R. G. Vaughan, N. L. Scott, and D. R. White, "The theory of bandpass sampling," *IEEE Transactions on Signal Processing,* vol. 39, pp. 1973-1984, 1991.
[78] V. J. Urick, M. S. Rogge, F. Bucholtz, and K. J. Williams, "The performance of analog photonic links employing highly compressed erbium-doped fiber amplifiers," *IEEE Transactions on Microwave Theory and Techniques,* vol. 54, pp. 3141-3145, 2006.
[79] G. H. Smith, D. Novak, and Z. Ahmed. (1997, Technique for optical SSB generation to overcome dispersion penalties in fibre-radio systems. *Electronics Letters 33(1),* 74-75. Available: http://digital-library.theiet.org/content/journals/10.1049/el_19970066
[80] J. D. McKinney and K. J. Williams, "Sampled Analog Optical Links," *IEEE Transactions on Microwave Theory and Techniques,* vol. 57, pp. 2093-2099, 2009.
[81] P. Smith, "Little Known Characteristics of Phase Noise," Analog Devices, Norwood, MA, Application Note AN-741, 2004.
[82] B. H. Kolner and D. W. Dolfi, "Intermodulation distortion and compression in an integrated electrooptic modulator," *Applied Optics,* vol. 26, pp. 3676-3680, 1987/09/01 1987.
[83] B. Pile and G. W. Taylor, "Performance of Subsampled Analog Optical Links," *Journal of Lightwave Technology,* vol. 30, pp. 1299-1305, 2012/05/01 2012.
[84] P.-L. Liu, M. Y. Frankel, K. J. Williams, R. D. E. D. S. D. Esman, and A. Weiner, "Saturation characteristics of fast photodetectors," in *Conference on Lasers and Electro-Optics*, San Francisco, California, 1998, p. CThM2.
[85] D. S. Inc. *InGaAs Photodiodes: 6 GHz, Highly Linear, Optical Power Handling*. Available: http://www.discoverysemi.com/Product_Pages/DSC100_100S.php
[86] R. H. Walden, "Analog-to-digital converter survey and analysis," *IEEE Journal on Selected Areas in Communications,* vol. 17, pp. 539-550, 1999.